Development of Photo-functional Systems based on Supramolecular Chemistry

超分子化学に基づいた光機能性システムの開発

Submitted to

the Graduate School of Science and Technology

in Partial Fulfillment of the Requirements

for the Degree of Philosophy in Technology

Tokyo University of Science

Masaaki Akamatsu

Table of Contents

Chapter 1
Introduction

1-1 Development of organic device system

Recently, electronic equipments, such as personal computers and cell phones have become key tools for our life. Also, because our society is based on information processed by electronic equipments, they can be crucial techniques for humans. To achieve more convenient society, developments of an electronic equipment bearing higher functionalities has proceeded. For these functions, equipments are consisted from some functional devices, e. g. central processing unit (CPU), hard disk, transistor, battery cell. Thus, functionalities of electronic equipments depend on performances of these devices. Research to develop a functional device system bearing a high performance has been enthusiastic in the area of material science.

Conventionally, these device systems have been constructed from inorganic substances. For instance, most currently available non-disk memory devices are based on silicon or silicon nitride semiconductor technology with information being stored through application of an electrical bias. That's because some crucial properties for operating device systems were previously limited in inorganic substances (e. g. semi-conductors and conductors). However, in 1974, H. Shirakawa found a conductive polymer (polyacetylene).[1] It was firstly revealed that organic substances also show the electronic conductivity. From this work, developments of electronic devices using organic compounds, so called 'organic electronics' have emerged.[2] There are some advantages to use organic substances for device systems, as below.[3] At first, because organic compounds have a diversity of molecular structures, verifications of the structure are facile for improvements of these properties. Secondly, they have processability. For example, flexible displays and devices are developed. In addition, compared to inorganic devices, organic ones are relatively lighter. From these excellences, organic device systems have been applied to organic light emitting devices, dye-sensitized solar cells, organic transistors, and sensors, and conventional inorganic-based materials have been replaced by organic ones. Thus, the organic device system is said as a future functional device system.

1-2 Supramolecular chemistry and their functionalities

In 1970s, supramolecular chemistry, a new category of chemistry was born. Supramolecular chemistry treats with associates and assemblies of molecules, formed by weak interactions, such as non-covalent bonds (coordination, electrostatic force, hydrogen bond, van der Waals force, donor-acceptor interaction, etc.) (Figure 1).[4]

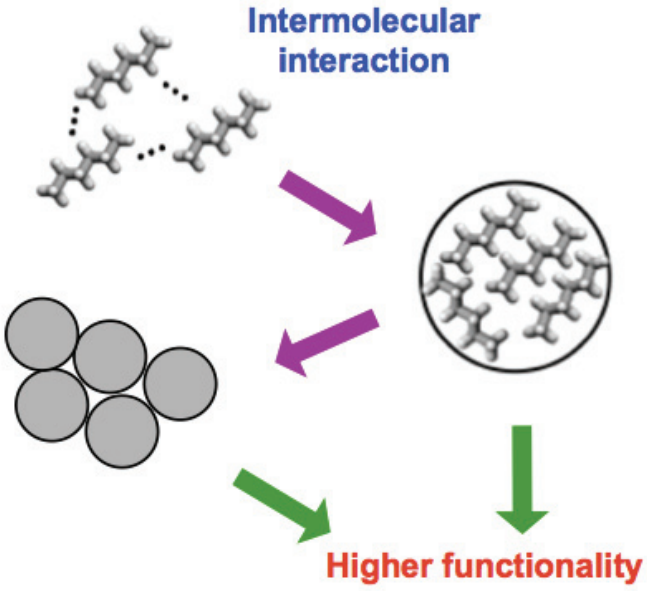

Figure 1. Association and assembly of molecules by non-covalent interactions.

As a result, supramolecules show higher functions beyond a single molecule. Afterward, this area had rapidly been developed, and then the Novel Prize in Chemistry was awarded to C. J. Pederson, D. J. Cram and J. M Lehn, who had highly contributed this area. Supramolecular chemistry is categorized to 1) small molecular system, 2) multi molecular system, 3) polymer system, 4) crystalline system, and 5) supramolecular aggregate (Figure 2).

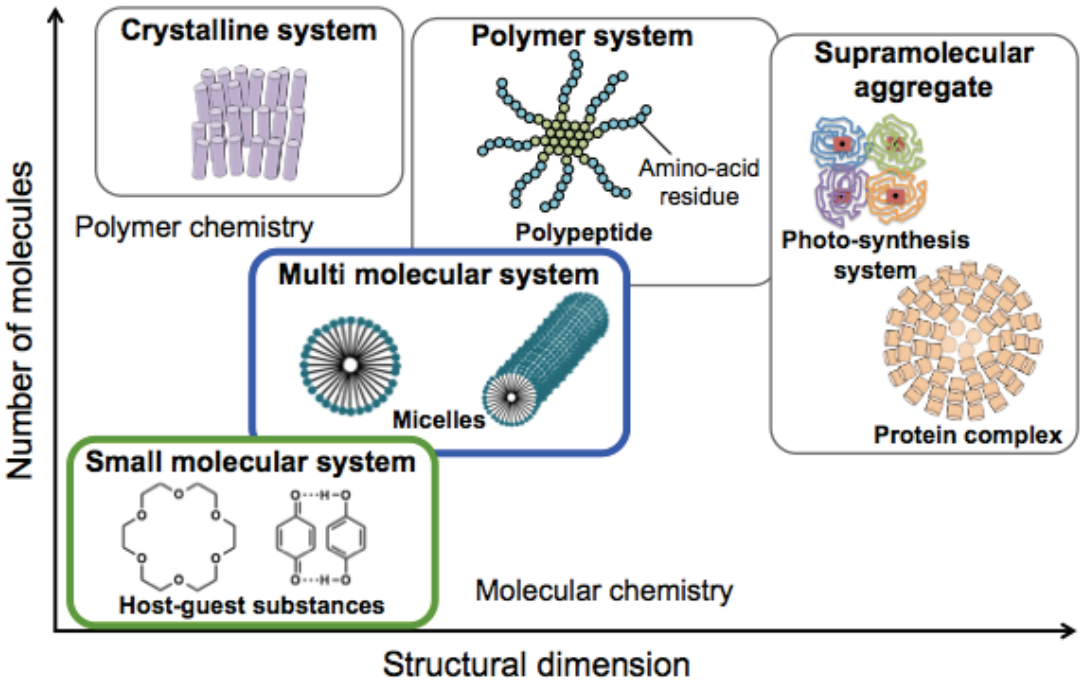

Figure 2. Categories of supramolecular chemistry.

Among them, "Small molecular system" is a representative. In 1999, C. J. Pederson reported the synthesis of cyclic ethers and the inclusion behavior of cations (such as metal ions) to inside of the molecule (Figure 3).[5] This inclusion behavior is derived from electrostatic interaction between lone pair electrons of oxygen atoms and cation, and a selective inclusion of cation is possible by changing the radius of the circle of the structure. Afterwards, this kind of molecules is named *crown ethers*, and has becomes a representative in supramolecular chemistry. Moreover, since some oligosaccharides, *cyclodextrins* have a hydrophobic space at the inside of the molecule, this molecule can catch an organic molecule inside.[6] In addition, a cyclic phenol derivative, called calixarene, can also trap molecules inside.[7] Such an inclusion behavior of the small molecular system enables selective incorporations due to the sizes and affinities between host and guest molecules. Thus, this system has been applied to chemical sensors or artificial enzymes.

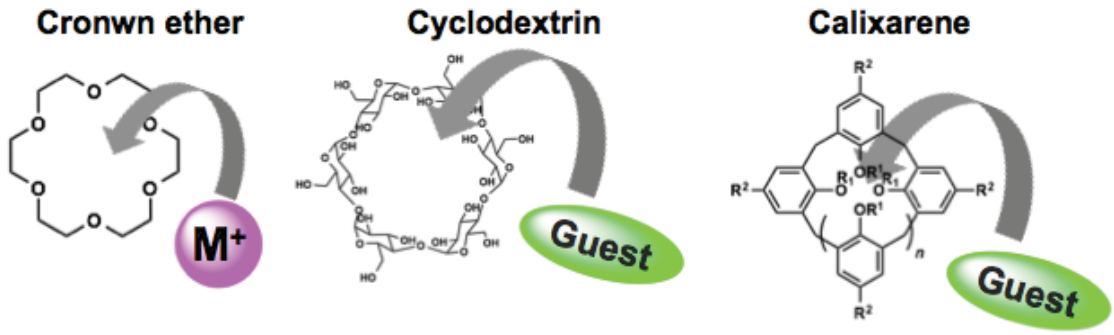

Figure 3. Clathrate behavior by cyclic compounds.

Moreover, although the inclusion behavior works with an association of a couple of molecules and ions, there is also "multi molecular system", assembling much amount of molecules. For this category, a representative example, molecular assemblies, formed by surfactant molecules, is described here. A surfactant molecule, which is a kind of amphiphile molecule bearing hydrophilic and hydrophobic moieties forms molecular assembles, called "micelle" at above the critical micelle concentration (CMC) (Figure 4). Depending on the conditions, such as molecular structure, concentration, and temperature, micelles show varieties of structures. These micelles have characteristic functions. For instance, because organic molecules are incorporated inside of the micells (hydrophobic space), water-insoluble molecules can be solubilized in the aqueous solution. Moreover, in special systems, to which rod-like micelles grows the viscosity of the solution changes with entanglements of the micelles like polymer chains.

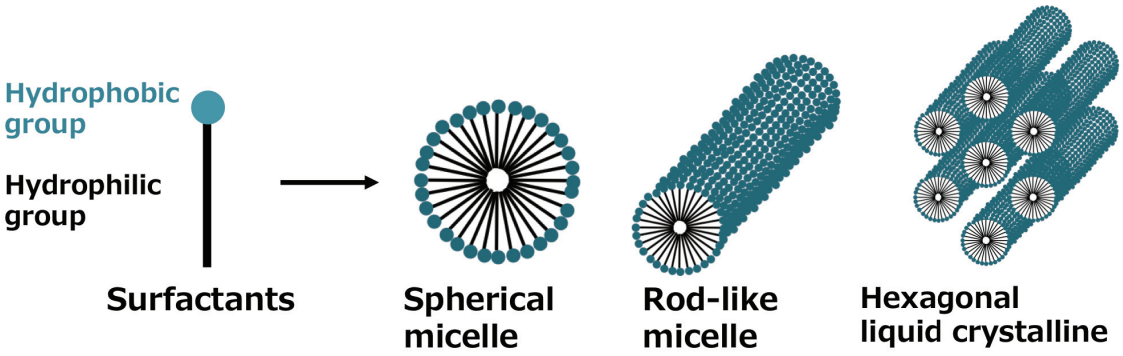

Figure 4. Self-assemblies of surfactant molecules.

As mentioned up to here, functions accomplished by interactions among two or more molecules are characteristic in supramolecular chemistry.

1-3 Stimuli-responsive molecules

Stimuli-responsive molecules, which show *output* with an application of *input* by using several kinds of stimuli, are known (Figure 5). Simply, the function of these molecules is a molecular system for information or function transformations. As stimuli, chemical information (e. g. addition of molecule and change in pH[8]) or physical information (e. g. application of light,[9] electronic[10] or magnetic field,[11] temperature[12]) are used in this system. For instance, photochromic molecules are well known, whose colors as output vary with application of light as input. Furthermore, a polarity of a ferrocene molecule dramatically changes with redox reactions caused by an application of electronic field. The affinity of polymer bearing *N*-isopropylacrylamide (NIPAM) units to water decreases with increase of temperature. Moreover, there have been various kinds of pH-responsive dyes. These varieties of functions of responsive-molecules would be applied to future organic device systems. In fact, a phthalocyanine molecule is currently used for a compact disk (CD-R).

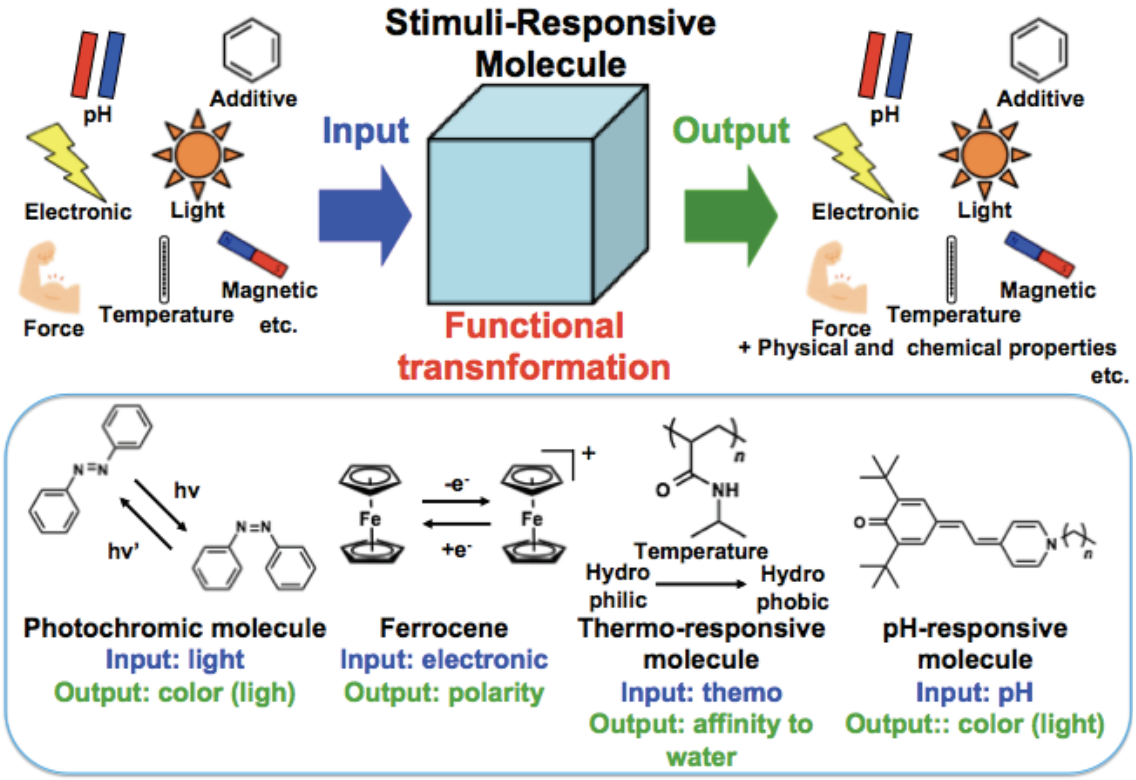

Figure 5. Stimuli-responsive molecules.

1-4 Stimuli-responsive supramolecular systems

Here, if this stimuli-responsive molecule is combined with supramolecular system, a responsive supramolecular system, which has a higher performance and a new functionality than a single molecular system, can be developed. F. M. Raymo *et al*. reported a molecular memory using a change in an UV/vis absorption spectrum, resulted by proton transfer with photo-isomerization of a spiropyran analog (Figure 6a).[13] They also demonstrated the characteristic behavior of sequential logic operators using this system. In addition, Y. Li *et al*. reported temperature-tunable formation and deformation of vesicles, formed by the diblock copolymers containing poly NIPAM and poly(N-(3-aminopropyl)methacrylamide hydrochloride) (Figure 6b).[14] In this system, control release of substances in the inner water layer of the vesicles can be developed.

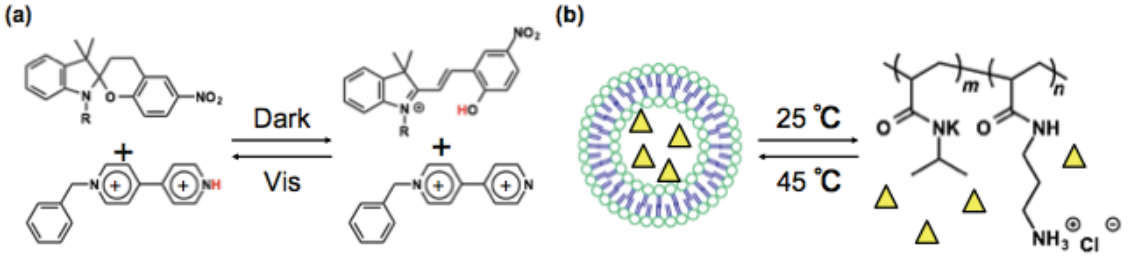

Figure 6. Stimuli-responsive supramolecular systems (a: molecular memory using a photochromic molecule, b: controlled formation of vesicles).

Among these stimuli-responsive supramolecular systems, light is highly paid attention as input and output from following reasons. First of all, because light can be irradiated to small area, a function transformation is possible within minute scales. This enables developments of small sized organic device systems. Secondly, since light irradiation adds no chemicals to the system, it is relatively clean. In addition, because light as output can be recognized by naked eyes, it is a facile way to detect. Finally, optical properties can be characterized by general equipments (e. g. UV/vis and fluorescence spectroscopies). From these advantages, developments of new photo-functional supramolecular device systems have proceed. For example, H. Shi *et al.* reported district heating/cooling systems by using a photo-responsive worm-like micellar solution.[15] Furthermore, G. Grynkiewicz, *et al.* developed a fluorescence probe, which selectively recognizes calcium ion. By using this probe, calcium ion in the body

was successfully visualized.[16] Also, our group has reported some photo-responsive supramolecular systems, based on multi moleculer system supramolecules (micelles).[17–20] Morphological changes in the micellear structures with light irradiation enable control-release of substances and viscosity changes of aqueous solutions. For example, I have previously reported the reversible controlled release and uptake of oily substances with cationic surfactant micelles containing an azobenzene unit as a photo-responsive moiety.[21] Ultraviolet light irradiation to an aqueous solution of a *trans*-isomer of an azobenzene-type cationic surfactant (AZTMA) with solubilized ethylbenzene resulted in photo-isomerization to the *cis* isomer, which caused the release of a portion of the solubilized ethylbenzene. Subsequent visible light irradiation of the *cis*-AZTMA solution resulted in photo-isomerization to the *trans* isomer that resolubilized released ethylbenzene.

1-5 Development of novel functionalities using dynamic chemical equilibrium of supramolecules

Chemical reactions, such as acid-base reaction, host-guest complexations, formations of molecular assemble are based on dynamic chemical equilibrium (Figure 7). In these reactions, the transformations between reactants and products move at an equal rates, and a balance of reactants and products is expressed by an equilibrium constant, *K*. The constant is determined by chemical and physical conditions. Thus it can be tuned by changes in the conditions, produced by application of chemical and physical stimuli.

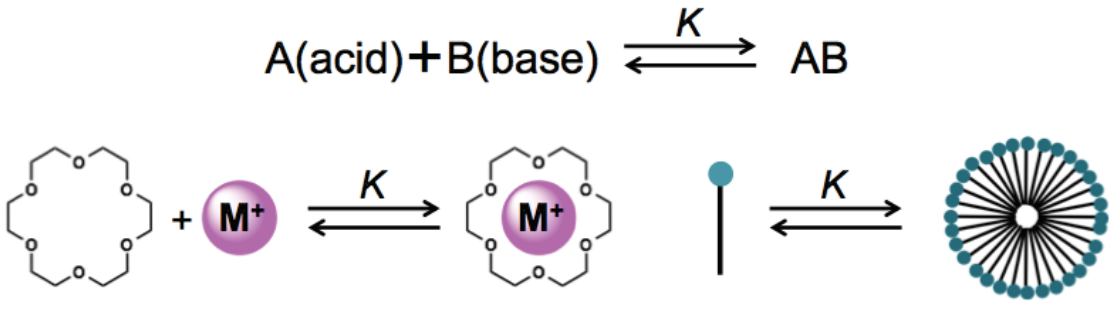

Figure 7. A series of chemical reactions, formed by dynamic chemical equilibrium (acid-base reaction, host-guest complexiations, and molecular assembby).

Here, the tunable chemical reaction by stimuli can be applicable for making

multiple chemical states (see Figure 8). These chemical states can produce variations in chemical signal (output) for sensor or probes. Thus, by utilizing the view of chemical equilibrium of supramolecules, molecular systems bearing novel functionalities can be developed.

Figure 8. Multiple chemical states produced by dynamic chemical equilibrium.

1-6 Dissertation outline

As described above, photo-functional molecular systems based on supramolecular chemistry would enable developments of novel functional device systems. In this thesis, I have investigated the applicatios of photo-functional systems based on supramolecular chemistry, e. g. sensors, molecular memories, probes, and also photo-responsive surfactant systems.

In Chapter 2, developments of an optical sensor and molecular memories, based on acid-base reaction of phenolic fluorophores are described. In section 2-1, an alcohol sensor was developed with a fluorescence response of a terphenol/base composite to solvents. Introduction of a hydrophilic group to the structure of terphenol increased affinity of the composite with inorganic base to ethanol, and as a result 15v/v% of ethanol contents in an alcohol beverage could be detected by the fluorescence response. Combination of the composite and water-absorbent polymer successfully detected up to 5v/v% of ethanol contents in an alcohol beverage due to condensation of ethanol in the solution on the material. Also, sensing of gas-state ethanol was demonstrated by using a composite of terphenol-inorganic base mixture and nanofibrous polymer film bearing high surface area. In 2-2, volatile and non-volatile molecular memories were developed by using changes in the fluorescence color caused by acid-base reaction of phenolic hydroxyl group with fluoride anion and water molecules. The varieties of fluoresce color of the phenols are derived from changes in the dynamic chemical equilibrium of three emissive species (phenol and phenolide states, hydrogen-bonded species between phenol and fluoride anion). By using base and water for information storing, both

non-volatile and volatile memory systems were successfully developed.

In Chapter 3, developments of supramolecular probe systems for detections of cesium are described. A fluorescence cesium probe was newly synthesized. This probe enabled a detection of cesium in the solid state in a micro-meter scale. Also, accumulation spots of cesium in the cell of *Arabidopsis* were revealed. On the other hand, a detection of cesium ion in an aqueous system was tried by using an ion-responsive membrane system (optode). A newly prepared optode membrane showed a selective detection of cesium ion with color variations.

Chapter 4 treats with analysis of developments of photo-functional systems with molecular assembles formed by surfactants. In section 4-1, small-angle neuron scattering (SANS) analysis was carried out for micelles formed by a photo-responsive surfactant (AZTMA). The results reveal prolate micells are formed by AZTMA in aqueous solutions, and the population and the short radius of the micelles reversibly changed. Moreover, AZTMA micelles solubilizing excess amounts of ethylbenzene additionally incorporate the solubilizates with ultraviolet light irradiation. Effects of photo-irradiation on structures of the micelles and the solution property were examined. Section 4-2 describes acceleration of a photo isomerization reaction of lophine dimer was investigated by using the inside of micelles as reaction sites. The photo isomerization reaction of a lophine dimer, solubilized in 10 mM cetyltrimethylammonium bromide (CTAB) aqueous solution, was enhanced *ca.* 10-fold, compared to one in organic solvents (octane and toluene).

Chapter 5 presents summary of this thesis.

References

(1) Ito, T.; Shirakawa, H.; Ikeda, S. *J. Polym. Sci. Polym. Chem. Polym. Chem.* **1974**, *12*, 11–20.

(2) Facchetti, A. *Chem. Mater.* **2011**, *23*, 733–758.

(3) Kim, T. W.; Yang, Y.; Li, F.; Kwan, W. L. *NPG Asia Mater.* **2012**, *4*, e18.

(4) Lehn, J. *Angew. Chem. Int. Ed. Engl.* **1988**, *27*, 89–112.

(5) Cao, C.; Jiang, Y. L.; Stivers, J. T.; Song, F. *Nat. Struct. Mol. Biol.* **2004**, *11*, 1230–1236.

(6) Chithra, P.; Varghese, R.; Divya, K. P.; Ajayaghosh, A. *Chem. Asian J.* **2008**, *3*, 1365–1373.

(7) Debler, E. W.; Kaufmann, G. F.; Meijler, M. M.; Heine, A.; Mee, J. M.; Pljevaljcic, G.; Di Bilio, A. J.; Schultz, P. G.; Millar, D. P.; Janda, K. D.; Wilson, I. a; Gray, H. B.; Lerner, R. a. *Science* **2008**, *319*, 1232–1235.

(8) Hisamoto, H.; Manabe, Y.; Yanai, H.; Tohma, H.; Yamada, T.; Suzuki, K. *Anal. Chem.* **1998**, *70*, 1255–1261.

(9) Wei-Guang D., E. *J. Phys. Chem. A* **2004**, *108*, 950–956.

(10) Kaifer, A. E. *Acc. Chem. Res.* **1999**, *32*, 62–71.

(11) Brown, P.; Bushmelev, A.; Butts, C. P.; Cheng, J.; Eastoe, J.; Grillo, I.; Heenan, R. K.; Schmidt, A. M. *Angew. Chem. Int. Ed.* **2012**, *51*, 2414–2416.

(12) Fujishige, S.; Kubota, K.; Ando, I. *J. Phys. Chem.* **1989**, 3311–3313.

(13) Raymo, M. F.; Alvarado, R. J.; Giordani, S.; Cejas, M. A. *J. Am. Chem. Soc.* **2003**, *125*, 2361–2364.

(14) Li, Y.; Lokitz, B. S.; McCormick, C. L. *Angew. Chem. Int. Ed. Engl.* **2006**, *45*, 5792–5795.

(15) Shi, H.; Ge, W.; Oh, H.; Pattison, S. M.; Huggins, J. T.; Talmon, Y.; Hart, D. J.; Raghavan, S. R.; Zakin, J. L. *Langmuir* **2013**, *29*, 102–109.

(16) Grzegorz, G.; M, P.; Tsien, R. Y. *J. Biol. Chem.* **1985**, *260*, 3440–3450.

(17) Matsumura, A.; Tsuchiya, K.; Torigoe, K.; Sakai, K.; Sakai, H.; Abe, M. *Langmuir* **2011**, *27*, 1610–1617.

(18) Orihara, Y.; Kodashima, H.; Matsumura, A.; Ohkubo, T.; Tsuchiya, K.; Abe, M. *J. Am. Chem. Soc.* **2005**, *127*, 13454–13455.

(19) Sakai, H.; Taki, S.; Tsuchiya, K.; Matsumura, A.; Sakai, K.; Abe, M. *Chem. Lett.* **2012**, *41*, 247–248.

(20) Aikawa, S.; Shrestha, R.; Ohmori, T.; Yuko, F.; Yoji, T.; Endo, T.; Kanjiro, T.; Koji, T.; Kazutami, S.; Kenichi, S.; Masahiko, A.; Hideki, S. *Langmuir* **2013**, *29*, 5668–5676.

(21) Orihara, Y.; Matsumura, A.; Saito, Y.; Ogawa, N.; Saji, T.; Yamaguchi, A.; Sakai, H.; Abe, M. *Langmuir* **2001**, *17*, 6072–6076.

Chapter 2
Novel Optical Supramolecular Devices based on Acid-base Reaction of Phenol Derivatives

2-1 Reversible Fluorometric Alcohol Sensing with Phenol Derivative

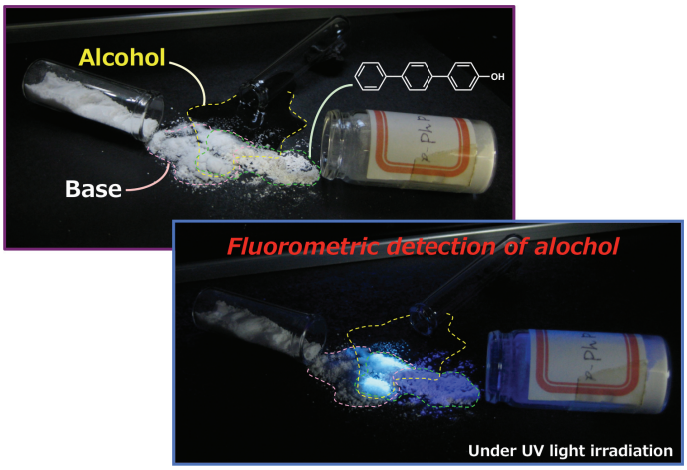

Abstract

In this section, an alcohol sensor was developed using the solid-state fluorescence emission of terphenyl-ol (TPhOH) derivatives. Admixtures of TPhOH and sodium carbonate exhibited blight sky-blue fluorescence in the solid state upon addition of small quantities of ethanol. A series of TPhOH derivatives were synthesized, and the effects of solvent polarities and the structures of these π-conjugated systems on the fluorescence were systematically investigated by fluorescence spectroscopy. In particular, π-extended TPhOHs and TPhOHs containing electron withdrawing group showed significant solvatochromism, whose fluorescence colors varied from blue to red. Detection of ethanol contents in alcohol beverages was demonstrated using different TPhOHs revealing the effect of molecular structure on sensing properties. Ethanol contents in highly concentrated alcohols were estimated from the intensity of the fluorescence elicited from the TPhOHs. Moreover, when terphenol and Na_2CO_3 were blended into a water-absorbent polymer ethanol could be detected at lower concentrations. Detection of ethanol vapor was also accomplished using a nanofibrous polymer scaffold as the immobilized sensing film. Estimation of alcohol contents in solution and vapor phases using simple fluorescence visualization is expected to be applicable in the food and beverage industries.

2-1-1 Introduction

Electronic tongues[1–3] and noses[4,5] that operate analogously with the senses of taste and smell[6] have attracted the attention of researchers not only as a means of imitating those human senses but also for potential applications in analyses of foods and beverages.[7–9] Alternatively, molecule-based sensors have been developed because they present several advantages, including in the miniaturization of sensor systems and because of their excellent selectivities and tunable properties. Indeed, operation of the senses of taste and smell in higher organisms is based on the molecule-level detection of substances. Some examples of optical molecular sensors that imitate the senses of taste and smell have already been reported.[10–19]

Certain phenol derivatives are known to exhibit increases in fluorescence intensity in the solid state when treated with solutions of basic substances.[20] In this work we have used the solid-state fluorescence response of phenol derivatives to develop an optical sensor for the ethanol contents of various alcoholic beverages. Alcohol sensing has previously been achieved by colorimetric detection involving reduction of chromates or using semiconductor devices[22]. However, these systems have some disadvantages such as non-reversible detection or the requirement for the use of a special and costly device. A few molecule-based alcohol sensors have been reported.[22–24] For example, Kessler *et al.* developed a colorimetric alcohol sensor using a solvatochromic dye.[23]

Our group found that ground powdered combinations of 1wt% of TPhOH derivatives and a carbonate salt exhibit bright fluorescence (e. g. sky blue) in the presence of ethanol under UV light irradiation. Based on this observation, I have developed a fluorometric solvent sensing system by using the phenol-phenoxide equilibrium. In particular, by introducing a substitute to the TPhOH structure, the affinity to ethanol may be increased, resulting enhancement of the responsivity for ethanol. A series of phenol derivatives were synthesized and the effects of solvents on their solid-state fluorescence emission were examined in the presence of alkali metal carbonates. The fluorescence responses of derivatives of TPhOH could be used to estimate ethanol contents in alcoholic beverages. Alcohol sensing for low concentrations of alcohol (for instance, contained in a ‘low alcohol’ beer) was also attempted by combining a water-absorbent polymer with TPhOH. Finally, the detection of vapor phase ethanol was conducted using a nanofiber film containing TPhOH and a base. This alcohol sensing system is based on fluorescence visualization, is highly

reversible and exhibits wide ranging sensitivity.

2-1-2 Results and discussion

TPhOH **3** exhibited weak purple-blue fluorescence in the solid state and in the presence of ethanol (added by dropping on the solid; Figure 1a). On the other hand, a ground mixture of **3** and an inorganic base (Na_2CO_3) underwent a change in the wavelength of fluorescence with a concomitant increase in the apparent emission intensity from weak purple-blue fluorescence (380 nm) to bright sky-blue fluorescence (472 nm) upon addition of ethanol (Figure 1b and 1c). Furthermore, the fluorescence gradually recovered to its initial weak purple-blue fluorescence with evaporation of the ethanol over a 15 minute period (Figure 1b) in normal humidity level (relative humidity 30–60 %). This reversible fluorescence switching on addition of ethanol can be repetitively cycled (Figure 1d).

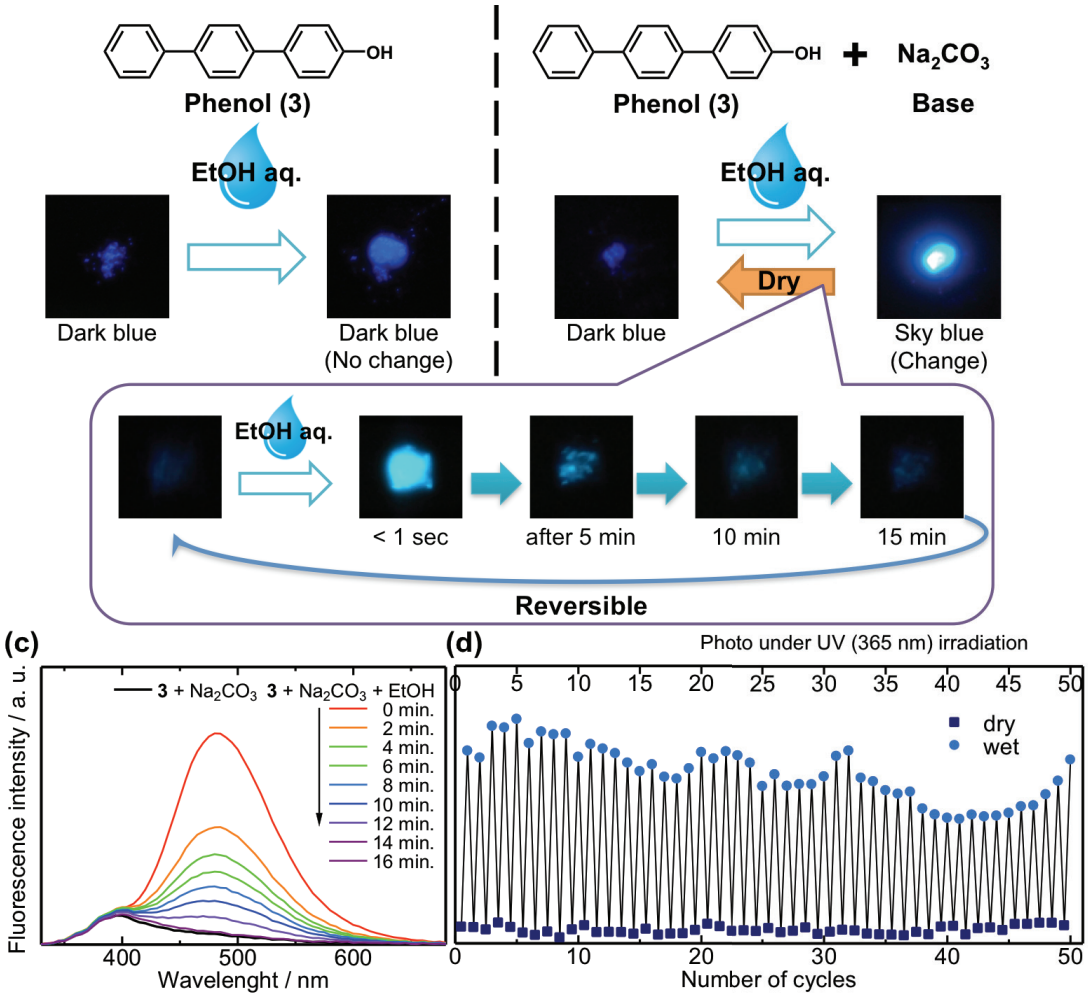

Figure 1. Schematic presentation of color change in solid-state fluorescence with phenol derivatives. Luminescence changing of powder of **3** (a), the mixture **3**+Na_2CO_3 (b, c) under UV irradiation (365 nm) before and after drop ethanol. Fluorescence spectra of the mixture **3**+Na_2CO_3 after drop ethanol. Time range from 0 to 16 min. (c) reversible changes of fluorescence intensities of the mixture **3**+ Na_2CO_3 alternate dry and wet with ethanol (d).

In order to tune fluorescence properties of the TPhOHs, the other prepared phenols were also mixed with inorganic base, and the fluorescence response was examined. Composite powders of the phenol derivatives (**2**–**5**, **3F**) and base (K_2CO_3) were prepared by grinding, and variation in the fluorescence of these powders was examined after addition of different organic solvents (water, chloroform, THF, acetone, acetonitrile, ethanol, methanol, DMF and DMSO) (Figure 2) revealing that fluorescence color of **3** varies from blue to green depending on solvent. The other phenols also showed solvatochromism in their fluorescence (**4**: blue–white, **5**: blue–pink, **3F**: blue–yellow). Interestingly, **3F** showed white-colored emission only in the presence of acetonitrile suggesting its use as a selective sensor for that solvent. The chromaticity coordinates calculated from the fluorescence spectrum of **3F** are at (0.32, 0.38), which is located nearly in the white region according to the 1934 CIE coordinate diagram. Comparison of **4** and **5** with **3** showed more significant solvatochromism because of the extended π-conjugated systems on **4** and **5**. Calculation of the molecular orbital structures suggests that the phenoxide form of TPhOH derivatives (e. g. **3F**) undergoes intramolecular electron transfer in its excited state (Figure 3). This suggests that trifluoromethyl units in the structure of **3F** decrease the electron density on the end phenyl group and enhance intramolecular electron transfer. Thus, **3F** exhibits fluorescence at longer wavelengths than **3**. Maximum fluorescence wavelengths were plotted against $E_T(30)$ values,[25] which denote the polarity characteristics of each organic solvent (Figure 4). In the points for solvents of lower polarity, these plots show reasonable linearity. The discontinuity for solvents of higher polarity is likely due to the effects of hydrogen bonding between the phenol and solvent molecules. In addition, significant red shifts were observed in fluorescence and UV/vis absorption bands of phenols (50–160 nm) upon addition of basic (tetra-*n*-butylammonium fluoride: TBAF) even in THF solutions (Figure 2c, 2d and 2e).

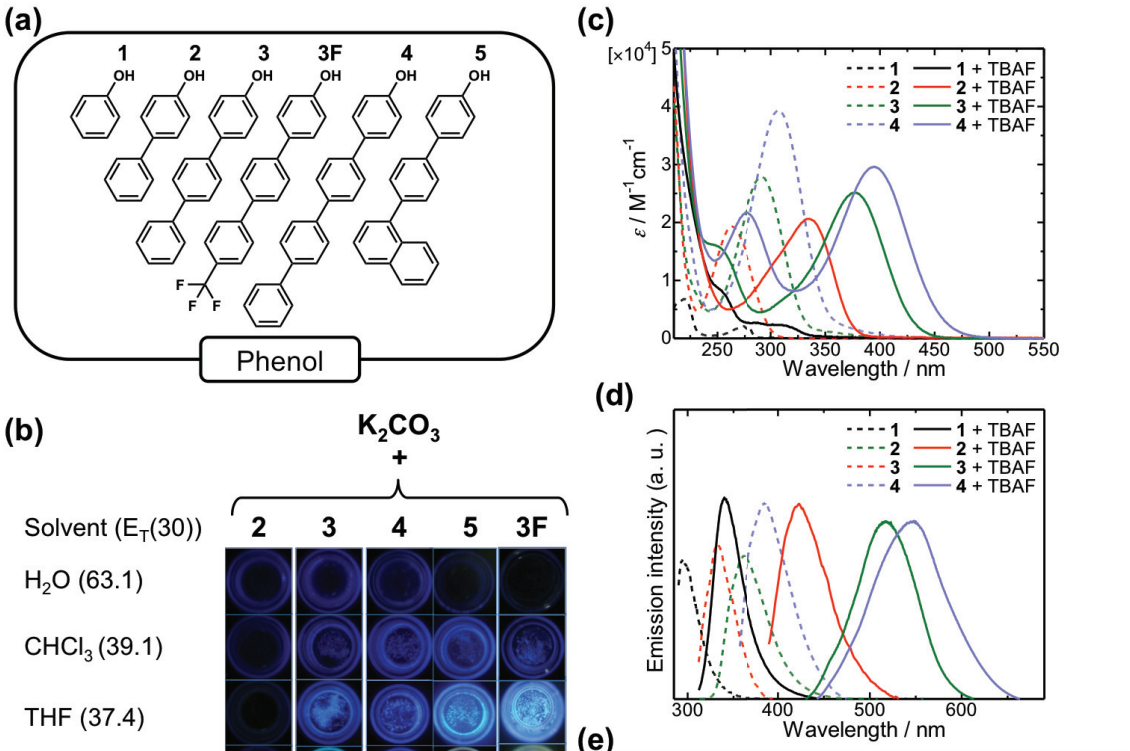

(e)

Phenol	Base	λ_{abs} / nm ($\varepsilon M^{-1}cm^{-1}$)	λ_{en} / nm
1	—	273 (0.21)	294
1	TBAF	310 (0.23)	340
2	—	262 (1.93)	333
2	TBAF	335 (2.06)	422
3	—	291 (2.78)	362
3	TBAF	375 (2.51)	518
4	—	306 (3.93)	385
4	TBAF	394 (2.96)	547

Phenol: 1×10^{-4} M, TBAF: 1×10^{-2} M in THF

Figure 2. Color alignments in solid-state fluorescence of phenol derivatives with base by adding various organic solvents. (a) Chemical structures of the phenol **1**, **2**, **3**, **4**, **5**, **3**F. (b) Photographs of the mixture of phenol (**2**, **3**, **4**, **5**, **3**F) and K_2CO_3 under UV irradiation (365 nm) after drop various solvents. UV/vis (c) and fluorescence (d) spectra of phenol **1** to **4** in THF (1.0×10^{-4} M) before and after dropping TBAF in THF (1.0×10^{-2} M) were summarized in Table (e).

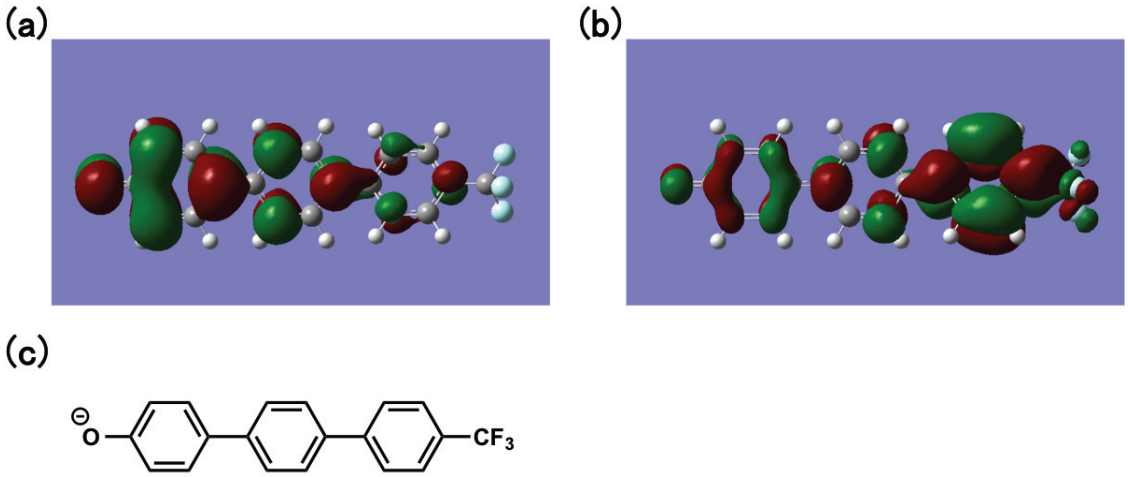

Figure 3. DFT (B3LYP6-31G) calculations of HOMO (a) and LUMO (b), and chemical structure of **3F3** (a phenoxide state).

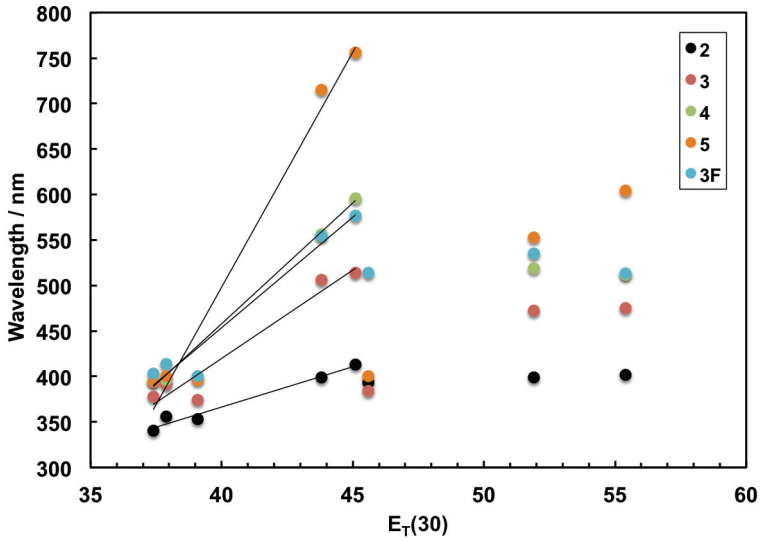

Figure 4. Plots of fluorescence wavelengths of vs. $E_T(30)$ values of organic solvents with approximate curves for plots in the region of lower polarities.

Solid-state fluorescence responses of the phenols in admixture with carbonate were applied for ethanol sensing. After adding a series of aqueous ethanol solutions to **3** or **3TEG** in the solid state in admixture with Na_2CO_3, absolute quantum yields were measured (Figure 5a and 5b). Here, the value of absolute quantum yield is treated as a quantitative fluorescence intensity of the solid-state sample. With increasing ethanol

content, fluorescence intensity increased and gave sigmoidal-shaped curves when plotted against the water/ethanol ratio. This indicates that the fluorescence response is closely related to deprotonation of the phenol. **3TEG** showed stronger fluorescence than **3**, and the detection limit was ca. 15v/v% of ethanol (**3**: 30v/v%). To examine this behavior, solubilities of **3** or **3TEG** (in admixture with sodium carbonate) in a series of ethanol aqueous solutions were also measured. Variations in solubility gave similarly sigmoidal shaped curves as those obtained for quantum yields (Figure 5c). Thus, it seems likely that the fluorescence response is due to dissolution of the phenol and base in the aqueous ethanol solution probably with concomitant reaction to the deprotonated more highly fluorescent phenoxide in solution. Thus, the solubility of the phenols in the presence of base is a key factor in the fluorescence response in ethanol/water. Consequently, because the more hydrophilic phenol **3TEG** is more soluble in solvent mixtures of low alcohol concentration, it showed improved sensitivity over TPhOH **3**. I also attempted ethanol sensing in alcoholic beverages (Figure 6a). As expected, a brighter fluorescence response was observed for those with increasing ethanol contents. An ethanol sensor array involving a series of phenols (**3** and **3F**) and bases (triethylamine, Na_2CO_3 and K_2CO_3) enabled estimation of the ethanol contents of the alcoholic beverages simply by observing differences in fluorescence intensity. In addition, the same sensor array could be repetitively applied for ethanol content sensing simply by drying between analyses (Figure 6b).

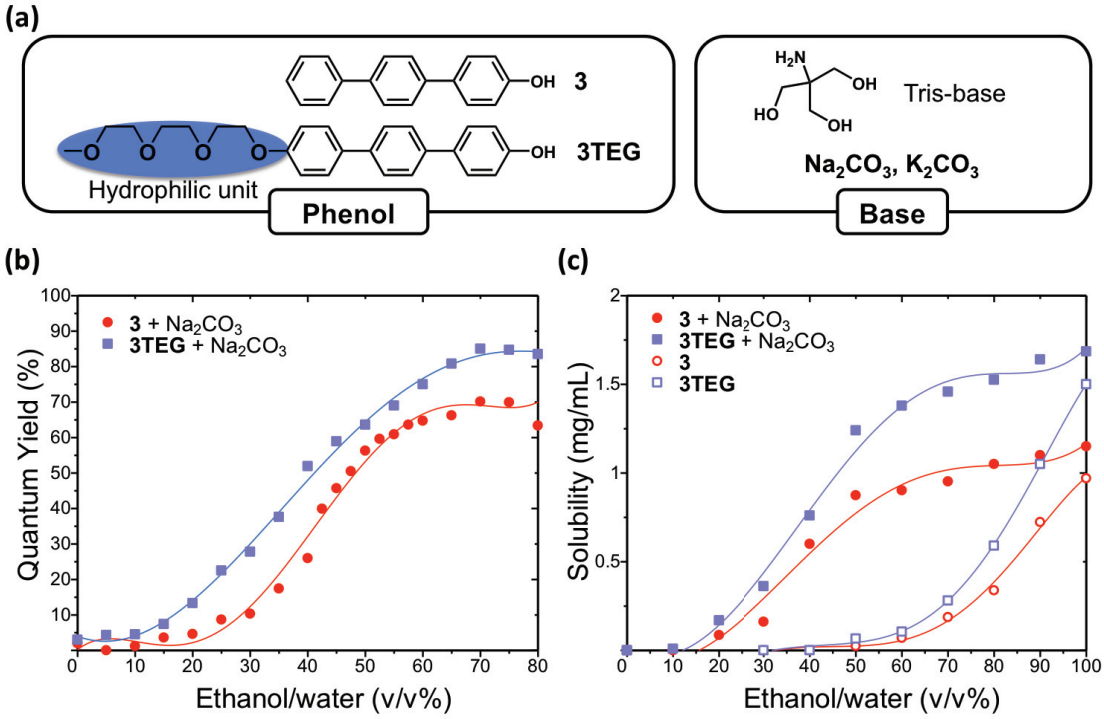

Figure 5. Alcohol concentration response of the mixture between the phenol derivatives and the base. (a) Chemical structures of the phenol derivatives and the base. (b)The variation in quantum yield of both mixture **3**+ Na_2CO_3 and **3TEG**+Na_2CO_3 in ethanol/water with concentration. (c)Solubility of phenol **3** and **3TEG**, mixture **3**+Na_2CO_3 and **3TEG**+Na_2CO_3 plotted as ethanol/water concentration.

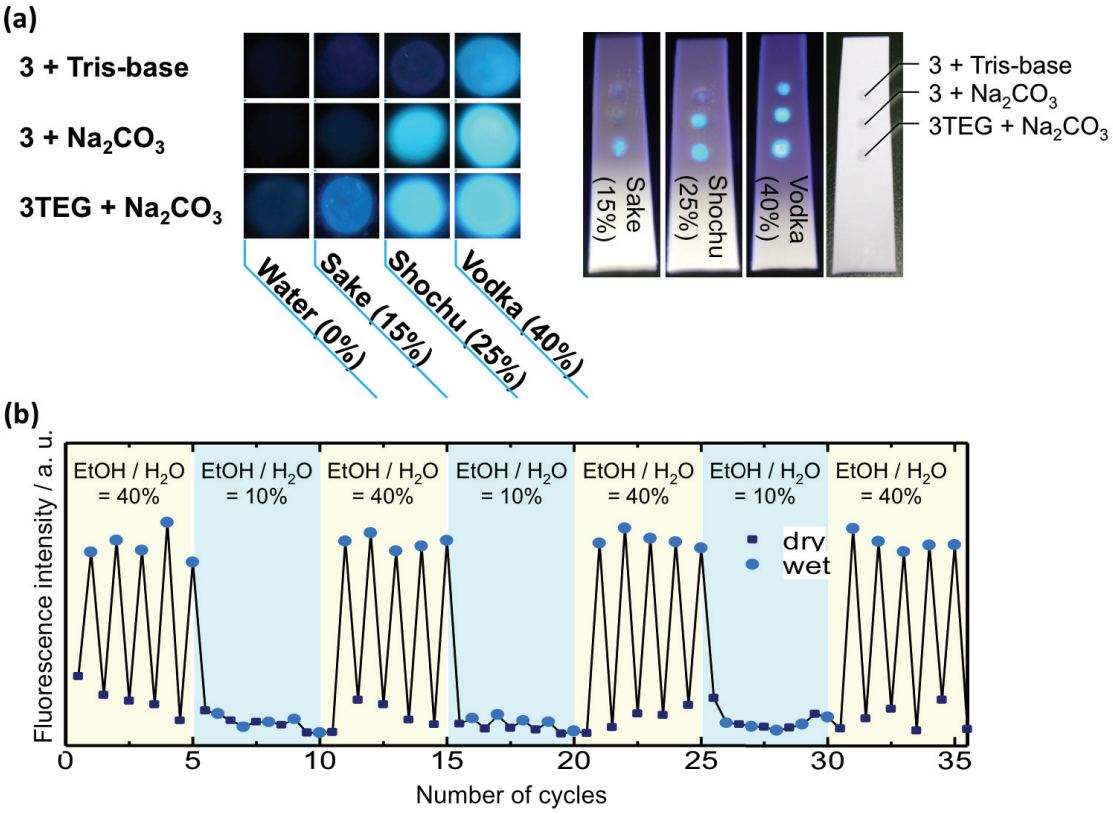

Figure 6. Photographs of the mixture **3**+Tris and **3**+Na_2CO_3, **3TEG**+Na_2CO_3 under UV irradiation (365 nm) after drop various concentration alcoholic beverages (a). Reversible changes of fluorescence intensities of the mixture **3**+Na_2CO_3 alternate 40% and 10% ethanol/water (v/v) (b).

I found that including a water-absorbent polymer led to an enhanced sensitivity for this system (Figure 7a) presumably due to an increase in the local ethanol:water ratio. Solid **3** and Na_2CO_3 were mixed and combined with sodium polyacrylate as the water-absorbent polymer. In this case, the sensor material could be used to detect down to 5v/v% of ethanol in water by observing the fluorescence response (Figure 7b). The polymer layer absorbs water from the alcohol mixture thereby increasing the ethanol content and facilitating its detection. By this means, sensing of ethanol in beer (5v/v%) could be demonstrated although ethanol content of non-alcoholic beer (0.00%) could not be estimated (Figure 7c). Thus, the sensitivity of solid-state detection using fluorescence was improved to 5v/v% ethanol content by incorporating the probe molecules (and base) into a water-absorbent polymer, and the ethanol contents of commercially available alcoholic beverages could be estimated.

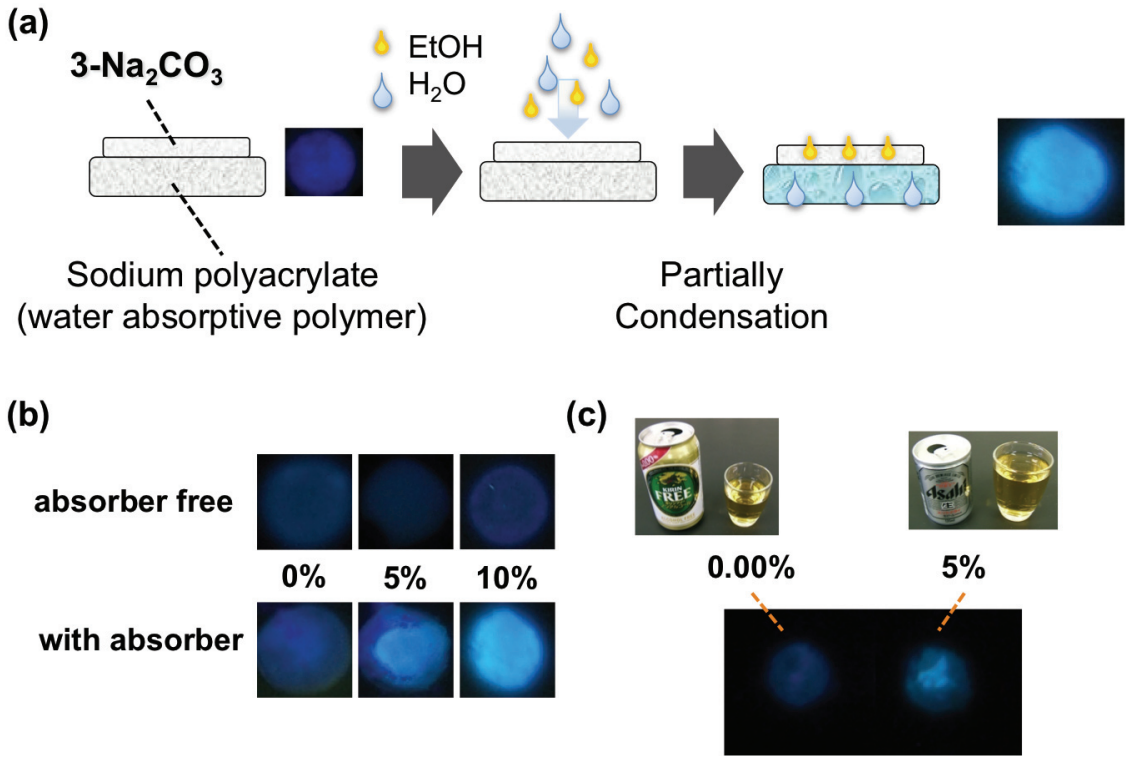

Figure 7. Improving alcohol concentration responsivity of the mixture between the phenol derivatives and the base by assisting water absorptive polymer. (a) Schematic illustration of mixture **3**+Na_2CO_3 on sodium polyacrylate as water absorptive polymer to recognize lower alcohol concentration. Photograph of mixture **3**+Na_2CO_3 on sodium polyacrylate after drop wine (10% Alc.) under UV irradiation (365 nm). (b) Fluorescence change of the mixture **3**+Na_2CO_3 on sodium polyacrylate after drop various concentration alcoholic beverages under UV irradiation (365 nm). (c) Photographs of **3** + Na_2CO_3 on sodium polyacrylate under UV irradiation (365 nm) after dropping non-alcoholic beer (left; KIRIN Free from Kirin Brewery Company, Limited) and normal beer (right; Super dry from ASAHI BREWERIES, LTD.).

Sensing of ethanol in the vapor phase was also attempted by incorporating the phenol/base system with other materials. **3** and Na_2CO_3 were mixed with basic alumina (Al_2O_3) and the characteristic bright sky-blue fluorescence could easily be observed under a flow of ethanol-saturated air, although a solid mixture of **3** and Na_2CO_3 without Al_2O_3 showed no observable fluorescence under similar treatment (Figure 8b). Fluorescence due to the ethanol vapor was eliminated by flowing ethanol-free air; a sensing process that could be repeated many times (Figure 8c). Supposedly, the response to ethanol vapor is enhanced in this case since basic alumina increases the prevalence of the phenoxide form over that simply in the presence of sodium carbonate. I have also attempted to further improve sensitivity towards vapor phase ethanol by increasing the available surface area for sensing. For this purpose, I prepared a PVA nanofiber film as a composite containing **3** and K_2CO_3 by using the electrospinning technique. The material obtained was a self-standing film with an internal structure of high surface area composed of entangled nanoscale fibers observed by scanning electron microscopy (SEM) (Figure 9a). A clear fluorescence response was observed in the nanofiber film when placed in a flow of ethanol-saturated air. Fluorescence emission measurements revealed that this film gave a 10-fold enhancement of fluorescence emission intensity over a cast film (Figure 9b) leading to greater sensitivity to ethanol vapor.

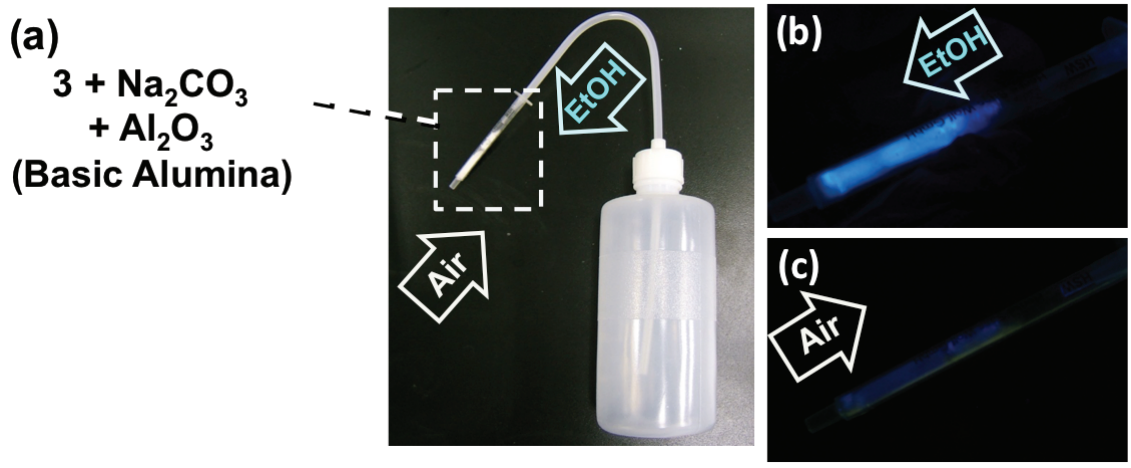

Figure 8. Alcohol gas sensing of phenol and base composite nanofibers. (a) Photograph of alchol gas sensor prepared by the mixture of **3**+Na_2CO_3 and basic alumina in plastic tube. (b and c) fluorescence change of alchol gas sensor under UV irradiation (365 nm) through ethanol gas (b) and air (c).

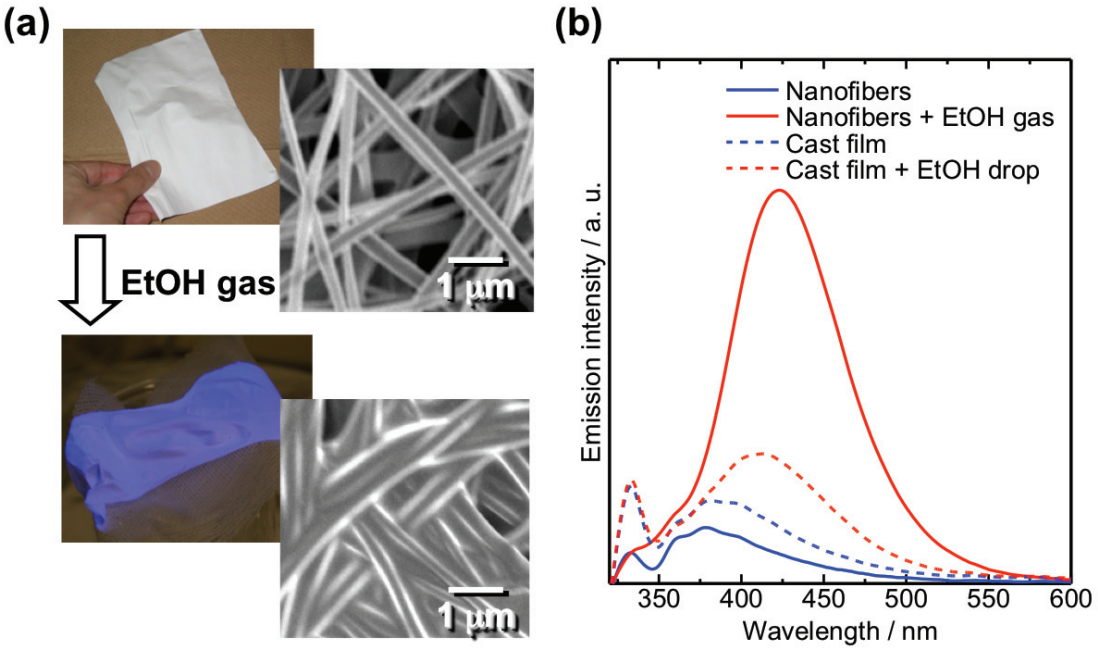

Figure 9. Composite nanofibers flim prepared by aqueous solution of **3** and K_2CO_3, PVA Photographes of composite nanofibers film under light (top left) and after exposure to alcohol gas under UV irradiation (365 nm) (bottom left). SEM images of composite nanofibers film before (top right) and after exposure to ethanol gas (bottome left) (a). Fluorescence spectra of composite nanofibers film and cast films prepared by queous solution of **3** and K_2CO_3, PVA, before and after exposure to ethanol gas (b).

2-1-3 Conclusions

In summary, I have developed an alcohol sensor involving solid-state fluorescence emission of phenol derivatives. Combinations of compounds **3** or **3TEG** with carbonate in the solid state can be used to estimate ethanol contents in alcoholic beverages due to a bright fluorescence emission in the presence of concentrated ethanol (more than 15v/v%) solutions. Sensitivity could be improved by incorporation of the sensing material into a water-absorbent polymer leading to estimation of ethanol contents in solution down to 5v/v% by simple observation of fluorescence. In addition, combining the ethanol sensor in a nanofiber polymer film possessing a large surface area enabled detection of ethanol in the vapor phase. The fluorescence visualization of ethanol content in solution and vapor phases demonstrated here is expected to be applicable in the food and beverage industries. Also, as mentioned above, it is a simple matter to combine the sensing activity reported here with that of other colorimetric or fluorometric systems especially in order to differentiate ethanol from other related analytes such as methanol. I am currently working to combine ethanol sensing and differentiation in a single device.

2-1-4 Experimental part

General procedures.

Solvents and reagents, including phenol derivatives **1** and **2** were purchased from Tokyo Chemical Industry Co. Ltd. (Tokyo, Japan) or Wako Pure Chemical Co. (Osaka, Japan) and were used without further purification. All reactions and fractions eluted during chromatographic separations were monitored using thin layer chromatography on glass-backed plates (Kieselgel 60 F254). The developed thin layer chromatography plates were observed under UV light at 254 and 365 nm. Flash column chromatography over silica gel (LC60A35-70 μM) was used for all separations.

Measurements.

^{1}H and ^{13}C NMR spectra were measured at 298 K from an acetone-d_6 solution of the samples using a JEOL model AL300BX (300 MHz) spectrometer with $SiMe_4$ as internal standard. Chemical shifts (*d*) and coupling constants (*J*) are given in parts per million and Hertz, respectively. ESI-MS spectra were measured using a JASCO model JMS-T100CS. HRMS (ESI-negative) spectra were measured using a JEOL model JMS-MS700. UV/vis absorption spectra were measured using a Shimadzu model UV-3600 UV-VIS-NIR Spectrometer. Fluorescence spectra of solutions were measured using a JASCO model FP-6500 Fluorescence Spectrometer. Fluorescence spectra of solid-state samples were measured from solid samples using an Otsuka Electronics, model MCPD-7000 spectrometer. Absolute quantum yield measurements were carried out with C9920-02 (Hamamatsu Photonics), SEM images were obtained using a Hitachi SU-8000 scanning electron microscope operating at an accelerating voltage of 5 kV.

Synthesis and structural characterization.

3,[20] **3TEG**,[8] **4**[20] and **5**[3] were prepared as has been previously reported. **3F** was prepared by a literature method involving a phosphine-free Suzuki coupling reaction.[26]

4''-(trifluoromethyl)-[1,1':4',1''-terphenyl]-4-ol (3F)

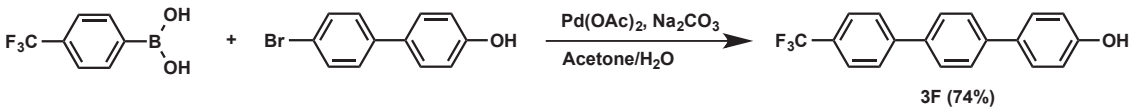

3F (74%)

A mixture of Na_2CO_3 (0.212 g, 2.0 mmol), $Pd(OAc)_2$ (0.001 g, 0.5 mol %),

4-Bromo-4'-hydroxybiphenyl (0.249 g, 1.0 mmol), 4-(Trifluoromethyl)phenylboronic Acid (0.227 g, 1.2 mmol), distilled water (10 mL) and acetone (8.5 mL) was stirred for 3 hours at room temperature. The resulting mixture was neutralized with a dilute HCl aq., and the precipitate was filtrated and washed with water. The residue was subjected to column chromatography (SiO_2, AcOEt) yielding **3F** as white powder (0.234 g) in 74% yield. ^{1}H-NMR (300 MHz, acetone-d_6, δ, ppm): 6.97 (d, 2H, J = 9.0; Ar-H), 7.60 (d, 2H, J = 9.0; Ar-H), 7.69–7.87 (m, 6H; Ar-H), 7.94 (d, 2H, J = 9.0; Ar-H), 8.55 (s, 1H; phenol-OH). ^{13}C-NMR (75 MHz, acetone-d_6, δ, ppm): 116.68, 126.53, 126.59, 126.64, 126.69, 127.72, 128.15, 128.40, 128.84, 132.22, 138.08, 141.82, 158.35. HRMS (ESI) m/z calcd for $C_{19}H_{12}F_3O$ $[M-H]^-$: 313.084, found 313.082.

Preparation of alcohol-responsive composite powders and characterization of their solid-state fluorescence responses.

1wt% of terphenyl-ol derivatives (**1**–**5**, **3F** and **3TEG**) was mixed in carbonate salt (Na_2CO_3 or K_2CO_3) as a matrix. The composite powder (ca. 5 mg) was placed onto a substrate, and then ethanol aqueous solution, organic solvent or alcohol beverage (10 μL) was added to it. Resulting fluorescence responses were observed, and was measured using fluoresce spectrometer as shown in Figure 10. The solid-state fluorescence was induced to the detector through a glass fiber line.

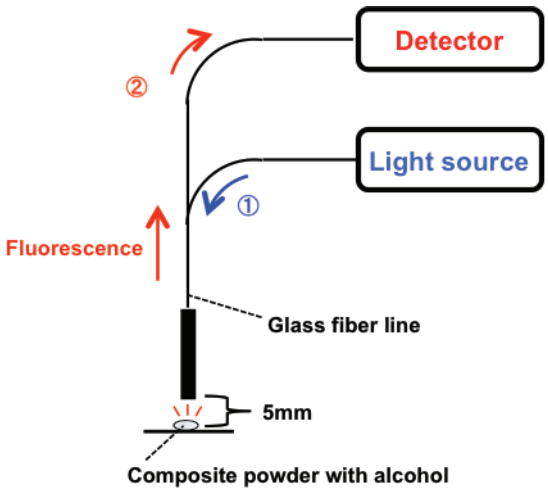

Figure 10. Diagrammatic illustration of solid-state fluorescence measurements.

Preparation of the composite nanofiber film.

1 wt% of **3** in K_2CO_3 were combined with 10 wt% aqueous polyvinyl alcohol, and

the mixture was filled into a glass syringe. The solution was forced from the syringe onto a rotating tubular substrate with application of an electrical field between the syringe needle and the substrate. A self-standing film was obtained after peeling from the substrate.

References

(1) Winquist, F.; Wide, P.; Lundström, I. *Anal. Chim. Acta* **1997**, *357*, 21–31.

(2) Riul, A.; Dantas, C. A. R.; Miyazaki, C. M.; Oliveira, O. N. *Analyst* **2010**, *135*, 2481–2495.

(3) Toko, K. *Biosens. Bioelectron.* **1998**, *13*, 701–709.

(4) Roeck, F.; Barsan, N.; Weimar, U. *Chem.Rev.* **2008**, *108*, 705–725.

(5) Ampuero, S.; Bosset, J. O. *Sensors Actuators B Chem.* **2003**, *94*, 1–12.

(6) Meyerhof, W.; Batram, C.; Kuhn, C.; Brockhoff, A.; Chudoba, E.; Bufe, B.; Appendino, G.; Behrens, M.; Orientale, P.; Bovio, V. *Chem. Senses* **2010**, *35*, 157–170.

(7) Qiu, S.; Wang, J.; Gao, L. **2014**, *62*, 6426–6434.

(8) Cetó, X.; Capdevila, J.; Puig-pujol, A. *Electroanalysis* **2014**, *26*, 1504–1512.

(9) Zawatil, N.; Zakaria, I.; Masnan, M. J.; Zakaria, A.; Shakaff, A. Y. *sensors* **2014**, *14*, 12233–12255.

(10) Rakow, N. A.; Suslick, K. S. *Nature* **2000**, *406*, 710–713.

(11) Zhang, C.; Suslick, K. S. *J. Agric. Food Chem.* **2007**, *55*, 237–242.

(12) Wright, A. T.; Anslyn, E. V. *Chem. Soc. Rev.* **2006**, *35*, 14–28.

(13) James, T. D.; Sandanayake, K. R. A. S.; Shinkai, S. *Angew. Chem. Int. Ed. Engl.* **1994**, *33*, 22072209.

(14) Gale, P.; Gunnlaugsson, T.; Galbraith, E.; James, T. D. *Chem. Soc. Rev.* **2010**, *39*, 3831–3842.

(15) Diehl, K. L.; Anslyn, E. V. *Chem. Soc. Rev.* **2013**, *42*, 8596–8611.

(16) Wiskur, S. L.; Anslyn, E. V. *J. Am. Chem. Soc.* **2001**, *123*, 10109–10110.

(17) Folmer-andersen, J. F.; Kitamura, M.; Anslyn, E. V. *J. Am. Chem. Soc.* **2006**, *128*, 5652–5653.

(18) Edwards, N. Y.; Sager, T. W.; Mcdevitt, J. T.; Anslyn, E. V. *J. Am. Chem. Soc.* **2007**, *129*, 13575–13583.

(19) Lim, S. H.; Feng, L.; Kemling, J. W.; Musto, C. J.; Suslick, K. S. *Nat. Chem.* **2009**, *1*, 562–567.

(20) Yamaguchi, I.; Goto, K.; Sato, M. *Tetrahedron* **2009**, *65*, 3645–3652.

(21) Win, D. T. *AU J.T.* **2006**, *10*, 75–80.

(22) Kimmel, H.; Mages, G. R. *Anal. Chem* **1988**, *60*, 1377–1380.

(23) Kessler, M. A.; Gailer, J. G.; Wolfbeis, O. S. *Sensors Actuators B Chem.* **1991**, *3*,

267–272.

(24) Taylor, P.; Petrova, S.; Kostov, Y.; Jeffris, K.; Rao, G. *Anal. Lett.* **2007**, *40*, 715–727.

(25) Matyushov, D. V; Schmid, R.; Ladanyi, B. M. *J. Phys. Chem. B* **1997**, *101*, 1035–1050.

(26) Liu, L.; Zhang, Y.; Xin, B. *J. Org. Chem.* **2006**, *71*, 3994–3997.

2-2 Molecular Memory System with Phenolic Fluorophore

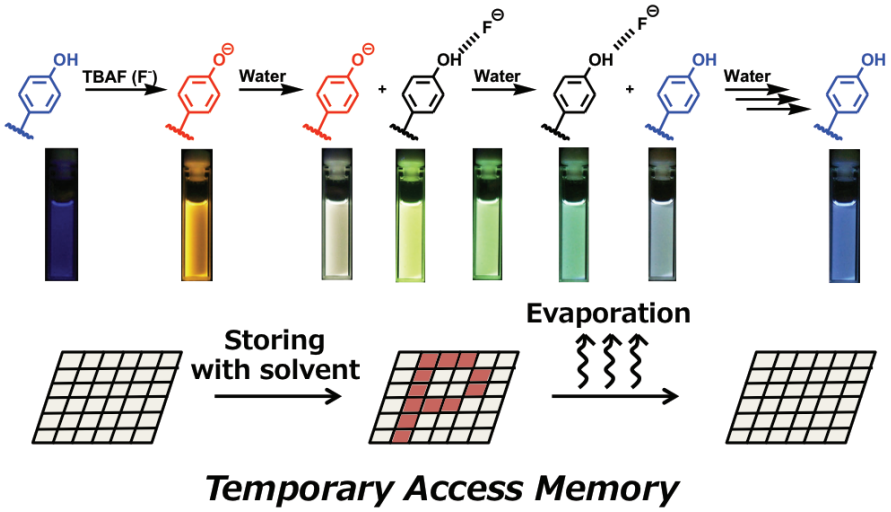

Abstract

Memory operations based on variation of a molecule's properties are important because they may lead to device miniaturization to the molecular scale or increasingly complex information processing protocols beyond the binary level. Molecular memory also introduces possibilities related to information-storage security where chemical information (or reagents) might be used as an encryption key, in this case, acidic/basic reagents. Chemical memory that possesses both volatile and non-volatile functionality requires reversible conversion between at least two chemically different stable or quasi-stable states. In this section, I have developed the phenol–phenoxide equilibrium of phenol fluorophores as a data storage element, which can be used to write or modulate data using chemical reagents. The properties of this system allow data to be stored and erased either in non-volatile or volatile modes. I also demonstrate non-binary switching of states made possible by preparation of a composite containing the molecular memory elements.

2-2-1 Introduction

Data storage devices including disk-based drives and flash media have become an essential part of the modern digital society. Most currently available non-disk memory devices are based on silicon or silicon nitride semiconductor technology with information being stored through application of an electrical bias. Memory devices containing organic components have also been developed due to their easy processability, light weight, and responsivity to an external stimulus.[1] Organic-material-based memories possess significant advantages in that they may be capable of operation not only by application of an electrical bias or magnetic field but also through chemical reaction or external chemical stimuli, for example, host–guest interaction, pH variation or light.[2–10] Usually their use is based on chromophores the optical properties of which can be reversibly toggled by an external stimulus and photo-responsive materials such as azobenzenes, diarylethenes or spiropyrans have been studied.[6–11] Systems based on applied voltages have also been developed and are important since they might be more easily interfaced with existing electronic devices.[12,13] Organic memories also have the potential to operate as switches or memories at the single-molecule level leading to greater storage fidelity and capacity. For example, an electric voltage can be applied to a single molecule of fullerene or a diacetylene derivative using the tip of a scanning tunnelling microscope (STM) enabling modulation of the molecular structures. As a result, they might eventually be adapted to perform memory operations at bit-per-molecule (or greater) information densities.[14,15] Of course, there remain limitations in the implementation of single-molecule devices including difficulties in addressability and operation at ambient temperatures.

Information stored in an organic memory should be retained until an external stimulus is applied since activation energy is required to promote the chemical reaction for switching between the ON and OFF states. For this reason, conventional organic memories based on a reversible reaction are categorized as non-volatile memories (i.e., information is persistent). While non-volatile memories are preferable as storage devices, there also exist possibilities for construction of memories from which information disappears spontaneously, that is, volatile memory.[16] For an organic memory, these may be important from the viewpoint of information security since, for instance, messages or code might be written then undergo automatic deletion on a predetermined timescale. For such a memory system to operate it is required that

information written on the basis of a particular process is gradually and/or spontaneously erased due to a low activation barrier for the reverse reaction. It is, of course, usually a disadvantage for a memory system to undergo "data fading", leading to the deletion of data.[17] However, in the context of a temporary-access memory where data are available momentarily then are deleted, it may be an advantage for the data owner.

Although there have been reports of systems operating using several wavelengths of light so that increasingly large volumes of information might be processed (e.g., by wave-length-division multiplexing[18] and holography[6]), most existing organic memories based on a single chemical change are binary, that is, each chemical state can be arbitrarily assigned 0 or 1 states. Excellent examples of these have been reported including those toggled between memory states by applying light or voltage stimuli.[6–11] If multi-stable organic molecules can be applied then memory capacities might be correspondingly increased while a continuum of states might lead to other advantages. Higher-order memories based on molecules have been reported,[17,19] but the novelty of obtaining a continuum of states has not been investigated.

In order to realize volatile functionality and larger memory capacities, a chemical process in which a readable state changes gradually with low activation energy at each step could be favourable. For this purpose I have focused on the influence of a molecule's environment emphasizing the use of local solvent interactions as an external "stimulus". In relation to this, electronic states of chromophores and chemical equilibrium that determine fluorescence emission wavelengths can be readily tuned by varying the solvent polarity of the prevailing medium. This is more commonly known as solvatochromism or fluorochromism for electronic absorption and fluorescence emission, respectively. With these phenomena in mind, I considered that solvents could be applied to tune in a continuous manner the composition of a solution containing a fluorescent reagent, which is itself in equilibrium with fluorescent products of some reversible reaction (here protonation). This would permit gradual tuning of the resultant solution properties. Although continuous tuning may be contrary to maintenance of discrete memory states, this feature of systems based on my concept represents an advantage for encryption since: 1) a chemical key (or a particular emission color) may be used to define the reconstructed state of encrypted code, and 2) encrypted code could be agglomerated with misleading information available using other keys. In this case,

information can be written and is spontaneously erased depending on solvent composition. A simple solvent evaporation process allows this system to be operated as a chemical temporary access memory (Figure 1). Data retention and information processing using fluorescence as an output relies on similar phenomena to those involved in chemosensing.[20–22] Thus, an applied stimulus (such as the presence of an analyte) causes quenching or emergence of fluorescence the intensity or wavelength of which may be determined by the concentration or identity of the analyte. In the system described here, fluoride (a basic "analyte") is employed.

In order to illustrate the basis of volatile and non-volatile memories, I have adapted the phenol-phenoxide equilibrium (Figure 2b) of the phenol fluorophores, [1,1';4',1'']-ter-phenyl-4''-ol (**1**) and 4'-naphthalen-1-yl-biphenyl-4-ol (**2** ; Figure 2a) as volatile organic memory elements. Addition of a base to the phenol solution causes deprotonation to its phenoxide form. Since the π-orbital structure varies significantly between these two states, fluorescence emission wavelength is shifted dramatically by this process. Subsequently, addition of an acid to the phenoxide form regenerates the phenol. Thus, fluorescence emission wavelength can be varied continuously by controlling the composition of the phenol/phenoxide mixture through addition of an appropriate quantity of an acid. Moreover, the variation of the electronic states of these fluorophores causes large changes in fluorescence colors,[23–27] suggesting a possible means for increasing memory capacities. If water is employed as an acid for storing information, this system can operate as a temporary access memory due to evaporation of solvent. A memory system employing water as the writing reagent could permit highly secure information transmission by way of secret code keys[28] or single-use passwords.[29] In contrast, if information is written in this system using a non-volatile basic substance, operation as a non-volatile memory is obtained. By using these operations, a rewritable, non-volatile memory can be developed where information is written using the base and can be erased using water.

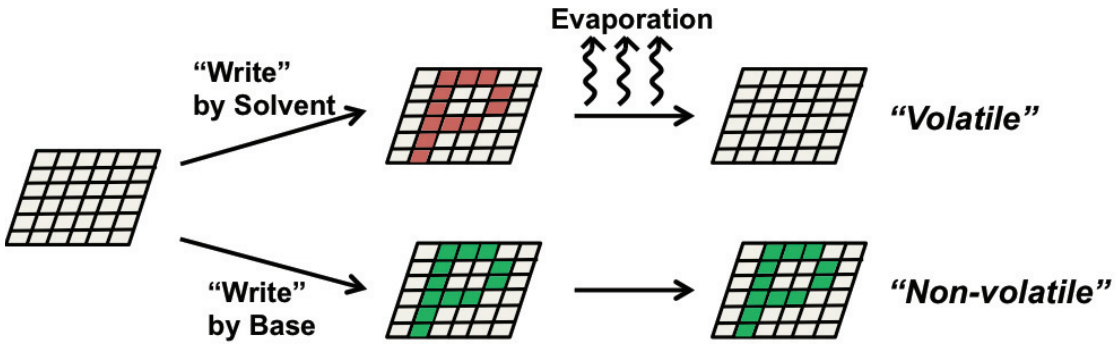

Figure 1. Schematic illustrations of volatile and non-volatile memories.

2-2-2 Results and discussion

2-2-2-1 Variations in fluorescence colors of phenols with addition of base and water

Fluorescence emission hues of the phenolic fluorophores used here range from weak purple–blue (**1**: 363 nm, **2**: 385 nm) to intense green (**1**: 521 nm) or orange (**2**: 562 nm) in THF, respectively, prior to and following addition of excess tetra-*n*-butylammonium fluoride (TBAF) as base (Figure 2c). Additionally, by titration with water, the initial fluorescence color gradually regains its weak purple–blue hue after passing through a variety of colors: sky-blue solutions of **1** or yellow, green and off-white in those of **2**. These fluorescence color variations can be interpreted in terms of the phenoxide forms (produced by treatment with TBAF) gradually regaining their phenol forms during titration with water. Fluorophore **2** exhibits different fluorescence colors, which might eventually correspond to its memory capacity. Fluorescence spectra corresponding to the color changes are also shown (Figure 2d). The photoluminescence maxima of **1** and **2** are red-shifted by approximately 150 nm upon addition of TBAF then are blue-shifted upon titration with water. In case of **2**, recovery of the fluorescence maximum of the phenol form with water titration is apparent at approximately 400 nm. Fluorescence intensity reaches its maximum in the presence of 0.33vol % water then decreases with increasing proportion of water. The mechanism of fluorescence color variation was investigated by using electronic absorption and fluorescence spectrophotometry and NMR spectroscopy.

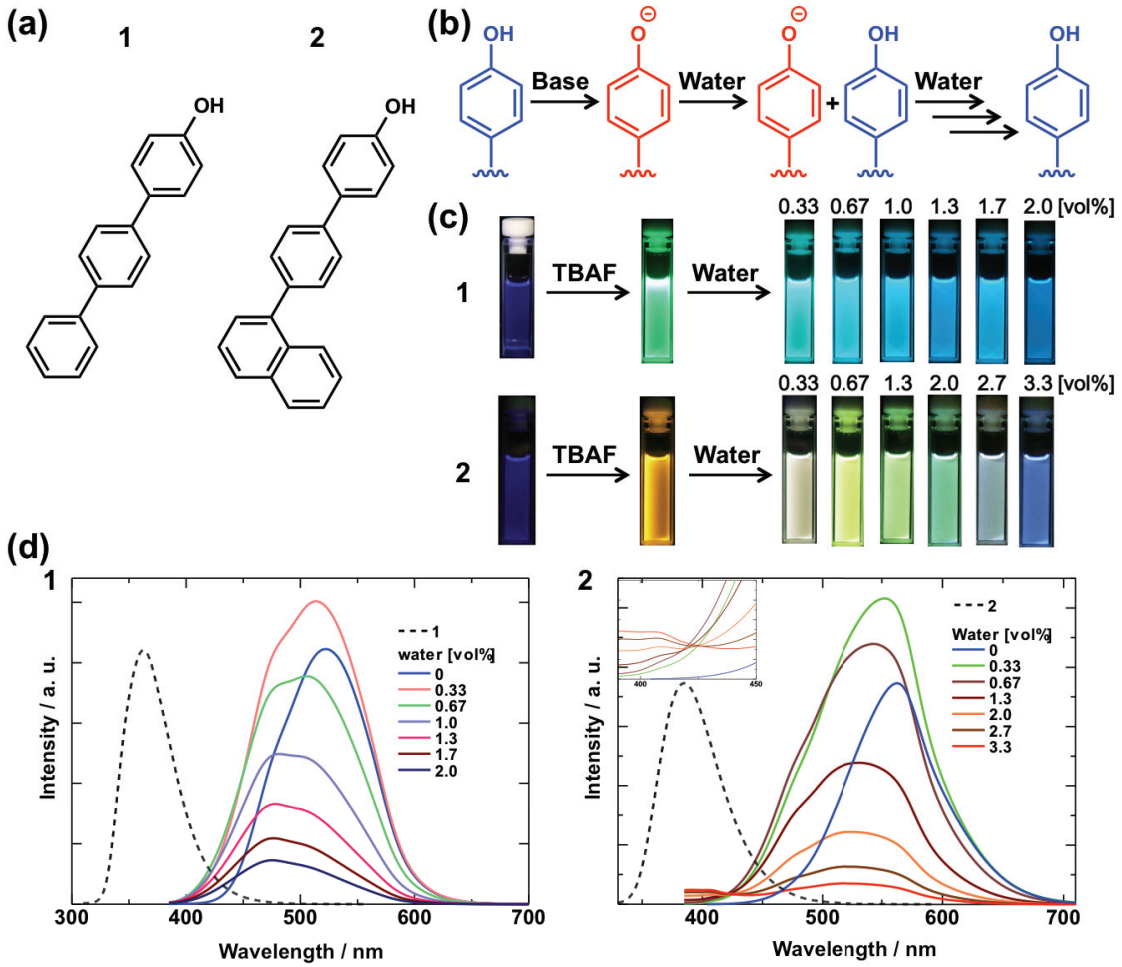

Figure 2. (a) Chemical structures of the phenol derivatives, **1** and **2**. (b) Variation of phenol form dependent on chemical stimulus. (c) Photographs and (d) spectra illustrating the variation of fluorescence color of the phenols upon TBAF/water addition ([**1**] or [**2**] = 1×10^{-4} M in THF, 100eq. TBAF), excitation at λ = 365 nm. In the absence of TBAF, fluorescence maxima of **1** and **2** are 291 nm and 306 nm, respectively. Isosbestic point shown for **2** involves excitation at λ = 365 nm. Emission of the phenol at 390 nm is due to excitation at λ = 291 nm.

2-2-2-2 Mechanism elucidation of the fluorescence color changes

In solutions of **1** or **2**, electronic absorption spectra indicate the existence of another form or intermediate, which is neither phenol nor phenoxide (Figure 3). The absorption maximum of **1** is red-shifted from 292 to 306 nm by titration with 1.0 equiv TBAF. Upon further addition of TBAF, the band progressively decreases in wavelength with concurrent emergence of a new band at 380 nm and formation of an isosbestic

point at 351 nm (Figure 3a and 3b). By adding water to **1** in THF containing 100 equiv TBAF, the absorption band at 380 nm reverted to its initial state (292 nm) through a two-step spectral change similar to the case for TBAF titration (Figure 3c and 3d). Solutions of **2** also exhibit a two-step spectral change with an isosbestic point at 342 nm (Figure A1). The fluorescence emission maximum of **1** shifts in two steps first from 363 to 480 nm then from 480 to 535 nm (Figures A2a and A2b in the Appendix) while that of **2** shifts from 385 to 480 nm, then from 480 to 540 nm (Figures A2c and A2d in the Appendix) on titration with TBAF. In both **1** and **2**, the fluorescence maxima at 480 nm are not derived from either phenol or phenoxide forms. Excitation spectra (with excitation at the fluorescence maximum of solutions containing added water) contain a band at 300–350 nm, indicating the existence of another species, possibly an intermediate between phenol and phenoxide forms (Figures A3 and A4 in the Appendix). Thus, it can be concluded that wavelengths of fluorescence emission maxima of solutions of **1** and **2** are due to their relative compositions of phenol, phenoxide and another species, which varies on addition of water.

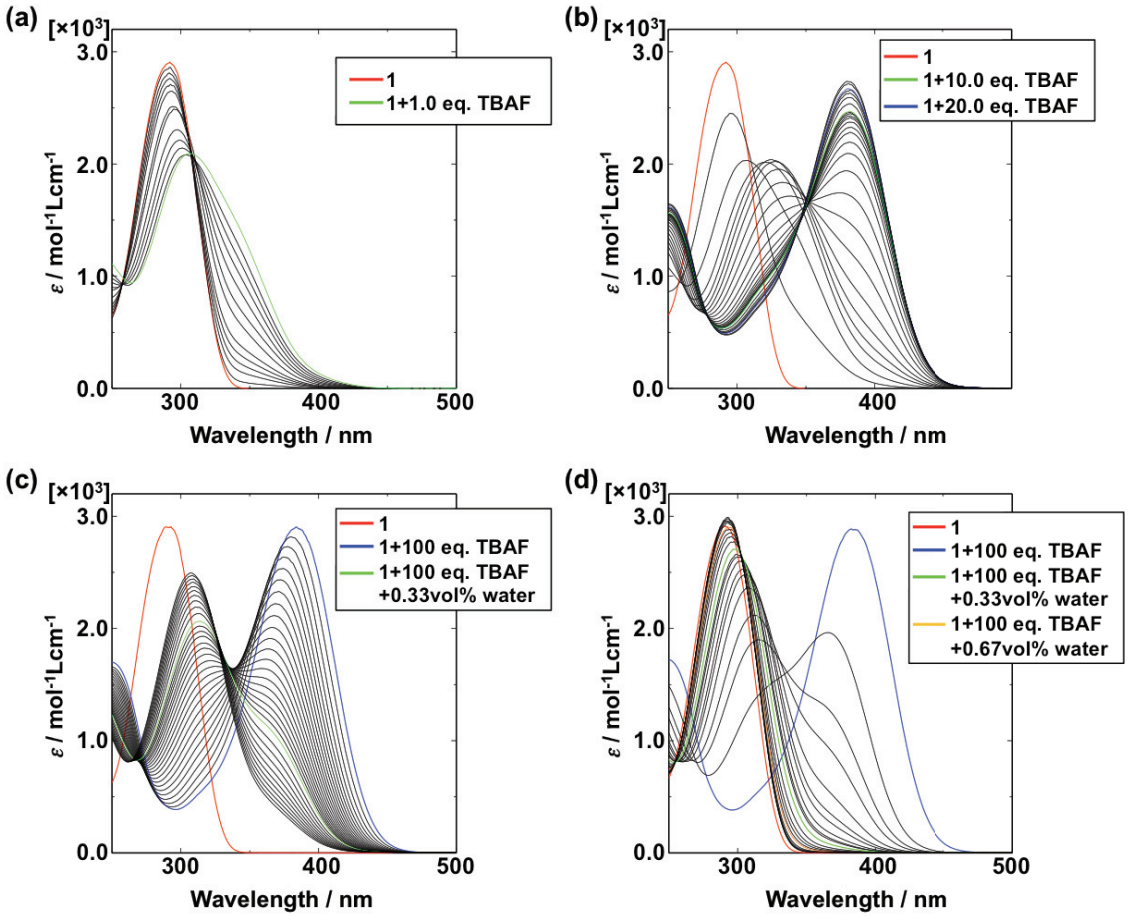

Figure 3. Variations in UV/vis absorption spectra with addition of TBAF and water ([**1**] = 1×10^{-4} M in THF): (a) addition of 0-1.00 eq. TBAF (increments of 0.03 eq. TBAF: 0.05-0.30 eq., increments of 0.10 eq. TBAF: 0.30-1.00 eq.), (b) Addition of 0-10.0 eq. TBAF (increments of 0.50eq. TBAF). (c) Addition of 0-0.62 vol% water to **1** solution containing 100.00 eq. TBAF, (d) Addition of 0-6.2 vol% water to **1** solution containing 100.00 eq. TBAF.

^{1}H NMR spectra of **1** or **2** in [D_8]THF indicate that the phenoxide form generated by addition of excess TBAF reverts to its phenol form on addition of excess water. The peak at 8.27 ppm due to phenolic hydroxyl protons (H_a) of **1** disappears upon addition of 30 equivalents of TBAF due to deprotonation (Figure 4a). Concurrently, the peak due to H_b, which is adjacent to the hydroxyl group, is shifted upfield from its initial position of 6.82 ppm due to formation of phenoxide. The peak due to H_b then shifts downfield upon addition of water with the spectrum finally reverting to that of the phenol in [D_8]THF containing the same quantity of D_2O. Fluorophore **2** behaves similarly (see also Figures A5 in the Appendix). It is known that phenolic protons form hydrogen

bonds with fluoride anions in the presence of TBAF[30–32] and we used ^{19}FNMR spectroscopy to investigate this. As shown in Figure 4b for the case of **1**, upon addition of TBAF a ^{19}F signal corresponding to the expected hydrogen-bonded species emerges at -115 ppm. Addition of further TBAF results in a new signal at -150 ppm due to the presence of HF_2^- in coexistence with phenoxide anions. These observations demonstrate that addition of TBAF results in formation of a phenolic hydrogen-bonded species, with subsequent formation of the phenoxideform.

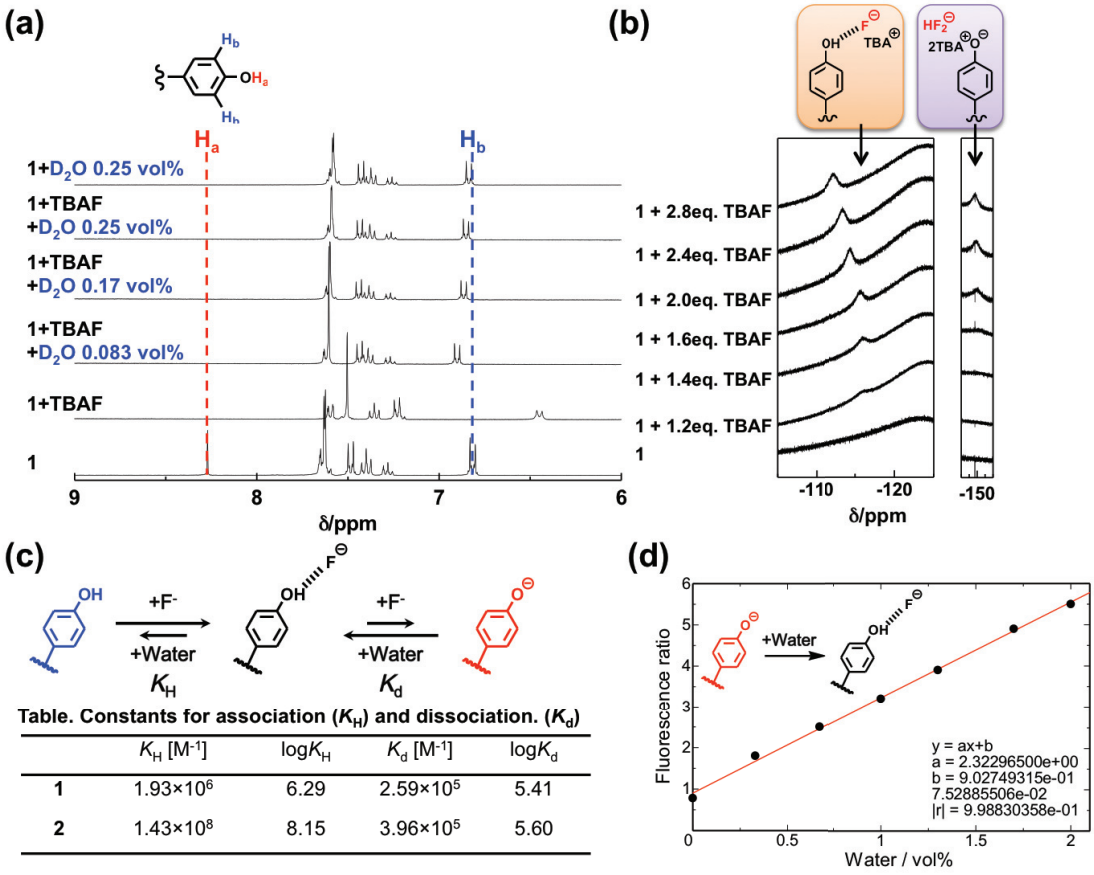

Table. Constants for association (K_H) and dissociation. (K_d)

	K_H [M^{-1}]	logK_H	K_d [M^{-1}]	logK_d
1	1.93×10^6	6.29	2.59×10^5	5.41
2	1.43×10^8	8.15	3.96×10^5	5.60

Figure 4. (a) Variation of the^{1}H-NMR spectrum of **1** upon addition of TBAF and water (THF-d_8, 30eq. TBAF). (b) Variation in the^{19}F-NMR spectrum of **1** in THF-d_8 (at r.t.) upon addition of TBAF. (c) Association (K_H) and dissociation (K_d) constants for **1**. (d) Dependency of the ratio of fluorescence intensities of **1** on quantity of water.

Equilibrium constants for this two-step process were calculated from electronic absorption spectral data.[33] For **1**, the equilibrium constant K_H for the reaction from phenol to hydrogen-bonded species is 1.93×10^6 M^{-1} and for the subsequent reaction to the phenoxide, $K_d = 2.59\times10^5$ M^{-1} (for **2**, $K_H = 1.43\times10^8$ M^{-1} and $K_d = 3.96\times10^5$ M^{-1}; Figure 4c). The values are similar to those already reported,[30–32] supporting our assignment of the species involved. In addition, it was found that the association reaction from phenol form to hydrogen-bonded species is more likely to occur prior to the dissociation reaction from hydrogen-bonded species to phenoxide form (i.e. , $K_H > K_d$).

According to the spectroscopic studies, variation of fluorescence emission color is caused by the mechanism shown in Figure 5. Phenoxide produced by addition of TBAF is converted to a hydrogen-bonded species, and subsequently to its phenol form. This phenol-hydrogen bonded phenol-phenoxide equilibrium system exhibits a range of colors due to the transient state of fluorescence of these three species and variation of its composition by titration with water. The equilibrium constants of reaction indicate that the initial association reaction is less likely than the dissociation reaction (Figure 4c). That is, the stability of the hydrogen-bonded intermediate species against hydrolysis to the phenol fluorophore likely contributes to the gradual variation of the relative composition of the three fluorescent species during addition of water. Fluorescence spectra of **1**, excited at 365 nm can be deconvoluted yielding two emission bands at 480 and 535 nm, respectively, due to the presence of hydrogen-bonded species and phenoxide form (Figures A6 in the Appendix). The ratio of fluorescence intensities ($I_{480/535}$) increases proportionally with increasing quantities of water added, suggesting that the band at 480 nm is due to the addition of water (Figure 4d) in turn indicating that the proportion of hydrogen-bonded species increases with addition of water. For **2**, fluorescence spectra consist of three emission bands at 480nm (hydrogen-bonded species), 540 nm (phenoxide form) and 560 nm, and the ratio of intensities of the bands at 480 and 540 nm increases proportionally with the quantity of water added (Figure A7 and A8 in the Appendix).

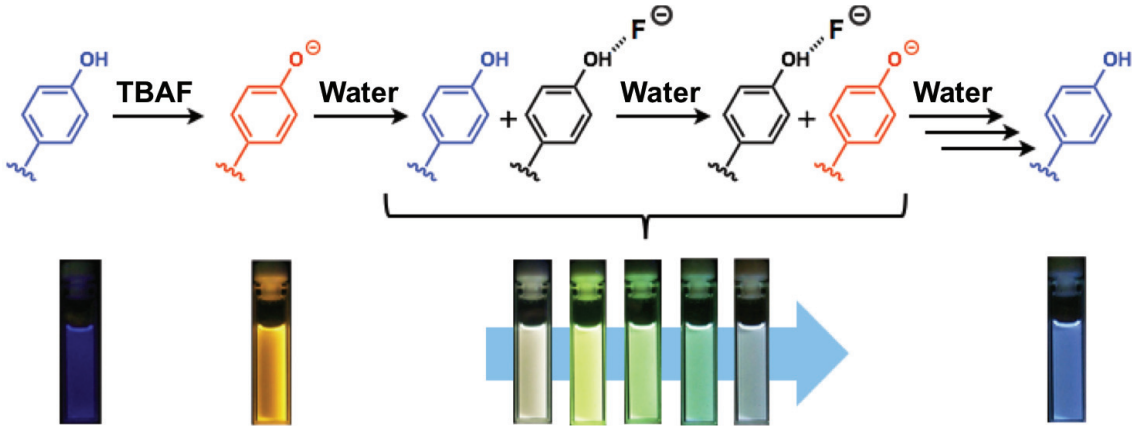

Figure 5. Mechanism of fluorescence color variation of phenol derivatives with TBAF/water addition.

In considering the band at 560 nm, it is assumed that its fluorescence is derived from a new electronic state due to introduction of the naphthalene unit. From electronic absorption spectra, the band due to the phenoxide form of **2** is broader than that of **1**, which indicates that a number of electronic bands exist in the system of **2**. These separated spectra of fluorescence indicate the reaction from phenoxide form to hydrogen-bonded species by adding water. In the system described here, fluorescence intensity increases with addition of small amounts of water then decreases with further addition of water (see Figure 2d). Fluorescence intensity is affected by luminescence efficiency and absorbance of the fluorophore. Values of fluorescence quantum yields of **1** and **2** reveal that luminescence efficiencies are maintained even in the presence of water (Figure 6) so that the variation of fluorescence intensities must originate from changes in absorbance. Liu *et al.*[34] have developed an electronic memory device which was also found to exhibit dependency of its fluorescence emission intensity in the presence of increasing quantities of water.

For a practical demonstration of a memory system using **1** or **2**, excitation wavelength was fixed at 365nm since a common laboratory UV lamp was used as the UV source. This wavelength is closer to the electronic absorption band of hydrogen-bonded species than to that of phenoxide form so that the growth of the band due to hydrogen-bonded species by adding small amounts of water is assumed to enhance intensities of fluorescence. In order to precisely examine changes of absorbance, intensities of excitation spectra at 365 nm were plotted along with amounts of water (Figure 6). Intensities of the excitation spectra increased up to 0.33vol % of

water then decreased at proportions greater than 0.33vol% water, in common with the variations in fluorescence. Additionally, fluorescence intensities of both **1** and **2** decreased monotonically, excited at the maximum absorption wavelength of the phenoxide form (Figure A9 in the Appendix). Therefore, the changes in fluorescence intensities upon addition of water are derived from variations in the overlapping of excitation wavelength with the band of hydrogen-bonded species, as mentioned above.

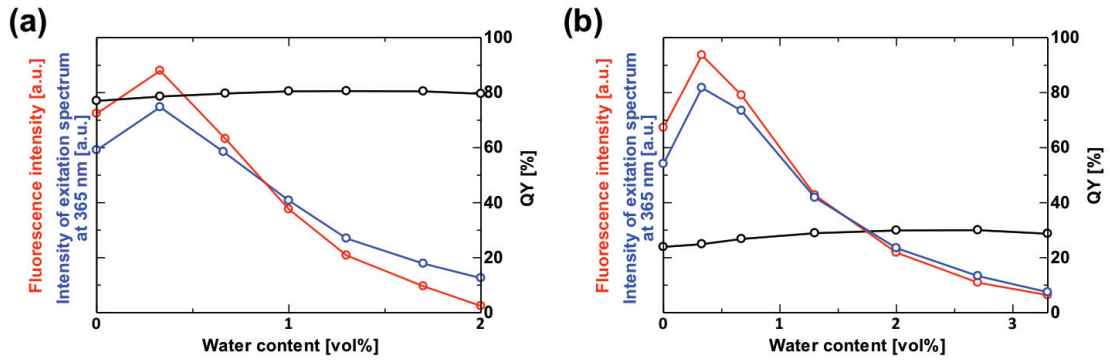

Figure 6. Intensities of fluorescence, excitation spectra at 365 nm and quantum yield to amounts of water in THF solution of (a) **1** or (b) **2**.

2-2-2-3 Solvents effects on the fluorescence color variations with base and water

I also examined variations of fluorescence color in other organic solvents (Figure 7a). In this case, **2** is useful since it exhibits greater variety in its fluorescence emission color and larger differences in color with addition of water than those observed for **1**. Fluorescence emission color was only slightly affected by the polarity of the solvents used. On addition of water, fluorescence color in acetonitrile or acetone exhibited variations similar to that observed for THF. Conversely, in highly polar organic solvents such as DMF and DMSO, fluorescence colors change through white or pale mauve hues. Variation in fluorescence color was assigned according to the standard of the Commission Internaionale de I'Eclairege (CIE).[35] According to the 1934 CIE color coordinate diagram (Figure 7b), the reaction from phenol form to phenoxide form with addition of TBAF leads to a bathochromic shift in fluorescence from blue to orange in all solvents used here. During the reverse reaction from phenoxide form to phenol form, then to hydrogen-bonded species by titration with water, fluorescence colors are

indirectly shifted from orange emission to blue through green. The green fluorescence for **2** is due to the hydrogen-bonded species revealed by deconvolution of fluorescence spectra where a fluorescence band at 480 nm corresponds to a green color. Upon addition of water, CIE coordinates of the fluorescence wavelengths[36] in DMF and DMSO shift more directly to the blue region (phenol form) than in other solvents (THF, acetonitrile and acetone). It is assumed that because solvation of the phenol form is favoured over formation of the hydrogen-bonded species (due to stronger hydrogen bonding with DMF or DMSO), the latter species are unlikely to arise even by adding small amounts of water. As can be seen in the photographs of fluorescent solutions (Figure 7a), larger quantities of water are required to recover to the phenol form in DMF or DMSO than in THF, acetonitrile or acetone. This indicates that the phenoxide form is more stable against addition of water leading to the phenol form in highly polar solvents than in THF, or that these solvents more effectively solvate water molecules attenuating their interaction with the phenoxide. Fluorescence spectra obtained from solutions in these polar organic solvents indicate that similar variations of spectral patterns with addition of water are observed to those in THF, and the wavelengths of fluorescence maximum show larger red-shifts in solvents of greater polarity (Figure 7c). Fluorescence colors of solutions in protic organic solvents such as methanol, ethanol or 1-propanol do not change even on addition of TBAF (Figure A10 in the Appendix). This is due to the decreased probability of phenol deprotonation by TBAF in these solvents. In polar-aprotic and non-polar solvents (e.g., ethyl acetate and dichloromethane, respectively), while fluorescence emission color changes to yellow on addition of TBAF, fluorescence color is not affected by the subsequent addition of water because water is immiscible in these solvents. This phenomenon may facilitate direct observation of interfaces between water and water-immiscible solvents by fluorescence, since the boundary between the two phases can be clearly observed.

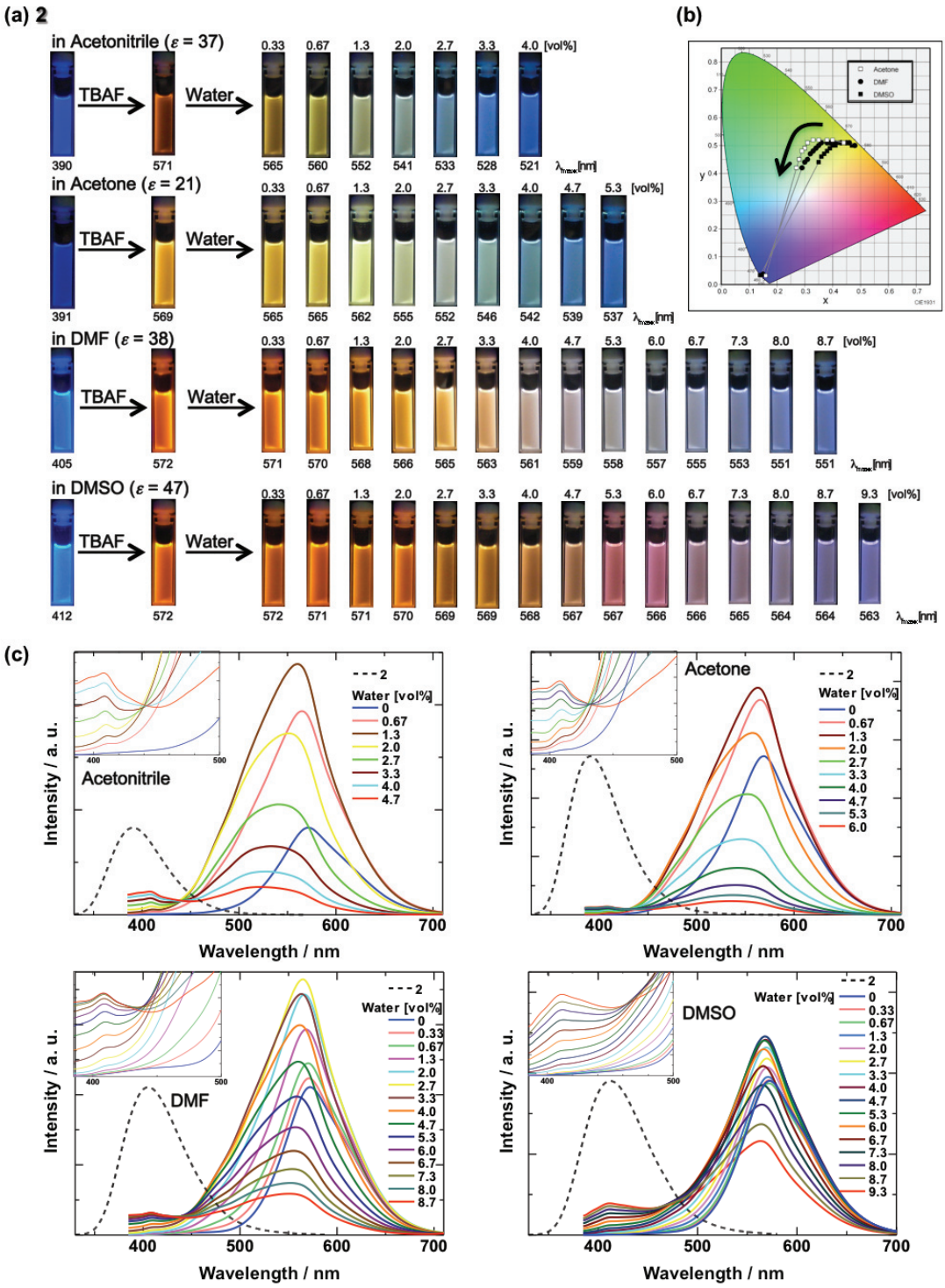

Figure 7. (a) Photographs and (b) Chromaticity diagram with marked coordinates calculated from the fluorescence spectra of **2** in acetone, DMF and DMSO. (c) fluorescence spectra of **2** with water addition (vol%) in different aprotic polar organic solvents (excitation: 365 nm, permittivity of solvent: *e*). The spectra of solutions before and after addition of TBAF are normalized.

2-2-2-4 Fabrications of organic device systems and demonstrations of non-volatile and volatile molecular memory systems

By varying organic solvents and tuning quantities of water, solutions of phenol fluorophores can be fluorescence-wavelength tuned over a wide range of colors indicating the potential information storage properties of these materials. As an illustration of this, pixelated images were constructed using the color variations of **2** available in DMSO. Upon additions of TBAF and/or water, a butterfly form emerges and color variations of its wings can be accomplished chemically (Figure 8a). This result shows that a single substance can be used to express variation of fluorescence color, and the image can be varied simply by addition of TBAF and/or water. These images demonstrate that using sequential changes of fluorescence colors is applicable as a complex data system since a single pixel can be used to store more than two states (i.e., beyond the two states of binary code). Here I chose to demonstrate this aspect using a pixel matrix prepared by hand. Because of this, the information storage data density is necessarily low. Information storage density can be easily increased by using inkjet printing technology for preparing data matrices with resolutions up to 9600×2400 dots-per-inch (dpi) corresponding to an approximate memory density of around 20 Gbitin^{-2}—not competitive with current magnetic technologies. Implementation at the molecular level would increase potential memory density to the Tbin^{-2} level but is currently not practical in this case given the mechanism of memory operation.

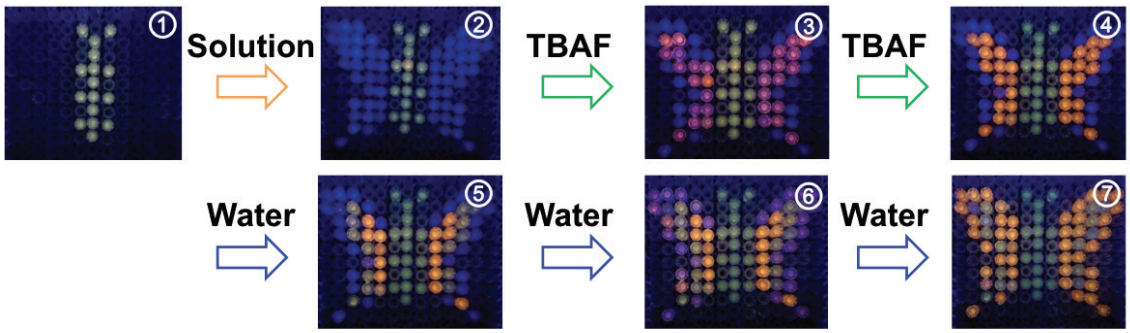

Figure 8. (a) Photographs composed of individual pixels (pixel size: ~2 mm ∅) containing **2**, TBAF, water and different organic solvents with excitation at 365 nm. Solutions of **2**, 100 eq. TBAF and 1.3 vol% of water in THF (1) and of **2** in DMSO (2) were filled in each pixel, and TBAF (3, 4) and water (5, 6, 7) were added.

The development of a practical memory device was attempted by immobilization of the reagents as an organogel composite, where the phenol fluorophores are distributed uniformly within the gel. Previously, our group has reported on use of gel immobilization of chromophores[37] although, in that case, the porphyrin fluorophore used is considerably less flexible (in terms of its emissive properties) than the phenol fluorophores reported here. Gelatinous materials have the advantage that they can be freely shaped or deposited in the required form. Furthermore, in the context of this work, information erasure rate can be varied by applying solvents of different volatilities. By adding the organogelator, lauroyl-L-glutamic-α,γ-dibutyl-amide into a solution of **2** in THF, gelation of the resulting composite occurs and the corresponding purple–blue or yellow fluorescence could also be observed in the gel state in the presence or absence of TBAF, respectively (Figure 9a). The organogel composite containing **2** in DMSO containing TBAF also exhibited yellow fluorescence and there was no significant difference in fluorescence colors from solvent to solvent. The organogels could be deposited on filter paper and the solvent removed yielding gel-infiltrated paper. On this study, solvents were used for writing did not diffuse significantly due to the gel state so that information could be written accurately by applying a solution of TBAF in THF or neat solvents in predetermined patterns as shown in Figure 8. Information was written on paper containing **2** using a brush that had been soaked in a solution of TBAF (Figures 9b and 9c). Since TBAF is involatile this writing process leads to non-volatile memory. The information could be subsequently erased by application of water. Thus, the memory also has a re-writeable functionality. On the other hand, the filter paper infiltrated with organogel composite containing **2** already uniformly treated with TBAF can likewise be written on non-volatilely by applying a TBAF-soaked brush. Applying a water-soaked brush can also be used to store information on the TBAF-treated filter paper. Thus, information written in TBAF/**2** gradually disappears due to evaporation of water (Figure 9c). In that case, the filter paper behaves as a "volatile" or temporary access memory, and information is not retained. In this case, use of the simple filter paper medium precludes extended use of the memory with only a few write/rewrite cycles being possible. Incorporation of **2** in a polymer matrix will permit greater durability (I am now testing these systems). Another aspect of this system that I are considering is the appearance of waste products of the reactions, which may interfere with subsequent switching operations or eventually render the memory ineffective. This

may require redesign of the chromophore so that different anionic species can be used to toggle the fluorescence color.

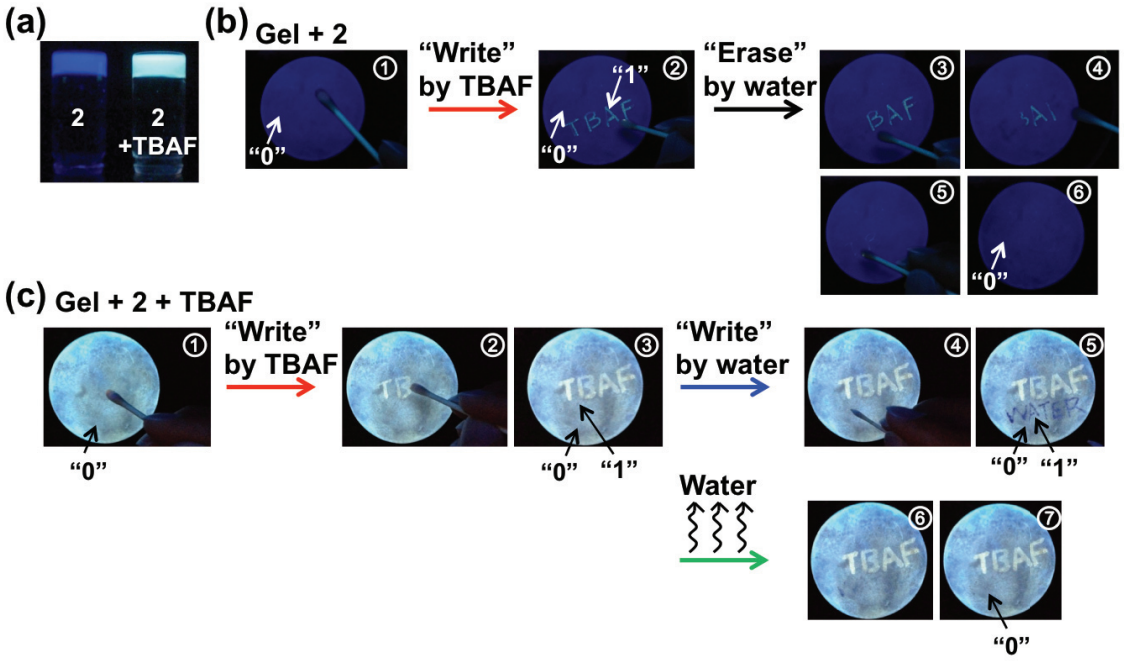

Figure 9. (b) Organogel composites of **2** in THF with lauroyl-L-glutamic-α,γ-dibutylamide containing with (left) and without (right) TBAF. (c, d) Photographs of information 'writing' or 'erasing' on gel-embedded filter papers (∅ = 125 mm) with excitation at 365 nm; (c) On a filter paper embedded with the organogel solution of **2**, information was written by applying TBAF (2), then erased with water (3, 4, 5, 6). (d) On a filter paper embedded with the organogel containing TBAF, information was written by applying TBAF or water (2, 3; 4, 5). The information stored using water was automatically erased after 5 minutes by evaporation of water (6, 7).

2-2-3 Conclusions

In conclusion, I have demonstrated a chemical temporary access memory capable of storing information using fluorescence color variation of phenol fluorophores (**1** and **2**) by treatment with TBAF and/or water. The memory operates in temporary-access mode because of the volatility of the (protic) solvent used for writing. Thus, the use of increasingly non-volatile solvents can be used to vary temporal access to information. Additionally, this system can be used to store a variety of information as individual fluorescent colors, which are derived from the bulk gradual deprotonation of phenol to a known hydrogen-bonded species then to the phenoxide. These systems where information is only temporarily available might permit highly secure information transmission, by way of secret code keys or single-use passwords. In addition, variation of the fluorescence emission color of these phenol/phenoxide couples by addition of water may prove useful for visualization of solvent diffusion in two dimensions or for measurement of ambient water content so that humidity might be assessed using the naked eye and an appropriately designed humidity indicator film. As with many of the available organic or single-molecule-memory systems, actual application is not currently practical. Despite, this I believe that my work demonstrates the inherent flexibility of organic compounds and, in particular, organo-gelatinous states in the search for useful materials.

2-2-4 Experimental part

Materials and measurements.

Solvents and reagents were purchased from Tokyo Chemical Industry Co. Ltd. (Tokyo, Japan) or Wako Pure Chemical Co. (Osaka, Japan) and were used without further purification. All reaction mixtures and fractions eluted by column chromatography eluents were monitored using thin layer chromatography (glass backed (TLC) plates (Kieselgel 60 F254). The developed thin layer chromatography plates were observed under UV light at 254 and 365 nm. Flash column chromatography over silica gel (LC60A35-70 μM) was used for all separations. ^{1}H, ^{13}C and ^{19}F NMR spectra were measured at 298 K from DMSO-d_6 or THF-d_8 solutions of the samples using a JEOL model AL300BX (300 MHz) spectrometer with Me_4Si as internal standard. Chemical shifts (δ) and coupling constants (J) are given in parts per million and Hertz, respectively. ESI-MS spectra were measured using a JASCO model JMS-T100CS. HRMS (ESI-positive) spectra were measured using a JEOL model JMS-MS700. UV/vis absorption spectra were measured using a Shimadzu model UV-3600 UV-VIS-NIR. Fluorescence spectra were measured using a JASCO model FP-6500.

Synthesis and structural characterization.

Preparation of phenolic dye **1** has been reported previously.[25] Phenolic dye **2** was synthesized by Suzuki-Miyaura cross coupling reaction.[38]

[1,1';4',1'']Terphenyl-4''-ol (1)

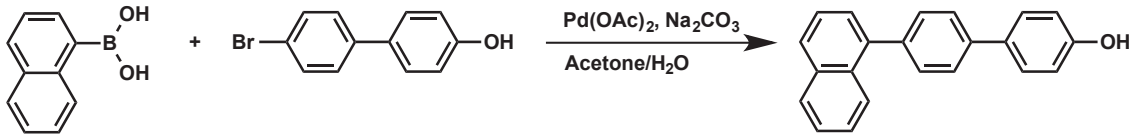

2 (66%)

^{1}H-NMR (300 MHz, DMSO-d_6, 298 K): 6.88 (d, 2H, J = 9.0; Ar-H), 7.37 (t, 1H, J = 6.0; Ar-H), 7.48 (t, 2H, J = 6.0; Ar-H), 7.54 (d, 2H, J = 9.0; Ar- H), 7.60-7.52 (m, 6H; Ar-H), 9.60 (s, 1H; phenol-OH). ^{13}C- NMR (75 MHz, DMSO-d_6, 298 K): 115.77, 126.39, 126.43, 127.04, 127.34, 127.64, 128.95, 130.27, 138.01, 139.21, 139.72, 157.24. MS (ESI): m/z = 245.11 $[M-H]^-$, 491.21 $[2M-H]^-$.

4'-Naphthalen-1-yl-biphenyl-4-ol (2)

A mixture of Na_2CO_3 (0.212 g, 2.0 mmol), $Pd(OAc)_2$ (0.001 g, 0.5 mol %), 4-bromo- 4'-hydroxybiphenyl (0.249 g, 1.0 mmol), 1-naphthylboronicacid (0.206 g, 1.2 mmol), distilled water (10 mL) and acetone (8.5 mL) was stirred for 3 hours at room temperaure. Solvents were removed under reduced pressure and the residue was treated with dilute aqueous HCl aq. The precipitate was filtered and washed with water. The residue was then subjected to column chromatography (SiO_2, THF) yielding **2** as white powder (0.194 g) in 66% yield. ^{1}H-NMR (300 MHz, DMSO-d_6, 298 K): 6.89 (d, 2H, J = 6.0; Ar-H), 7.45-7.64 (m, 8H; Ar-H), 7.74 (d, 2H, J = 6.0; Ar-H), 7.89 (d, 1H, J = 9.0; Ar-H), 7.93-8.05 (m, 2H; Ar-H), 9.61 (s, 1H; phenol-OH). ^{13}C-NMR (75 MHz, DMSO, 298 K) : 115.99, 125.43, 125.76, 126.08, 126.14, 126.51, 126.96, 127.74, 127.91, 128.53, 130.37, 130.61, 131.01, 133.64, 138.12, 139.36, 139.43, 157.43. MS (ESI): *m/z* = 295.11 $[M-H]^-$, 591.23 $[2M-H]^-$. HRMS (ESI) *m/z* calcd for $C_{22}H_{15}O$ $[M-H]^-$: 295.1122, found 295.1136.

Preparation of memory papers using phenol fluorophore.

Organogelator lauroyl-L-glutamic-α,γ-dibutylamide (40 mg) wasaddedto 1×10^{-4} M **2** in THF(1.0 mL) solution containing 30 eq. TBAF. The gelator was dissolved by heating, and the solution was allowed to stand for 1 day in order to test gelation. Organogels of the solutions were obtained regardless of the presence of TBAF. The gel was returned to its solution state by heating, and the solution was used to coat the filter papers. Solvent was slowly evaporated by allowing the filter paper to stand in air giving the memory paper.

References

(1) Kim, W. T.; Yang, T.; Li, F.; Kwan, L. W. *NPG Asia Mater.* **2012**, *4*, 1–12.

(2) de Silva, P. H. A.; Nimal Gunaratne, Q.; Gunnlaugsson, T.; Huxley, M. A. J.; Rademacher, J. T.; Rice, T. E. *Chem. Rev.* **1997**, *97*, 1515–1566.

(3) Lavin, M. J.; Shimizu, D. K. *Chem. Commun.* **2007**, *3*, 228–230.

(4) Pina, F.; Melo, J. M.; Maestri, M.; Ballardini, R.; Balzani, V. *J. Am. Chem. Soc.* **1997**, *119*, 5556–5561.

(5) Sindelar, V.; Silvi, S.; Kaifer, E. A. *Chem. Commun.* **2006**, *20*, 2185–2187.

(6) Saishoji, A.; Sato, D.; Shishido, A.; Ikeda, T. *Langmuir* **2007**, *23*, 320–326.

(7) Pariani, G.; Castagna, R.; Dassa, G.; Hermes, S.; Vailati, C.; Bianco, A.; Bertarelli, C. *J. Mater. Chem.* **2011**, *21*, 13223–13231.

(8) Uchida, K.; Saito, M.; Murakami, A.; Nakamura, S.; Irie, M. *Adv. Mater.* **2003**, *15*, 121–125.

(9) Wu, Y.; Xie, Y.; Zhang, Q.; Tian, H.; Zhu, W.; Li, D. Q. A. *Angew. Chem. Int. Ed.* **2014**, *53*, 2090–2094.

(10) Raymo, M. F.; Alvarado, J. R.; Giordani, S.; Cejas, A. M. *J. Am. Chem. Soc.* **2003**, *125*, 2361–2364.

(11) Irie, M.; Fukaminato, T.; Sasaki, T.; Tamai, N.; Kawai, T. *Nature* **2002**, *420*, 759–760.

(12) Pischel, U.; AndrØasson, J. *New J. Chem.* **2010**, *34*, 2701–2703.

(13) de Ruiter, G.; Tartakovsky, E.; Oded, N.; van der Boom, E. M. *Angew. Chem. Int. Ed.* **2010**, *49*, 169–172.

(14) Donhauser, J. Z.; Mantooth, A. B.; Kelly, F. K.; Bumm, A. L.; Monnell, D. J.; Stapleton, J. J.; Price, W. D. Jr.; Rawlett, M. A.; Allara, L. D.; Tour, M. J.; Weiss, S. P. *Science* **2001**, *292*, 2303–2307.

(15) Nakaya, M.; Tsukamoto, S.; Kuwahara, Y.; Aono, M.; Nakayama, T. *Adv. Mater.* **2010**, *22*, 1622–1625.

(16) Pina, F.; Roque, A.; Melo, M. J.; Maestri, M.; Belladelli, L.; Balzani, V. *Chem. Eur. J.* **1998**, *4*, 1184–1191.

(17) de Ruiter, G.; Wijsboom, H. Y.; Oded, N.; van der Boom, E. M. *ACS Appl. Mater. Interfaces* **2010**, *2*, 3578–3585.

(18) Nagatsu, N.; Okamoto, S.; Sato, K. *IEEE J. Select. Areas Commun.* **1996**, *14*, 893–902.

(19) de Ruiter, G.; Motiei, L.; Choudhury, J.; Oded, N.; van der Boom, E. M. *Angew. Chem. Int. Ed*. **2010**, *49*, 4780–4783.
(20) Kumar, M.; Kumar, R.; Bhalla, V. *RSC Adv.* **2011**, *1*, 1045–1049.
(21) Guo, Z.; Zhu, W.; Shen, L.; Tian, H. *Angew. Chem. Int. Ed.* **2007**, *46*, 5549–5553.
(22) Lu, W.; Zhang, M.; Liu, K.; Fan, B.; Xia, Z.; Jiang, L. *Sensors Actuat. B* **2011**, *160*, 1005–1010.
(23) Gareis, T.; Huber, C.; Wolfbeis, S. O.; Daub, J. *Chem. Commun.* **1997**, *18*, 1717–1718.
(24) Fan, Y.; Zhu, M. Y.; Dai, R. E.; Zhang, Y. L.; Chen, N. Z. *Dalton Trans.* **2007**, *35*, 3885–3892.
(25) Yamaguchi, I.; Goto, K.; Sato, M. *Tetrahedron* **2009**, *65*, 3645–3652.
(26) Naumov, P.; Kochunnoonny, M. *J. Am. Chem. Soc.* **2010**, *132*, 11566–11579.
(27) Mori, T.; Akamatsu, M.; Okamoto, K.; Sumita, M.; Tateyama, Y.; Sakai, H.; Hill, P. J.; Abe, M.; Ariga, K. *Sci. Technol. Adv. Mater.* **2013**, *14*, 015002–1.
(28) Huang, Z. J.; Yin, Q. Z.; Wang, S.; Li, W. H.; Chen, W.; Han, F. Z. *Eur. Phys. J. D* **2012**, *66*, 1–5.
(29) Lee, J. S.; Lee, S. J.; Lee, M.; Lee, J. S.; Choi, D.; Kim, D. K. *ETRI Journal* **2011**, *33*, 611–620.
(30) Clark, H. J.; Cork, G. D. *J. Chem. Soc. Chem. Commun.* **1984**, *15*, 1014–1015.
(31) Clark, H. J.; Cork, G. D.; Tinsdale, J. A. *Spectrochim. Acta A* **1986**, *42*, 815–819.
(32) Jose, A. D.; Kar, P.; Koley, D.; Ganguly, B.; Thiel, W.; Ghosh, H. N.; Das, A. *Inorg. Chem.* **2007**, *46*, 5576–5584.
(33) Agbaria, A. R.; Butterfield, T. M.; Warner, M. I. *J. Phys. Chem.* **1996**, *100*, 17133–17137.
(34) Liu, Y.; Zhang, Y.; Lan, Q.; Liu, S.; Qin, Z.; Chen, L.; Zhao, C.; Chi, Z.; Xu, J. *J. Economy. Chem. Mater.* **2012**, *24*, 1212–1222.
(35) C. I. E. Chromaticity Diagram: http://hyperphysics.phy-astr.gsu.edu/hbase/vision/cie.html#c2; last accessed February 3rd, 2012.
(36) For example: Damaceanu, M.-D.; Constantin, C.-P.; Bruma, M.; Pinteala, M. *Dyes Pigm.* **2013**, *99*, 228–239.
(37) Shundo, A.; Hill, P. J.; Ariga, K. *Chem. Eur. J.* **2009**, *15*, 2486–2490.
(38) Liu, L.; Zhang, Y.; Xin, B. *J. Org. Chem.* **2006**, *71*, 3994–3997.

Chapter 3
Development of Novel Optical Systems for Detection of Radioactive Cesium using Supramolecular Probes

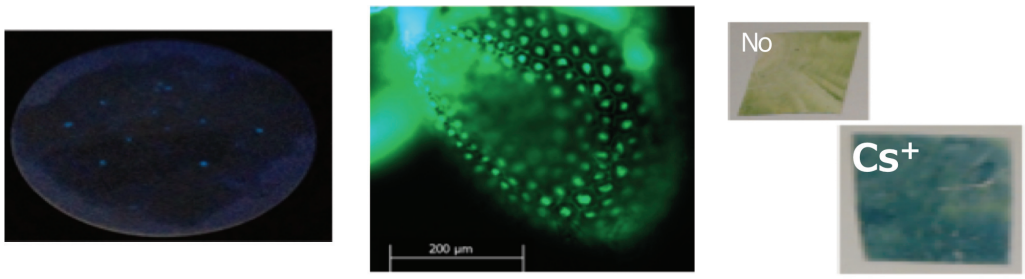

Abstract

In this chapter, optical cesium sensor systems based on supramolecular chemistry are described. The accident at the Fukushima Daiichi nuclear power plant, which was one of the most serious adverse effects of the Great East Japan Earthquake, was accompanied by the release of a large quantity of radioactive materials including ^{137}Cs to the environment. A detection of cesium has been needed on soil, in water systems and also in the body. If cesium (also radiocesium) could be detected optically, then its environmental remediation would be facilitated. Supramolecular material approaches, such as host-guest chemistry, are useful in the design of high-resolution molecular sensors and can be used to convert molecular-recognition processes into optical signals. In this work, I have developed molecular materials (here, phenols) as an optical probe for cesium cation-containing particles with implementation based on simple spray-on reagents and a commonly available fluorescent lamp for naked-eye detection in the solid state and the cell of a plant. This chemical optical probe provides a higher spatial resolution than existing radioscopes and gamma-ray cameras. In addition, Cs^+ in aqueous media was detected with an optode membrane. This is useful for examination of environmental water, contaminated by the leak of radioactive materials.

3-1 Introduction

Cesium-133 is the heaviest stable alkali metal and it has had only a few significant applications, such as in atomic clocks[1] or as gradient centrifugation reagents.[2] More recently, however, cesium compounds as their brines have emerged as important materials for deep drilling operations due to the high densities of their solutions[3] and their relatively low toxicity.[4] Radiocesium, on the other hand, including the two longer-lived isotopes of cesium Cs-134 (half-life 2.07 years) and Cs-137 (half-life 30.17 years), is a major source of environmental contamination in the vicinity of radiation leaks such as those which occurred at Chernobyl, Ukraine,[5] and more recently at Fukushima, Japan.[6, 7] During nuclear reactor breaches, iodine I-131 (half-life 8.02 d) is released to the atmosphere.

In addition to the well-known nuclear reactor disasters, radiocesium has been more gradually introduced into the biosphere through nuclear weapons testing over the last 60 years.[8] Dual environmental hazards are presented by radiocesium in that background radiation exposure is increased and, more significantly, it is known to be bioaccumulated, leading to a much greater risk of carcinogenesis in organisms.[9] Although cesium is gradually eliminated from mammals when it is removed from dietary sources, levels of corporeal contamination may be maintained or increased in cases of chronic pollution surrounding nuclear disaster areas, where locally grown agricultural produce certainly contain significant amounts of radioactive contaminants. Uptake of radiocesium by cultivated plants is therefore a significant source of risk to local populations[10] since radiocesium is usually simply left to decay, meaning that radiation leaks (and nuclear weapons tests) result in major legacies of environmental contamination.[11]

Following three systems are mainly considered as the contamination spots.

(a) Ground soil in the solid state

(b) Sea and ground water

(c) In the body

Cs-137 is released as a microparticulate aerosol leading to long-term soil and water contamination.[12] Moreover, water system is also contaminated because cooling water for the reactors of nuclear reaction, containing Cs-137 has been leaked to sea and ground water. On the other hand, although contamination of living things (also foods) by Cs-137 is a serious problem for our life, uptake behavior of Cs-137 in the body has

not been clarified sufficiently.

Areas contaminated by accumulated Cs-134 and Cs-137 can be monitored from over-flying aircraft and, in Japan, both public agencies and non-governmental organizations undertake such measurements. Although the Japanese government is planning and implementing radioisotope decontamination operations, the serious problem of waste treatment remains. For instance, Toshiba[13] and JAXA[14] are developing a gamma ray camera to visualize radioactivity. However, these techniques do not show the existence of cesium with a high-resolution image, and are unable to examine in water systems. Since cesium is released during reactor breaches in a particulate form it would be useful if these particulates could be detected within large volumes of contaminated ground soil in the solid state. Thus, detection of cesium with a high resolution enables efficient elimination of radioactive materials. Moreover, with the high-resolution imaging technique, cesium in the body can be mapped. And, the measurement in water systems is useful for checking contaminated sea and ground water. Here, host-guest supramolecular materials promise simple detection of a variety of chemical species, especially specific ions.[15–18] Host–guest interactions may be converted into detectable signals such as electrical and optical outputs while, for instance, fluorescent molecular sensing materials provide greater spatial resolution.[19–21] In addition, chemical sensors can be carried out in solvent system such as water and organic solvents. Thus, this supramolecular strategy would be suitable for the cesium detection.

In this work, I have adopted the deprotonation of phenols as a probe reaction for detecting alkali metal cations. Phenols are a notable class of organic compound because of the acidity of their hydroxyl protons.[22] Thus, deprotonation can occur by treatment with an inorganic base (e.g. Na_2CO_3, K_2CO_3) yielding a phenolate anion with associated countercation such as Na^+ or K^+. For substituted phenols, such as 4-hydroxy-1-biphenyl and 1-hydroxy-4,4',4''-terphenyl [HTP; 1-(4'-hydroxy phenyl)-4-phenylbenzene], substantial changes in fluorescence emission spectra are observed upon deprotonation,[23, 24], which are strongly affected by the nature of the substituent, solvent and deprotonating reagent. Furthermore, intermolecular processes such as fluorescence resonance energy transfer (FRET)[25] or excimer emission[26] can be designed into molecules to optimize or tune any sensing output signal. Using these features, I initially designed a class of HTP sensing elements and compounded one of them with an

electron-accepting 4-nitrophenyl ether (4-NPE) group through a variable-length polyethylene glycol chain with the aim of selectively detecting alkali metal or alkali earth metal cations. Figure 1 shows the chemical structure of 4-NPE-substituted HTP **1**, which contains a tetraethylene glycol (TEG) linker separating the two aromatic moieties. Cesium cation-containing particles can be visualized after spraying with **1** in methanol. Significantly, because of my molecular design, the probe is selective for cesium cations making it useful for the detection of cesium in the environment and the body of the plant (cellar imaging). The probe is particularly suitable for detecting cesium salts in particulate form and allows them to be detected in the solid state with the naked eye. Moreover, I have tried detection of cesium in an aqueous solution by using an optode method, which is based on cation extraction from aqueous phase to polymer film.

3-2 Results and discussion

3-2-1 Selective detection of cesium in solid state using a novel fluorescence probe

Figure 1 illustrates the selective sensing activity of **1** including its solid-state fluorescence response to the presence of Cs^+ (Figure 1a). Figure 1b shows the difference in fluorescence emission color from **1** in the presence of Li^+, Na^+, K^+ or Cs^+ (as their carbonate salts), following exposure to methanol by spraying a small amount of the solvent on the powdered solid.[6] The absence of fluorescence in the presence of Mg^{2+} and Ca^{2+} is also shown (Figure 1b). Green fluorescence due to the presence of Cs^+ on dry soil is shown after spraying of a solution of **1** in methanol so that the contaminated site can be easily identified and removed from the surrounding material (Figure 1c). In addition, Cs^+ particles can be visualized after spraying with **1** in methanol (see Figure 1d).

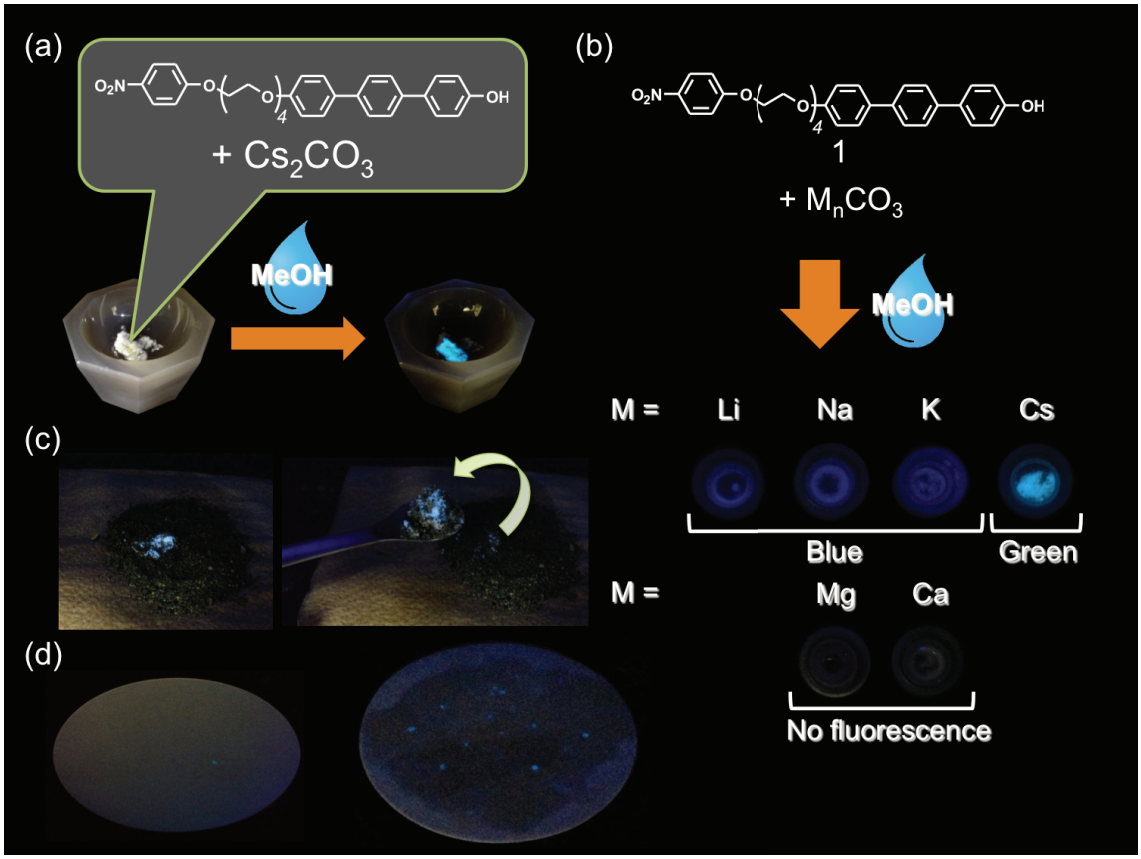

Figure 1. Photographs of fluorescence changes of a mixture of **1** and various carbonate salts after addition of a drop of methanol. (a) Fluorescence change of a powdered mixture of **1** and Cs_2CO_3 under UV irradiation (365 nm) after addition of a drop of methanol. (b) Photographs of a mixture of **1** and various carbonate salts under UV irradiation (365 nm) after addition of a drop of methanol. (c) Photographs of **1** + Cs^+ on dirt under room light (left) and under UV irradiation (365 nm, right) after spraying with methanol. (d) Photographs of **1** + Cs^+ particles on filter paper (diameter 110 mm) under UV irradiation (365 nm) after spraying with methanol.

The limit of detection for Cs^+ should depend on several parameters including counteranion, local pH and intercalation of Cs^+ into clay contained in ground soils. I estimate a detection limit of 1ppm under ideal conditions (see Figure 2). This limit is significant since cesium is present in the Earth's crust at 1ppm: detection of cesium concentrations above this level would indicate possible local contamination. From Figure 2, it is evident that the wavelength of the fluorescence emission maximum is dependent on the concentration of Cs^+ present making construction of a calibration curve possible. The form of the calibration curve suggests that concentrations of Cs^+ far lower than 1ppm could be detected, although this is not necessarily useful from a practical perspective. The importance of the connectivity of 4-NPE in **1** was investigated by comparing its response to that of a physical mixture of a triethylene glycol-substituted terphenol (**3TEG**), a simple ether of 4-nitrophenol (**10**) and the respective alkali metal carbonates in the presence of methanol (see Figure 3). Notably, the green fluorescence characteristic of the presence of Cs^+ in **1** was not observed, and all metal carbonates (Na^+, K^+ or Cs^+) gave the standard blue fluorescence in the solid state moistened with methanol. This further demonstrates that Cs^+ binding to **1** differs from that of the other alkali metal cations leading to the specificity in its fluorometric response.

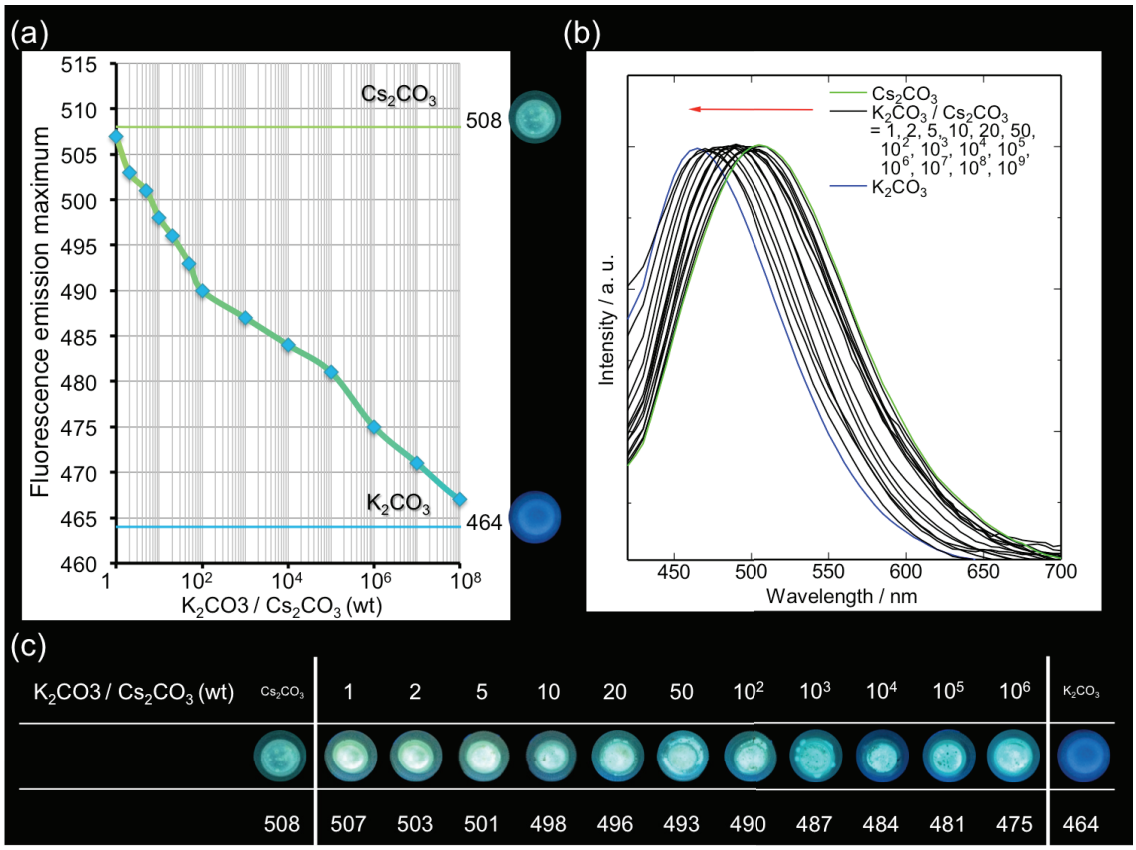

Figure 2. Detection limit of Cs_2CO_3 by using **1**. (a) Photographs and plot of fluorescence emission maxima wavelengths for mixtures between **1** and Cs_2CO_3/K_2CO_3 under UV irradiation (365 nm) after addition of a drop of methanol. (b) Fluorescence spectra of mixtures used to construct the plot in (a). (c) Photographs and emission maxima for mixtures between **1** and Cs_2CO_3/K_2CO_3 under UV irradiation (365 nm) after addition of a drop of methanol.

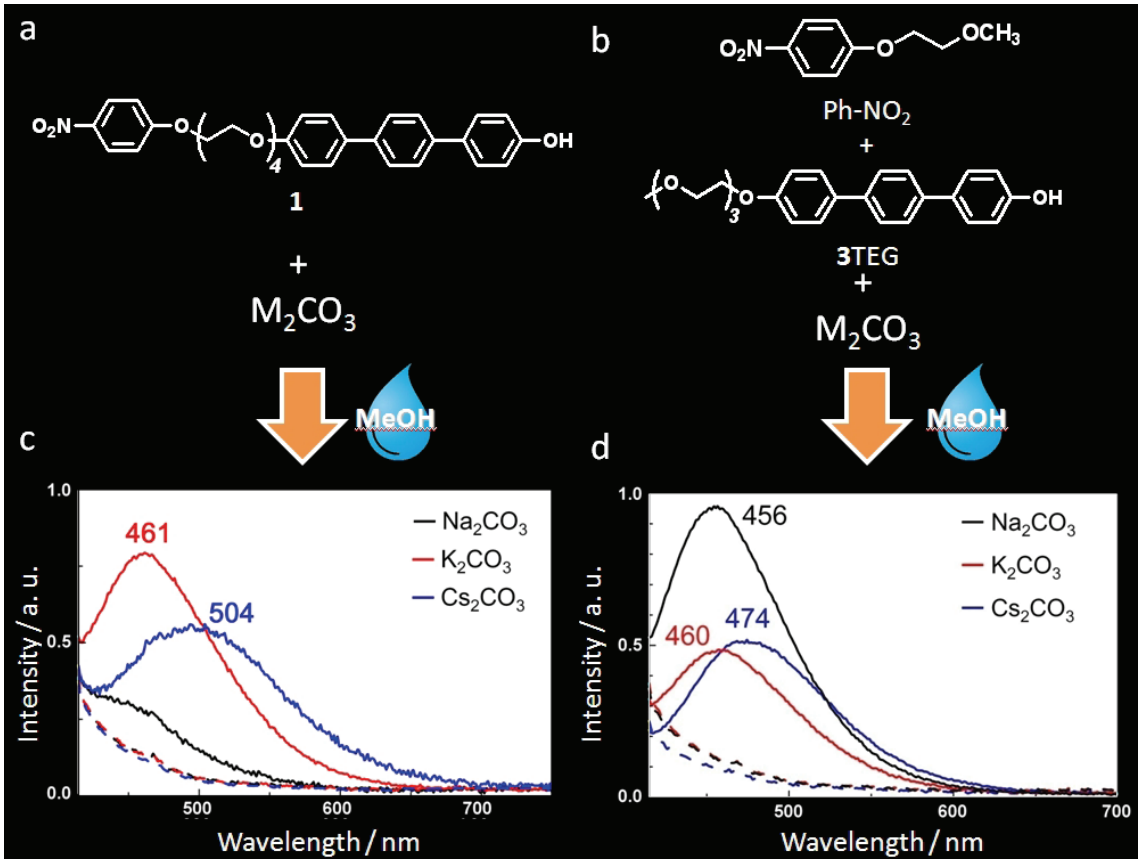

Figure 3. Interaction of **1** (a) or its component chromophore moieties (3TEG) (b) with alkali metal cations. (c) Fluorescence spectra of the mixtures revealing the different spectrum in the presence of Cs^+. (d) In the simple mixture of component chromophores the shift in fluorescence maximum is rather small and is not sufficient for sensing activity. Numbers above the spectra in panels (c) and (d) indicate the wavelength of the fluorescence maximum.

Recent research suggests that sulfate aerosols were the transport medium of radiocesium from the Fukushima nuclear accident.[8] Accordingly, a mixture of **1** and cesium sulfate exhibited green fluorescence under basic conditions after spraying with methanol (Figure 4).

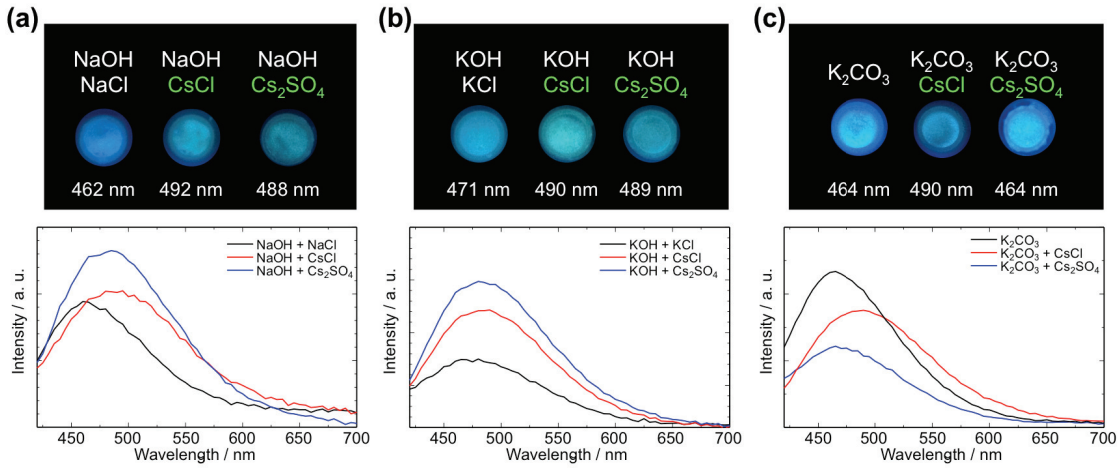

Figure 4. Photographs (a)–(c) and spectra of fluorescence change (d)–(f) of a mixture of **1** and alkali metal salt under UV irradiation (365 nm) after addition of a drop of methanol. Fluorescence change of a powder mixture of **1** and Cs^+ under basic conditions after spraying with methanol. Numbers in panels (a)–(c) indicate the wavelength of the fluorescence maximum.

In ascertaining whether the fluorimetric response or selectivity of **1** could be varied, I prepared compound **2** where the 4-NPE group of **1** had been replaced by a fluorescent naphthalene-1,8-dicarboxylic imide unit. Compound **2** unexpectedly behaves as a selective sensor for Rb^+ yielding a similar green fluorescence to that obtained for **1** and Cs^+ under basic conditions (Figure 5).

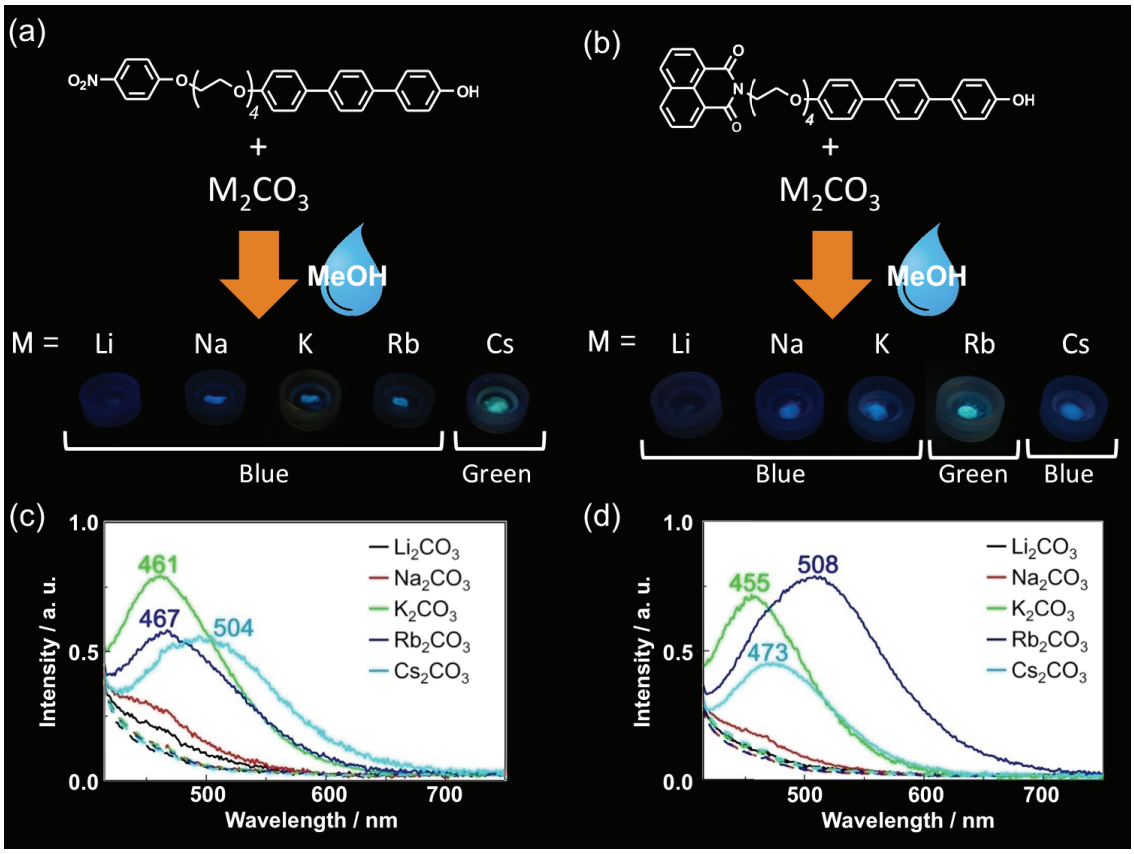

Figure 5. Photographs and spectra illustrating the differences in fluorescence emission from (a) **1** and (b) **2** in the presence of carbonate salts of alkali metal cations after spraying with methanol.

Detection of cesium carbonate particles using Cesium Green is based on fluorescence, thus its resolution can be greater than that of radiation detectors. To illustrate the potential of Cesium Green for micrometer-scale imaging, cesium carbonate and potassium carbonate particles were mixed prior to imaging by fluorescence microscopy. Green and blue fluorescence emitted by cesium- and potassium-containing particles, respectively, was observed (as shown in Figure 6).

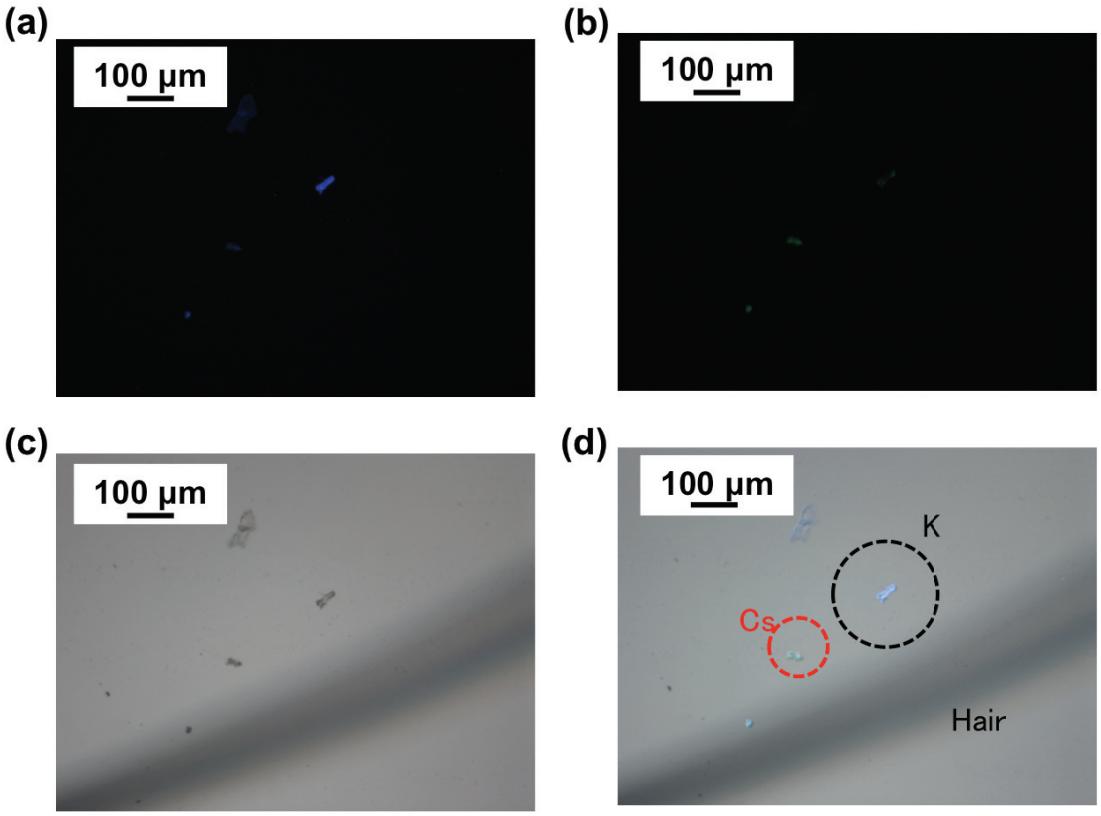

Figure 6. Imaging of cesium carbonate and potassium carbonate using **1**. (a) Blue fluorescence (Ex. 360 nm, Em. 425 nm), (b) green fluorescence (Ex. 480 nm, Em. 527nm), (c) Optical microscope image (transmission mode), (d) overlaid image. Dimensions of the particles can be estimated by reference to the human hair visible in the image (average diameter of human hair: ~100 µm).

3-2-2 Intracellar imaging of cesium distribution in a plant using the novel fluorescence probe

I considered that micrometer-scale imaging of cesium particles could be extended to cellular level imaging. Cesium uptake by plants occurs via the potassium transport system and resulting intracellular cesium distributions in plants are of interest although an imaging method has not been established to date. Determination of intracellular localization of cesium in plants is particularly important in the scope of phytoremediation or for detection of plants contaminated with cesium. Thus, I applied **1** to plant cell imaging using Arabidopsis cotyledon. Here, cesium imaging was performed using plants treated with high concentrations of cesium ions.[27, 28]

Arabidopsis seeds were germinated and grown for 9 days on medium containing 0.5 mM cesium carbonate. Elemental analyses revealed Cs^+ content in the resulting plants of 67 ± 11 nmol Cs/mg dry-weight. (Figure 7) Subsequently, the resulting seedlings were freeze-dried and soaked in 0.02wt% methanolic **1** solution prior to imaging by fluorescence microscopy.

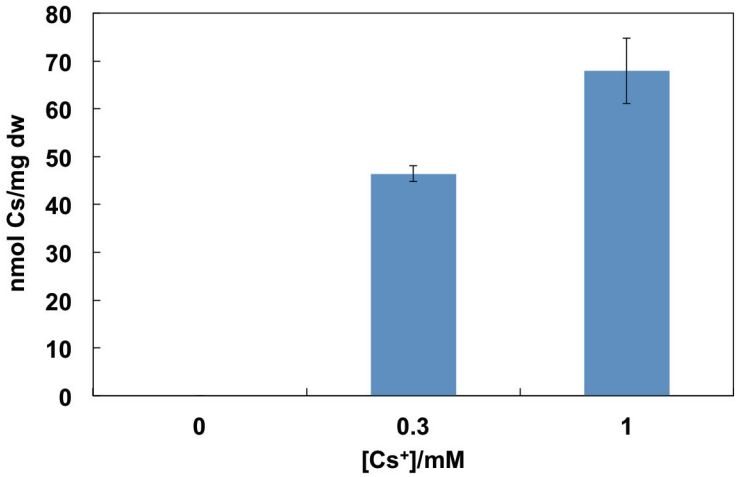

Figure 7. Cesium concentrations in *Arabidopsis* according to atomic absorption spectroscopy. Arabidopsis seeds were germinated and grown for 9 days on medium containing 0, 0.15 and 0.5 mM Cs_2CO_3.

Upon a comparison between the fluorescence images of cesium-treated and non-treated plants (Figure 8), bright fluorescent spots are visible in the cotyledons of the

cesium-treated plants, but not of the untreated plants. It is likely that these fluorescent spots are vacuoles, which are known to play a role in detoxification of potentially toxic substances (such as sodium under salt stress[29]) by sequestration. It is possible that plants sequestrate cesium in vacuoles to avoid its negative effects in the cytoplasm. From this result, it is apparent that **1** is suitable for detection of cesium in plants at the organelle level. This might contribute to a better understanding of the mechanisms by which plants accumulate cesium, indicating its potential in phytoremediation applications.

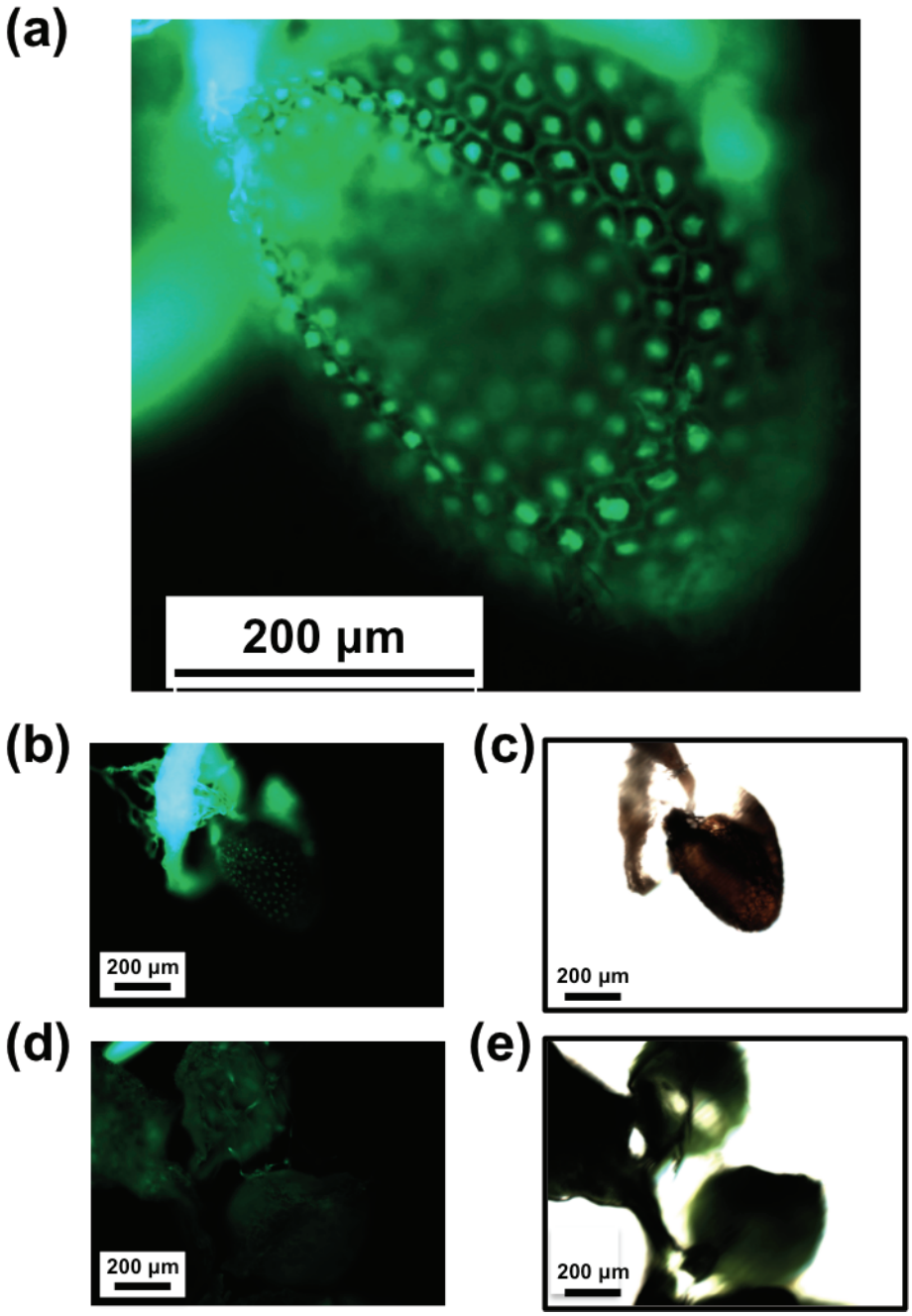

Figure 8. Cesium imaging of the cotyledon of *Arabidopsis* treated with a methanolic solution of **1** (0.02 wt%). (a and b) Fluorescence image (Ex 480 nm, Em 527 nm) of cotyledon of Arabidopsis treated with 0.5 mM Cs_2CO_3. (c) Optical micrograph in the presence of 0.5 mM Cs_2CO_3, (d) Fluorescence image of the plant grown in the absence of Cs_2CO_3, (e) Optical micrograph image in the absence of Cs.

3-2-3 Mechanism of the selective fluorescence color variation of the newly developed probe in the presence of cesium

Fluorescence lifetimes for **1** and **1** with K^+ or Cs^+ in methanol are summarized in Table 1. Lifetimes of intermolecular fluorescence (i.e. that involving two chromophores linked in the same molecule), such as that occurring due to FRET or exciplex mechanisms, are an order of magnitude longer than those of intramolecular fluorescence (i.e. that involving an isolated chromophore). For instance, the fluorescence lifetime of the naphthalimide monomer is about 1 ns. If a naphthalimide dimer forms an excimer then the fluorescence lifetime is longer (about 20 ns). The difference in fluorescence lifetime between [**1** + K_2CO_3] and [**1** + Cs_2CO_3] is small. Fluorescence lifetimes for **1** in the presence of alkali metal cations are an order of magnitude shorter than those expected for FRET and exciplex fluorescence emission mechanisms and suggest an intra-moiety mechanism involving the deprotonated terphenol group.

Table 1. Fluorescence lifetime of the mixtures of phenols and alkali metal carbonate after addition of methanol.

Compound	Excitation [nm]	Emission [nm]	Fluorescence lifetime [ns]
3TEG	279	380	1.38 (56%), 3,72 (44%)
3TEG + K_2CO_3	375	460	1.27 (72%), 3,24 (28%)
3TEG + Cs_2CO_3	375	460	0.19 (10 %), 1.58 (90 %)
1	279	380	0.66 (43%), 1.18 (57%)
1+ K_2CO_3	375	460	0.33 (10%), 2.08 (90%)
1+ Cs_2CO_3	375	460	0.20 (14%), 2.97 (86%)
1+ Cs_2CO_3	375	505	0.14 (16%), 2.73 (84%)

To explain this disparity in the responses of the two sensor molecules (**1** and **2**), I considered the respective geometries of **1** and **2** during interaction with the analyte cations by applying density functional theory (DFT)[30] geometry optimization to the resulting complexes. The results (Figure 9) show that the forms of the complexes of the cations with each ligand are very similar, with the electropositive metal cation being coordinated by oxygen atoms of the tetraethylene glycol chain, similar to the situation in the crown ether complexes. It is important to note that a weak hydrogen bond

between the 4-nitro group of the NPE moiety and one methine of the terphenol is predicted and in fact could be detected in infrared spectra of **1** in the presence of alkali metal cations (see Figure 10). This hydrogen bond apparently stabilizes a quasi-macrocyclic conformation of **1** while no similar interaction occurs in **2**. This also explains why for the previously mentioned physical mixture involving disconnected components of **1** there is no differentiation between cations, as macrocyclization of the host's component moieties is not possible. On the other hand, in **2** there are apparent CH-π interactions between the naphthalenedicarboxylic imide unit and the π-electronic system of its terphenyl. Now, considering the departure from ideal geometry in each case, measured by summing the angular departures from ideal tetrahedral geometry of the methylene groups of the tetraethylene glycol chain, we find that for **2**, Rb^+ is most easily accommodated, while for **1** Cs^+ is favored. Perhaps serendipitously, the optimal binding geometry for **1**.Cs^+ and **2**.Rb^+ also leads to the respective cations being brought in closer proximity to the alkoxyphenyl end of the HTP group.

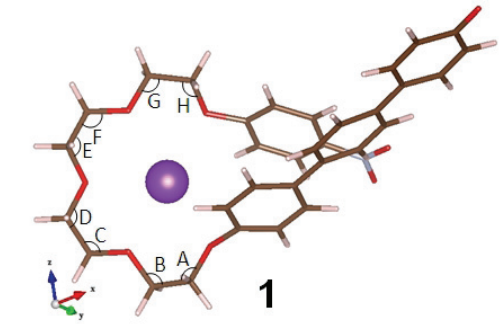

Angle	K	Δ_K	Rb	Δ_{Rb}	Cs	Δ_{Cs}
B	107.5	2	108.0	1.5	108.5	1
C	107.6	1.9	108.3	1.2	109.2	0.3
D	108.7	0.8	109.3	0.2	109.5	0
E	108.9	0.6	109.6	0.1	109.5	0
F	108.8	0.7	109.3	0.2	109.5	0
G	108.4	1.1	108.2	1.3	109.0	0.5
		1.18		0.75		0.30

Δ = |Angle - 109.5|

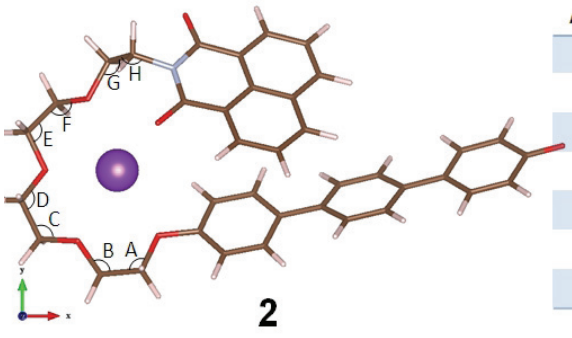

Angle	K	Δ_K	Rb	Δ_{Rb}	Cs	Δ_{Cs}
B	109.4	0.1	109.4	0.1	109.2	0.3
C	109.1	0.4	109.5	0	109.9	0.4
D	108	1.5	108.5	1	109.0	0.5
E	108.3	1.2	108.9	0.6	109.3	0.2
F	108.9	0.6	109.4	0.1	110.0	0.5
G	109.6	0.1	110.0	0.5	110.4	0.9
		0.65		0.38		0.47

Δ = |Angle - 109.5|

Figure 9. Selected angles of the computed structures of the complexes of **1** with K^+, Rb^+ or Cs^+ and **2** with K^+, Rb^+ or Cs^+. Dihedral angles subtended at the indicated bonds are listed in the table on the right.

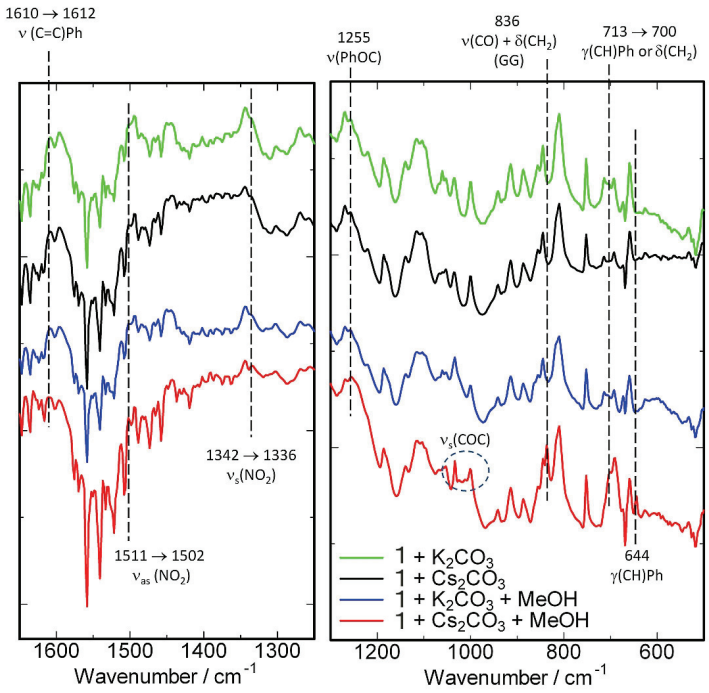

Figure 10. FT-Infrared spectra (KBr pellets) of **1** mixed with potassium carbonate (green line) or cesium carbonate (black line) and similar samples in the presence of methanol (K_2CO_3/methanol: blue line; Cs_2CO_3/methanol: red line). Changes in the frequencies especially of the nitro group symmetric and asymmetric stretching are consistent with the formation of an intramolecular hydrogen bond in **1** as predicted by DFT data.

To explain the selectivity of the response to Cs^+ for **1**, I consider that the deprotonated terphenol unit is formally a donor–acceptor (D–A) type moiety (Figure 11, also as mentioned Chapter 2-2). Deprotonation of the HTP unit leads to an electronic donor state for the phenol part of the molecule while the opposing alkyloxyphenyl unit is relatively electron deficient. The fluorescence of the mixtures between **1** and alkali metal carbonates are bathochromically shifted by *intramolecular charge transfer* following addition of methanol by the mechanism proposed by Valeur.[31, 32] Fluorescence lifetime is slightly longer for **1** + Cs_2CO_3 than **1** + K_2CO_3 suggesting that excitons of **1** + Cs_2CO_3 are more stable. When Cs^+ interacts with the acceptor group of deprotonated **1** the excited state is stabilized more by Cs^+ than the ground state, and this leads to a bathochromic shift of the fluorescence maximum (Figure 12). For **2**, Rb^+ also approaches more closely than other alkali metal cations the electron-deficient part of the deprotonated phenol.

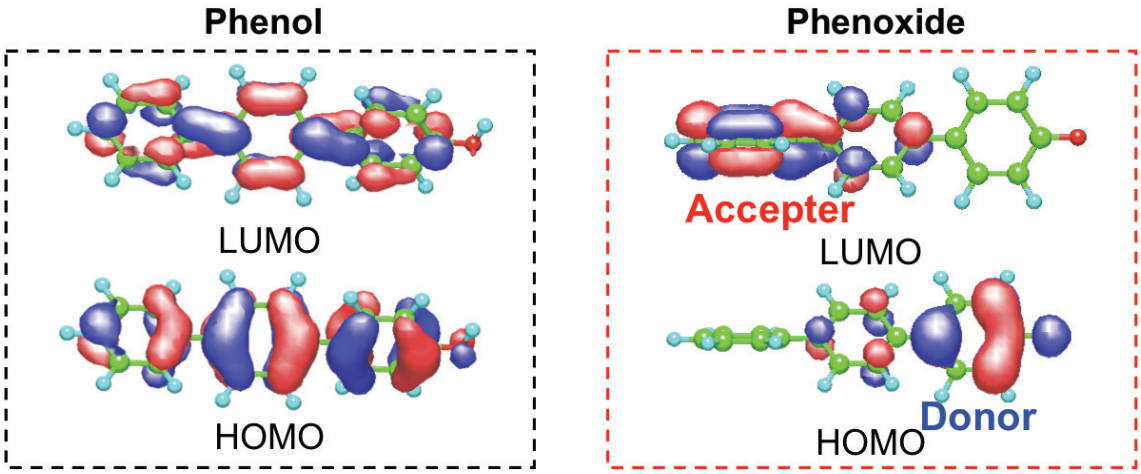

Figure 11. Origin of the donor-acceptor (D-A) character of terphenol. In the phenol both the highest occupied molecular orbital (HOMO) and lowest unoccupied molecular orbital (LUMO) are situated over the extent of the molecule. Upon deprotonation, HOMO is situated at the electron-rich phenoxide group while the LUMO is situated at the electron-deficient phenyl group remote from the phenol. (MOPAC2000 program Optimized Structure: PM5 method)

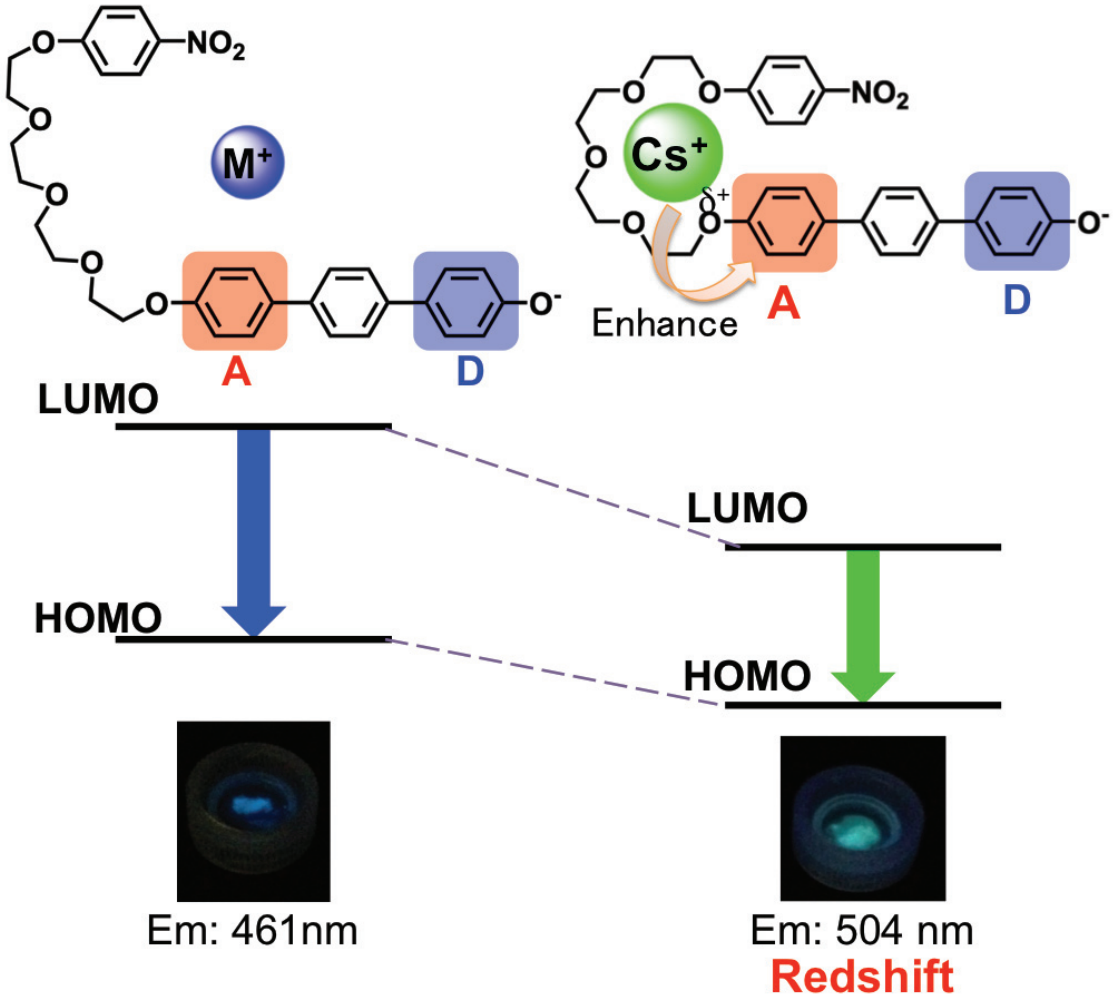

Figure 12. Schematic of the computed structures of the complexes of **1** with K^+ or Cs^+. Em stands for emission wavelength.

Although my initial molecular design was based on an expectation that FRET or exciplex phenomena might be observed in **1** due to intermolecular interaction, introduction of the 4-nitrophenyl ether group introduced a serendipitous point for intramolecular macrocyclization through hydrogen bonding (between the 4-nitro group and one HTP methane[33]) with no optical effects due to this group, except for changes in the fluorescence upon binding different cations due to *intramolecular* effects. Moreover, I believe that it would anyway be extremely difficult to detect any difference between complexes of **1** with the alkali metal cations if FRET or exciplex mechanisms operated

in this case, due to the substantial similarities in structure between the complexes, especially with regard to the relative positioning of the donor and acceptor chromophores. In fact, FRET or exciplex emission would likely obstruct cation differentiation in this case due to the subtlety of the effect of the proximity of the Cs^+ to the HTP group.

3-2-4 Detection of cesium ion in aqueous media using an optode membrane

The cesium binding site of **1** is considered to be the ethylene glycol chain. It is also known that deprotonation of phenol enhances the sensitivity of its fluorescence response. Although **1** responds to solid cesium-containing particles, a quantitative estimation of selectivity is not possible in the form of a solid. Thus, a lipophilic analogue of **1**, **1-C12** was synthesized and applied as an ionophore in the optode method (Figure 13).[34–36] In optode systems, the ionophore and membrane extraction affect the protonation of a pH-responsive dye inducing a color change of the dye. By using the optode method, aqueous-phase cesium detection and estimation of the selectivity by organic phase extraction become possible. Also, there exist other optode methods for determination of Cs^+, which may be useful for comparative purpose.[37, 38] In this work, the optode membrane was prepared from Cesium **1-C12**, the pH-response dye KD-M13,[39] the cation exchanger NaTFPB and the plasticizer dioctyl sebacate (DOS) with PVC as a matrix.

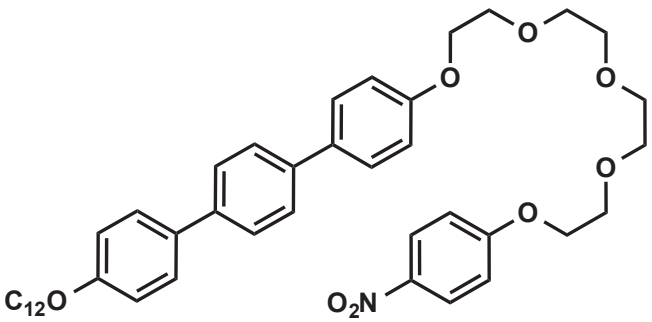

Figure 13. 1 modified with *n*-dodecyl ether (**1-C12**).

Responses of the **1-C12**-based optode membrane are shown in Figure 14 and the poor selectivities of the optode for alkali metal cations were revealed. Using **1-C12**, aqueous-phase Cs^+ detection could be established although the selectivity was

moderate.

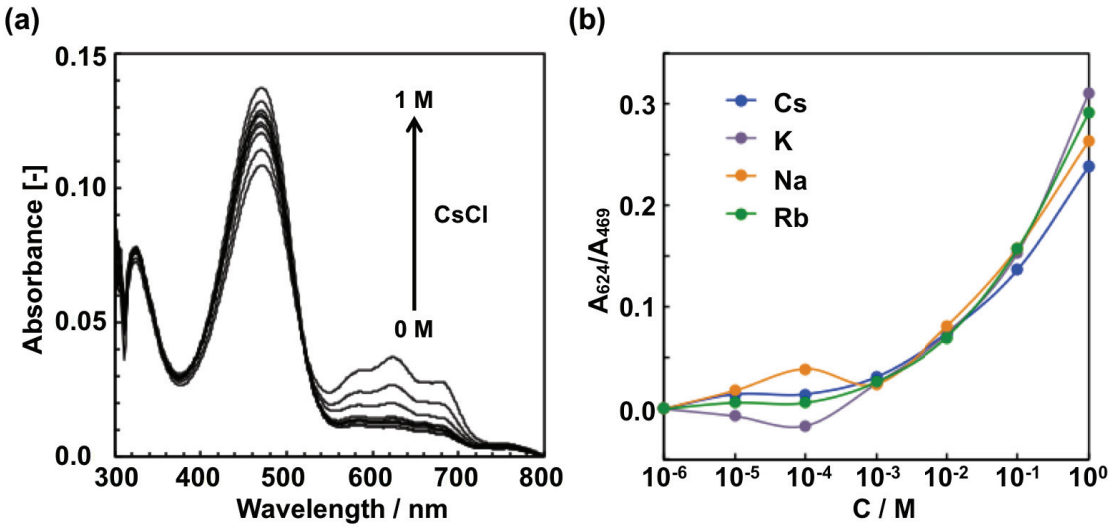

Figure 14. Cesium Green-C12-based optode. (A) Responses to cesium ([CsCl] = 1×10^{-6}, 5×10^{-6}, 1×10^{-5}, 5×10^{-5}, 1×10^{-4}, 1×10^{-3}, 1×10^{-2}, 1×10^{-1}, 1 M) (B) Selectivity for CsCl, NaCl, KCl and RbCl.

From a comparison of the organic-phase extraction (membrane) selectivity with the solid-phase cesium selectivity, it seems that the sensitivity of **1** is derived not only from binding of cesium cations at the ethylene glycol unit but also from the optical selectivity for cesium cations in the solid state.

In order to detect Cs^+ in aqueous phase with better selectivity and sensitivity, reported host molecules for Cs^+ were incorporated to optode membranes and characterized. As shown in Figure 15, **Biscrown**[40] and **Calix**[41] were selected because of their strong affinity to Cs^+. Both **Biscrown** and **Calix**-based optode membranes showed responses to Cs^+ (Figure 15c and 15d). Next, these responses were precisely characterized by analyzing these response curves, obtained from these spectra. The optode incorporating **Biscrown** showed response from ca. 1.0 mM of Cs^+ (Figure 15e). By comparing the response curve to ones of other cations, it is estimated that this optode system has selectivity against Na^+ with 5-fold and K^+ with 10-fold. On the other hand, the **Calix**-based optode showed better selectivity and sensitivity, compared to **1-C12** and **Biscrown**. Dissociation degree α of the incorporated pH-responsive dye were obtained from the UV/vis spectra at each concentration of CsCl. α is expressed by

A/A_0 at 620 nm (A_0 is an absorbance at cation free). Figure 15f displays a response curve of α vs. cations concentration. From this curve, the membrane with **Calix** showed response to Cs^+ from 10^{-5} M, although it showed no responses to cations existing in environments, such as Na^+, Mg^{2+} and Ca^{2+}. A coupling constant between the **Calix-**based optode membrane and Cs^+, K_{exch} was obtained by fitting theoretical curves to experimental ones (5.72×10^{-5}; Table 2). Although the membrane has responsivity to K^+ as an interfering cation, the selectivity against K^+ is good (ca. 100-fold) (Table 2). Moreover, a significant color change in the optode membrane was observed from yellow to green. Thus, the detection of Cs^+ with the naked eye is possible (Figure 16).

Finally, I tried Cs^+ detection in sea and tap water for considerations of practical systems. As a result, the optode membrane incorporating **Calix** showed responses both in UV/vis spectra and color hues (Figure 16). Even in those water systems bearing some interfering cations, the membrane detected Cs^+ from around 10^{-4}–10^{-5} M (Figure 17). From these results, Cs^+ in aqueous solutions were successfully detected with good selectivity.

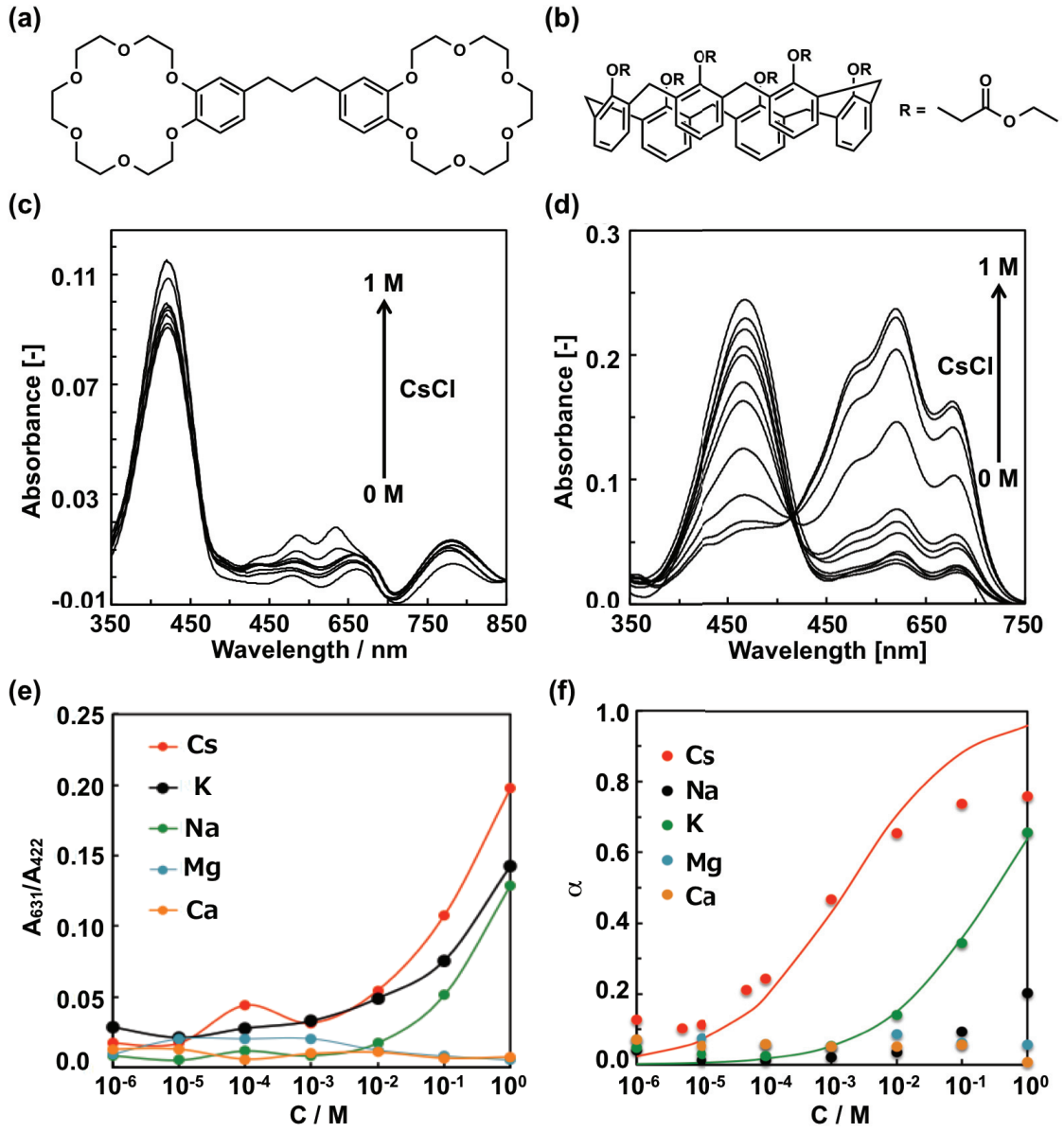

Figure 15. Chemical structures of host molecules (a, **Biscrown** and b, **Calix**). Variations in UV/vis spectra of optode membranes incorporating **Biscrown** (c) or **Calix** (d) to cesium ([CsCl] = 1×10^{-6}, 5×10^{-6}, 1×10^{-5}, 5×10^{-5}, 1×10^{-4}, 1×10^{-3}, 1×10^{-2}, 1×10^{-1}, 1 M). pH values of the Bis-tris buffer solutions were 9.0 (**Biscrown**) and 7.0 (Calix), respectively. Response curves of optode membranes incorporating **Biscrown** (e) or **Calix** (f) to cesium. Solid lines on (b) are theoretical response curves, fitted to experimental ones.

Table 2. Coupling constants (K_{exch}) and selectivity coefficients (log K_{ij}^{opt}) for the optode membrane incorporating **calix**.

	K_{exch} [-]	log K_{ij}^{opt}
Cs^+	5.72E-05	-
Na^+	-	-
K^+	3.13E-07	-2.2
Rb^+	8.88E-06	-0.8
Mg^{2+}	-	-
Ca^{2+}	-	-

$i = Cs^+$

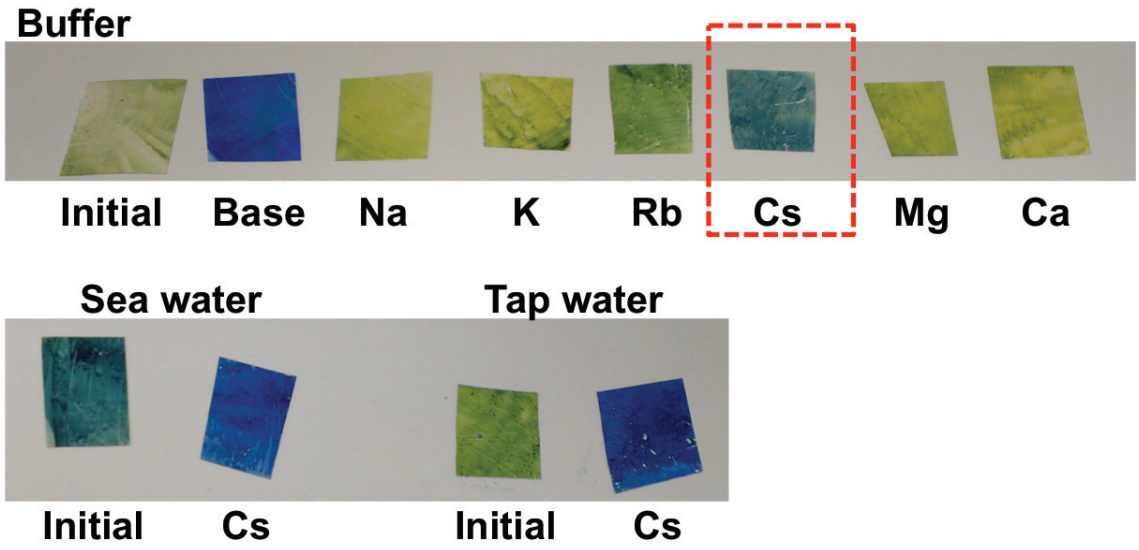

Figure 16. Color variations in optode membrane with **Calix** in Bis-tris buffer solution (pH 7.0), in seawater and in tap water incorporating 1.0 mM MCl.

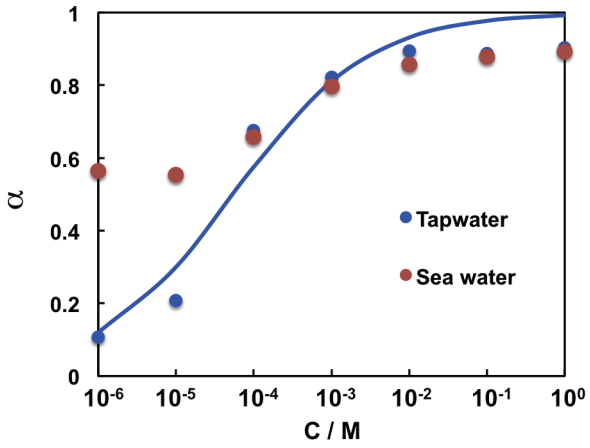

Figure 17. Response curves of optode membranes incorporating **Biscrown** (a) or **Calix** (b) to cesium in sea or tap water. A solid line on is a theoretical response curve for curves of tapwater, fitted to experimental ones.

3-3 Conclusions

In this chapter, I have demonstrated the detection of cesium in solid and aqueous state, and also in the body of plant. The simple optical probe **1** has a higher spatial resolution for Cs-137 than existing radioscopes and gamma ray cameras. Since only contaminated particles are detected by eye and can be easily removed, the volume of radioactively contaminated material for extraction is greatly reduced. Moreover, application of **1** for plant cell imaging suggested that cesium absorbed from growth media might be sequestrated in the vacuole in *Arabidopsis*. This result highlights the capability of the probe for visualization of cesium accumulated in plants at the organelle level. The location of cesium in solid samples such as soil, foodstuffs and plants can be visualized by using this probe, allowing one to study its diffusion processes and accumulation behavior in those media. In addition, an optode membrane using **Calix** could detect Cs^+ in aqueous media (buffer, sea and tap water) showed moderate and high selectivity for Cs^+. The availability of this and other similarly easily implemented tests for environmental contaminants is likely to increase the volume of data regarding rates of contamination around chemical and radiological hazards. In addition, the cesium imaging in plants would lead to phytoremediation, which is a method to extract radioactive materials from contaminated environments.

3-4 Experimental part

Materials.

Solvents and materials were purchased from Tokyo Chemical Industry Co Ltd (Tokyo, Japan) and Wako Pure Chemical Co (Osaka, Japan), and were used without further purification. ^{1}H and ^{13}C nuclear magnetic resonance (NMR) spectra were measured at 298 K from $CDCl_3$ or d_6-dimethyl sulfoxide (DMSO) solutions of the samples using a JEOL model AL300BX (300 MHz) spectrometer with tetramethylsilane (Me_4Si) as an internal standard. Chemical shifts (*d*) and coupling constants (*J*) are given in parts per million (ppm) and hertz (Hz), respectively. Matrix-assisted laser desorption/ionization time-of-flight mass spectrometry (MALDI-TOF-MS) measurements were carried out using a Shimadzu-Kratos AXIMA+ mass spectrometer with dithranol as a matrix. High-resolution mass spectra (HRMS, ESI-positive) were acquired with JMS-MS700 (JEOL), and elemental analysis was performed with a PE 2400II (PerkinElmer) system.

Measurements.

Electronic absorption spectra were measured from tetrahydrofuran solutions of the samples using a Shimadzu model UV-3600 UV/Vis/NIR spectrophotometer. Fourier transform infrared (FTIR) spectra were measured from KBr pellets using a Nicolet model 760X spectrometer. Fluorescence spectra were measured from solid samples using an Otsuka Electronics, model MCPD-7000 spectrometer. Fluorescence lifetimes were measured using a Horiba model FluoroCube UltraFast-3000U setup. Leica Microsystems BM 2500 was used for fluorescence imaging, and ×10 objective lens was used.

Synthesis and structural characterization.

Synthetic routes of **1** and **2** are shown in scheme 1. Simple substituted derivatives are designated **3TEG** (TEG = 2-{2-[2-(methoxyethoxy)ethoxy]ethoxy}) (Scheme 2). Preparations of **Biscrown**[40] and **Calix**[41] have been reported previously.

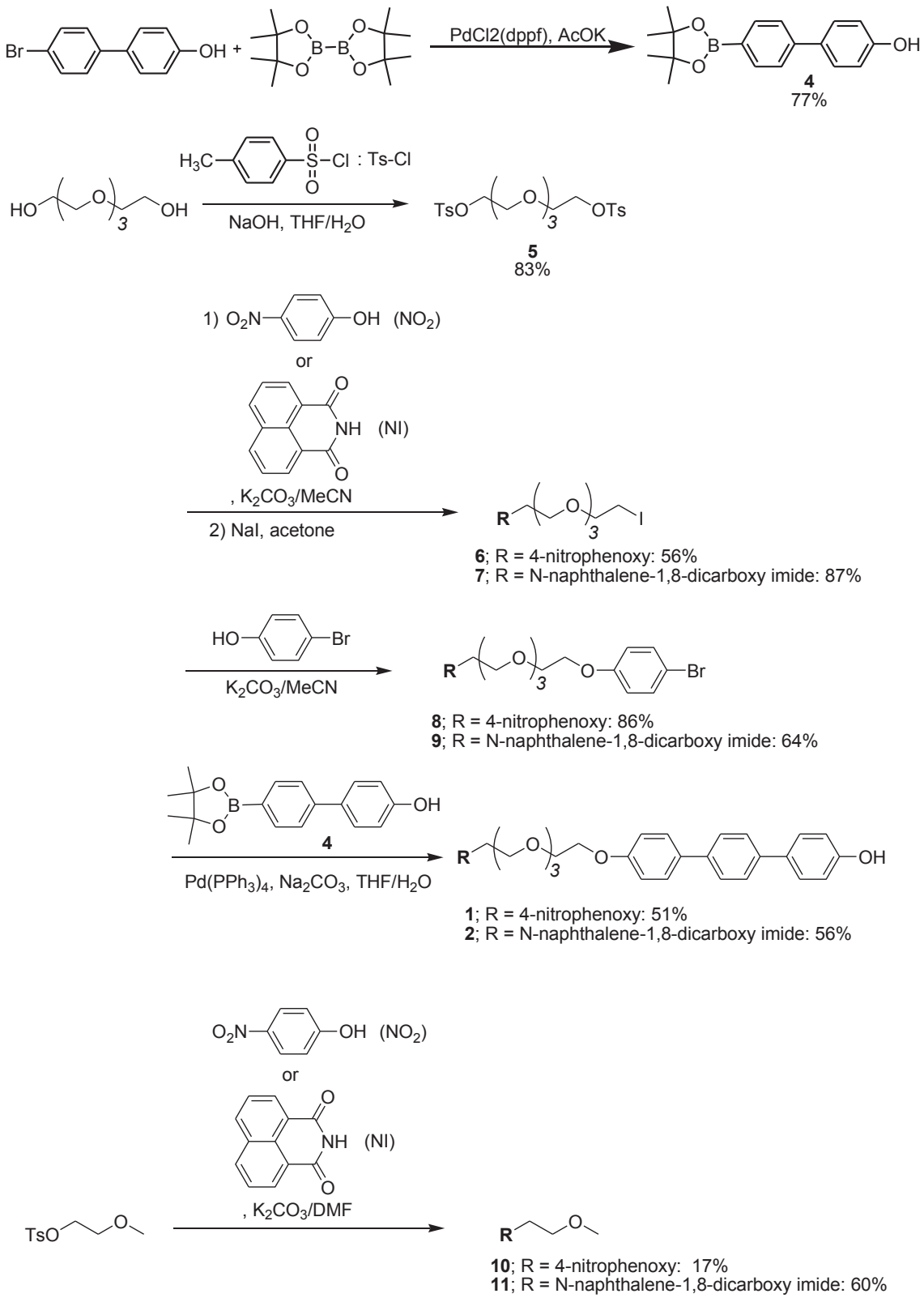

Scheme 1. Synthesis of host molecule **1**, **2** and control molecules.

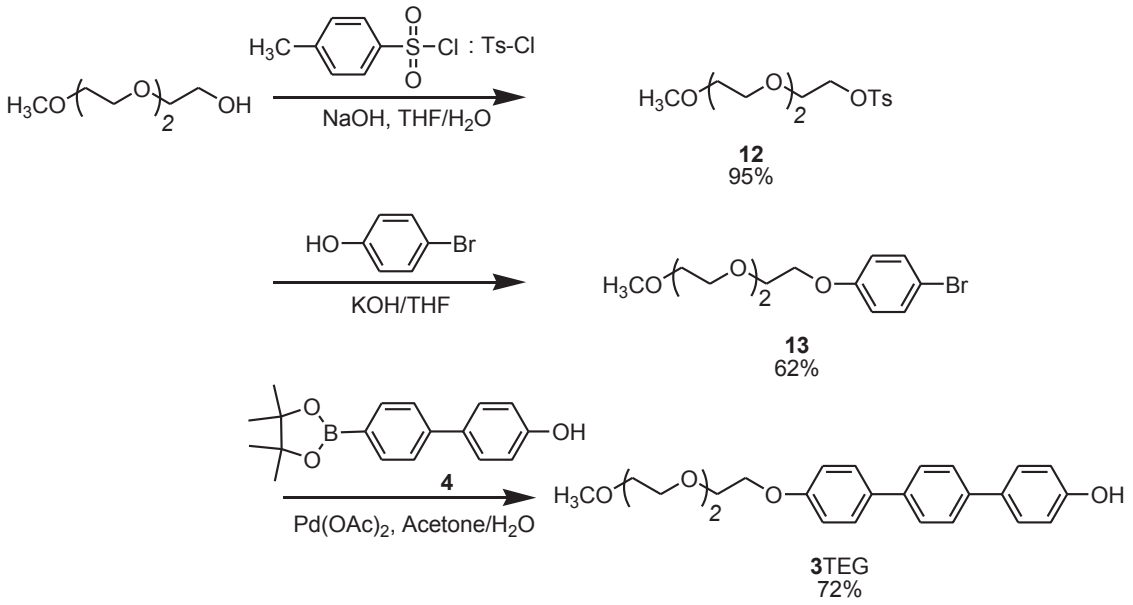

Scheme 2 Synthesis of **P3TEG**.

4-Hydroxy-4' -(4,4' ,5,5' -tetramethyl-1,3,2-dioxaborolan -2-yl) biphenyl (4).

4'-Bromo-[1,1'-biphenyl]-4-ol (0.498 g, 2 mmol), potassium acetate (KOAc, 0.588 g, 6 mmol), $PdCl_2$(dppf) (dppf = 1,10 -bis(diphenylphosphino)ferrocene; 0.043 g, 0.06 mmol), and bis(2,2,3,3-tetramethyl-2,3- butanedionato)diboron (0.761g, 3.0mmol) were dissolved in anhydrous DMSO (12 ml). The mixture was heated at 80 C for 4 h with stirring under N_2. The mixture was cooled to room temperature and the solid filtered off and washed with dichloromethane. After evaporation of the solvents under reduced pressure, the residue was purified by silica gel column chromatography (AcOEt/hexane=1/2, where AcOEt stands for ethyl acetate), to give 0.351g of **4** as a white powder in 59% yield. ^{1}H-NMR (300 MHz, $CDCl_3$, 25 ºC): d = 1.36 (s, 12H), 5.16 (s, 1H), 6.91 (d, 2H, J = 9.0), 7.41–7.63 (m, 4H), 7.86 (d, 2H, J = 9.0) ppm. MALDI-TOF (dithranol): m/z = 296.1 $[M]^+$.

Tetraethylene glycol bis(4-toluenesulfonate) (5).[42]

Sodium hydroxide (1.06 g, 26 mmol) dissolved in water (10 ml) and tetraethylene glycol (1.71 g, 8.8 mmol) in tetrahydrofuran (THF, 10 ml) were placed in a flask and the mixture was cooled on an ice bath with magnetic stirring. To the mixture was added dropwise *p*-toluenesulfonyl chloride (3.50 g, 17 mmol) in THF (10 ml) over 1 h with

continuous stirring and cooling of the mixture below 5 C. The solution was stirred at 0–5 C for an additional 4 h, and then poured into ice water (50 ml). The mixture was extracted twice with dichloromethane. The combined organic extracts were washed with saturated aqueous sodium chloride solution, and then dried over anhydrous Na_2SO_4. After evaporation of the solvent, the resulting crude product was purified by chromatography on silica gel with ethyl acetate, giving the product as colorless oil in an 83% yield. ^{1}H-NMR (300 MHz, $CDCl_3$, 25 ºC): δ = 2.44 (s, 6H), 3.55–3.58 (m, 8H), 3.67 (t, 4H, J = 4.6), 4.15 (t, 4H, J = 4.6), 7.33 (d, 4H, J = 8.1), 7.79 (d, 4H, J = 8.4) ppm. MALDI-TOF (dithranol): m/z = 525.15 $[M+Na]^+$, 541.16 $[M+K]^+$.

11-Iodo-3,6,9-trioxaundecyl-(4-nitrophenyl)ether (6).

Potassium carbonate (0.691 g, 5.0 mmol) and potassium iodide (0.002 g, 0.1 mmol) were added to a CH_3CN (20 ml) solution of a mixture of 4-nitrophenol (0.347 g, 2.5 mmol) and **5** (5.02 g, 10 mmol), and the resulting suspension was refluxed for 13 h under N_2. The reaction mixture was allowed to cool to room temperature and the solvents evaporated under reduced pressure. The residue was dissolved in CH_2Cl_2, washed with water and dried over anhydrous Na_2SO_4. After evaporation of the solvent under reduced pressure, the residue was dissolved in acetone (50 ml), NaI (15.0 g, 100 mmol) was added, and the mixture was heated at reflux for 24 h. The reaction mixture was allowed to cool to room temperature and then the solvent was removed under reduced pressure. The residue was taken into CH_2Cl_2 and the solution was washed with water, dried over anhydrous Na_2SO_4, and then the solvent was removed under reduced pressure. The crude product was subjected to column chromatography (SiO_2, AcOEt/hexane: 1/1 v/v) which yielded the product as a colorless oil (0.60 g) in a 56% yield. ^{1}H-NMR (300 MHz, $CDCl_3$, 25 ºC): d = 3.25 (t, 2H, J = 7.0), 3.77–3.66 (m, 10H), 3.91–3.88 (m, 2H), 4.23 (t, 2H, J =3.0), 6.98 (d, 2H, J =9.2), 8.19 (d, 2H, J =9.2) ppm. ^{13}C-NMR (75 MHz, $CDCl_3$, 25 ºC): d = 2.92, 68.14, 69.34, 70.15, 70.57, 70.65, 70.87, 71.88, 114.52, 125.83, 141.50, 163.78 ppm. MALDI-TOF (dithranol): m/z = 448.16 $[M+Na]^+$, 464.11 $[M+K]^+$. HRMS (ESI) m/z calculated for $C_{14}H_{20}INNaO_6$ $[M+Na]^+$: 448.0225, found 448.0233.

N-(11-Iodo-3,6,9-trioxaundecyl)naphthalene-1,8-di- carboxylic acid imide (7).

^{1}H-NMR (300 MHz, $CDCl_3$, 25 ºC): d = 3.22–3.17 (m, 2H), 3.73–3.53 (m, 16H), 3.85–

3.81 (m, 2H), 4.47–4.42 (m, 2H), 7.75 (t, 2H, *J* = 7.7), 8.22 (d, 2H, *J* = 8.3), 8.60 (d, 2H, *J* = 7.3) ppm. ^{13}C-NMR (75 MHz, $CDCl_3$, 25 ºC): *d* = 2.92, 39.04, 67.88, 70.06, 70.11, 70.48, 70.58, 71.83, 122.50, 126.85, 128.08, 131.18, 131.46, 133.90, 164.11 ppm. MALDI-TOF (dithranol): m/z = 484.36 $[M+H]^+$, 506.37 $[M+Na]^+$, 522.26 $[M+K]^+$.

11-(4-Bromophenoxy)-3,6,9-trioxaundecyl-(4-nitrophe- nyl)ether (8).

K_2CO_3 (0.349 g, 2.5 mmol) was added to a solution of a mixture of 4-bromophenol (0.128 g, 1.3 mmol) and **6** (0.305 g, 0.63 mmol) in CH_3CN (10 ml), and the resulting suspension was refluxed for 15 h under N_2. The reaction mixture was allowed to cool to room temperature and solvent removed under reduced pressure. The residue was dissolved in ethyl acetate and the solution was washed with water, dried over anhydrous Na_2SO_4, and then solvent was removed under reduced pressure. The crude product was subjected to column chromatography (SiO_2, AcOEt/hexane 1/1 v/v) yielding the product as a white solid (0.213 g, 64%). ^{1}H-NMR (300 MHz, $CDCl_3$, 25 ºC): *d* = 3.74–3.65 (m, 8H), 3.89–3.82 (m, 4H), 4.13–4.07 (m, 2H), 4.20 (t, 2H, *J* = 1.9), 6.78 (d, 2H, *J* = 9.0), 6.96 (d, 2H, *J* = 9.3), 7.33 (d, 2H, *J* = 8.7), 8.18 (t, 2H, *J* = 4.6) ppm. ^{13}C-NMR (75 MHz, $CDCl_3$, 25 ºC): *d* = 67.62, 68.14, 69.35, 69.62, 70.62, 70.64, 70.81, 70.88, 113.00, 114.53, 116.37, 125.84, 132.19, 141.53, 157.83, 163.79 ppm. MALDI-TOF (dithranol): m/z = 492.02 $[M + Na]^+$. HRMS (ESI) m/z calculated for $C_{20}H_{24}BrNNaO_7$ $[M+Na]^+$: 492.0624, found 492.0634.

N-[11-(4-Bromophenoxy)-3,6,9-trioxaundecyl]naph-thalene-1,8-dicarboxylic acid imide (9).

^{1}H-NMR (300 MHz, CDCl3, 25 ºC): *d* = 3.63–3.61 (m, 6H), 3.71–3.86 (m, 2H), 3.84–3.76 (m, 4H), 4.15–4.02 (m, 2H,), 4.44 (t, 2H, *J* =6.0), 6.76 (d, 2H, *J* =4.6), 7.32 (d, 2H, *J* =7.5), 7.74 (t, 2H, *J* = 8.0), 8.20 (d, 2H, *J* = 7.3), 8.59 (d, 2H, *J* = 6.0) ppm. ^{13}C-NMR (75 MHz, $CDCl_3$, 25 ºC): *d* = 39.07, 67.56, 67.89, 69.52, 70.12, 70.59, 70.74, 112.89, 116.36, 122.56, 126.88, 128.14, 131.22, 131.52, 132.12, 133.94, 157.83, 164.18 ppm. MALDI-TOF (dithranol): m/z = 528.12 $[M+H]^+$. HRMS (ESI) m/z calculated for $C_{26}H_{26}BrNNaO_6$ $[M+Na]^+$: 550.0833, found 550.0841.

11-(4''-Hydroxy-1''-phenyl-1',4'-phenyl-1,4-phenoxy)-3,6,9-trioxaundecyl-(4-nitro phenyl)ether (1).

4 (0.250 g, 0.53 mmol) and **8** (0.250 g, 0.50 mmol) were dissolved in THF (16 ml). 2.0 M aqueous Na_2CO_3 (16 ml) was (added and the solution was purged with N_2 gas. Tetrakis(triphenylphosphine) palladium(0) (3 mg, 0.0031mmol) was added and the mixture was heated at 80 ºC for 24 h with vigorous stirring under N_2. After cooling to room temperature, solvents were removed under reduced pressure and the residue dissolved in ethyl acetate, followed by washing with water and drying of the organic phase over anhydrous Na_2SO_4. The solution was filtered and solvent removed under reduced pressure. The crude product was purified by column chromatography (silica gel) using THF/hexane = 9/1 as the eluent to yield 0.152 g (51%) as an orange solid. ^{1}H-NMR (300 MHz, d_6-DMSO, 25 ºC): d = 3.58–3.56 (m, 8H), 3.78–3.76 (m, 4H), 4.12–4.10 (m, 2H), 4.24–4.21 (m, 2H), 6.85 (d, 2H, J = 8.6), 7.01 (d, 2H, J = 8.8), 7.14 (d, 2H, J = 9.3), 7.52 (d, 2H, J = 8.6), 7.62–7.59 (m, 6H), 8.17 (d, 2H, J = 9.1), 9.55 (s, 1H) ppm. ^{13}C-NMR (75 MHz, d_6 -DMSO, 25 ºC): d = 67.38, 68.43, 68.80, 69.14, 70.03, 70.13, 115.09, 115.23, 115.95, 126.07, 126.53, 126.67, 127.69, 127.75, 130.59, 132.30, 137.85, 138.67, 140.98, 157.33, 158.24, 164.04 ppm. MALDI-TOF (dithranol): m/z = 559.02 $[M]^+$, 582.03 $[M+Na]^+$. Calculated for $C_{32}H_{33}NO_8$: %C, 68.68; %H, 5.94; %N, 2.50. Found: %C, 68.31; %H, 6.32; %N, 2.48.

N-[11-(4' '-Hydroxy-1' '-phenyl-1',4'-phenyl-1,4-phenoxy)-3,6,9-trioxaundecyl]naphthalene-1,8-dicarboxylic acid imide (2).

^{1}H-NMR (300 MHz, d_6-DMSO, 25 ºC): d = 3.56–3.47 (m, H), 3.68–3.64 (m, H), 4.09–4.06 (m, 4H), 4.25 (t, 2H, J = 6.5), 6.84 (d, 2H, J = 8.6), 6.99 (d, 2H, J = 8.8), 7.51 (d, 2H, J = 8.6), 7.61–7.57 (m, 6H), 7.86 (t, 2H, J = 4.0), 8.46 (d, 2H, J = 7.5), 8.5087 (d, 2H, J = 7.3), 9.55 (s, 1H) ppm. ^{13}C-NMR (75 MHz, d_6-DMSO, 25 ºC): d = 67.11, 67.32, 69.08, 69.85, 69.89, 70.00, 70.05, 115.08, 115.94, 122.21, 126.51, 126.66, 127.46, 127.60, 127.66, 127.74, 130.59, 131.01, 131.08, 131.52, 132.26, 134.60, 137.85, 138.65, 157.31, 158.21, 163.64 ppm. MALDI-TOF (dithranol): m/z = 617.57 $[M]^+$, 640.58 $[M + Na]^+$, 656.54 $[M + K]^+$. HRMS (ESI) m/z calculated for $C_{38}H_{35}NNaO_7$ $[M + Na]^+$: 640.2311, found 640.2292.

4-((12λ^3-dodeca-1,3,5,7,9,11-hexayn-1-yl)oxy)-4''-(2-(2-(2-(2-(4-nitrophenoxy)ethoxy)ethoxy)ethoxy)ethoxy)-1,1':4',1''-terphenyl (1-C12)

Potassium carbonate (65.4 mg, 5 eq.) and 1-bromododecane (30 mL, 106 mmol, 1.3 eq.) were added to a solution of Cesium Green **1** (53.2mg, 95.0 mmol, 1 eq.) in DMF (1 mL) and the mixture was stirred for 16 h at room temperature. The reaction mixture was then poured into water and extracted twice with EtOAc. The organic fractions were combined, washed twice with brine then dried over anhydrous Na_2SO_4. The solution was filtered then the solvents removed under reduced pressure. The residue was subjected to silica gel column chromatography (eluent: CH_2Cl_2 to acetone) to yield Cesium Green-C12 **2** as a white solid (48.2mg, 66.2 mmol, 69%). ^{1}H-NMR ($CDCl_3$, 300 MHz) 0.88 (t, 3H, 7 Hz), 1.24-1.50 (m, 18H), 1.81 (t, 2H, 7Hz), 3.68-3.78 (m, 8H), 3.86-3.92 (m, 4H), 4.00 (t, 2H, 7 Hz), 4.15-4.22 (m, 4H), 6.92-7.02 (m, 6H), 7.50-7.62 (m, 8H), 8.17 (d, 2H, 9Hz); ^{13}C-NMR (75 MHz, $CDCl_3$) 14.1, 22.7, 26.0, 29.3, 29.3, 29.4, 29.6, 29.6, 29.6, 29.6, 31.9, 61.7, 67.4, 68.0, 68.1, 69.3, 69.7, 70.6, 70.8, 70.8, 114.5, 114.7, 114.8, 114.8, 125.8, 126.9, 126.9, 127.9, 132.9, 133.3, 138.8, 139.1, 141.5, 158.2, 158.7, 163.8; LR-MALDI-MS: 729 [M+H$^+$]; HR-ESI-MS: calcd for $C_{44}H_{57}NO_8^+$ [M$^+$] 727.4084, found 727.4078.

2-Methoxyethyl-(4-nitrophenyl)ether (10).

K_2CO_3 (0.552 g, 4.0 mmol) was added to a solution mixture of 4-nitrophenol (0.278 g, 2.0 mmol) and 2-methoxyethoxy-4-toluenesulfonate (0.921 g, 4.0 mmol) in dimethylformamide (DMF, 10 ml), and the resulting suspension was refluxed for 12h. The reaction mixture was allowed to cool to room temperature and evaporated to dryness. CH_2Cl_2 solution of the residue was washed with water, dried over anhydrous Na_2SO_4, and evaporated to dryness. The residue and NaI (1.20 g, 8.0 mmol) were suspended in acetone (5 ml), and heated at reflux for 3 h. The reaction mixture was allowed to cool to room temperature and solvents removed under reduced pressure. The residue was dissolved in CH_2Cl_2, washed with water, dried over anhydrous Na_2SO_4, and then solvent was removed under reduced pressure. The product was obtained as colorless yellow needles (0.065 g) in a 17% yield. ^{1}H-NMR (300 MHz, $CDCl_3$, 25 ºC): *d* = 3.46 (s, 3H), 3.79 (t, 2H, *J* = 3.0), 4.22 (t, 2H, *J* =6.0), 7.00 (d, 2H, *J* =9.0), 8.20 (d, 2H, *J* =6.0) ppm. ^{13}C-NMR (75 MHz, $CDCl_3$, 25 ºC): *d* = 59.28, 68.04, 70.58, 114.53, 125.85, 141.62, 163.78 ppm.

N-(2-Methoxyethyl)naphthalene-1,8-dicarboxylic acid imide (11).

^{1}H-NMR (300 MHz, $CDCl_3$, 25 C): *d* = 3.39(s, 3H), 3.74(t, 2H, *J*=6.0), 4.46(t, 2H, *J*=6.0), 7.76 (t, 2H, *J* = 9.0), 8.22 (d, 2H, *J* = 9.0), 8.62 (d, 2H, *J* = 6.0) ppm. ^{13}C-NMR (75 MHz, $CDCl_3$, 25 C): *d* = 38.81, 58.38, 69.21, 122.15, 126.47, 127.89, 130.92, 131.14, 133.54, 163.88 ppm. MALDI-TOF (dithranol): *m*/*z* = 255.09 $[M]^+$. HRMS (ESI) *m*/*z* calculated for $C_{15}H_{13}NNaO_3$ $[M+Na]^+$: 278.0793, found 278.0790.

2-[2-(2-Methoxyethoxy)ethoxy]ethyl-4-methylben- zenesulfonate (12).[43]

Sodium hydroxide (0.9 g, 20 mmol) dissolved in water (20 ml) and triethylene glycol monomethyl ether (2.46 g, 15 mmol) in THF (20 ml) were placed in a flask and the mixture was cooled on an ice bath with magnetic stirring. To the mixture was added dropwise *p*-toluenesulfonyl chloride (2.88 g, 14 mmol) in THF (20 ml) over 1 h with continuous stirring and cooling of the mixture below 5 ºC. The solution was stirred at 0–5 ºC for an additional 4 h, and then poured into ice water (70 ml). The mixture was extracted twice with dichloromethane. The combined organic extracts were washed with saturated aqueous sodium chloride solution, and then dried over anhydrous magnesium sulfate. After evaporation of the solvent, the resulting crude product was purified by chromatography on silica gel with ethyl acetate to give **12** as colorless oil. ^{1}H-NMR (300 MHz, $CDCl_3$, 25 ºC): *d* = 2.44 (s, 3H), 3.36 (s, 3H), 3.36–3.54 (m, 2H), 3.58–3.62 (m, 6H), 3.66–3.70 (m, 2H), 4.10–4.17 (m, 2H), 7.34 (d, 2H, *J* = 8.6), 7.79 (d, 2H *J* = 8.3) ppm. ^{13}C-NMR (75 MHz, $CDCl_3$, 25 ºC): *d* = 21.60, 58.99, 68.61, 69.19, 70.48, 70.51, 71.84, 127.92, 129.77, 132.91, 144.74 ppm. MALDI-TOF (dithranol): *m*/*z* = 341.0 $[M+Na]^+$, 357.0 $[M+K]^+$.

1-(2-(2-(2-Methoxyethoxy)-ethoxy)ethoxy)-4-bromo- benzene (13).

To a THF (15ml) solution of mixture of 4-bromophenol (0.692 g, 4 mmol) and **12** (1.12 g, 3.5 mmol) was added KOH (1.0 g, 16 mmol), and the resulting suspension was refluxed for 15h under N_2. The reaction mixture was allowed to cool to room temperature and evaporated to dryness. The AcOEt solution of the residue was washed with water, dried over anhydrous Na_2SO_4, and then the solvent was removed under reduced pressure. The residue was subjected to column chromatography (SiO_2, AcOEt/hexane 1/1 v/v) to allow isolation of **13** as a colorless oil (0.7 g) in a 62% yield. ^{1}H-NMR (300 MHz, $CDCl_3$, 25 ºC): *d* = 3.37 (s, 3H), 3.54 (m, 2H), 3.72 (m, 6H), 3.84

(m, 2H), 4.09 (m, 2H), 6.80 (d, 2H, J = 9.0), 7.35 (d, 2H, J = 9.2) ppm. MALDI-TOF (dithranol): m/z = 356.94 $[M+K]^+$.

4-{2-[2-(2-Methoxy-ethoxy)-ethoxy]-ethoxy}-[1,'1'; 4',1'']terphenyl-4''-ol[42](3TEG).

A mixture of Na_2CO_3 (0.158 g, 1.5 mmol), $Pd(OAc)_2$ (0.003 g, 0.5 mol.%), **4** (0.236 g, 0.8 mmol), **13** (0.226 g, 0.7 mmol), distilled water (7 ml) and acetone (6 ml) was stirred for 3 h at room temperature. Afterward, the reaction mixture was evaporated to dryness, and the solution was quenched with dilute aqueous hydrochloric acid. The precipitate was washed with water. The residue was subjected to column chromatography (SiO_2, AcOEt/hexane 1/1v/v) to allow isolation of **3**TEG as a white powder (0.414g) in a 72% yield. ^{1}H-NMR (300 MHz, d_6 -DMSO, 25 ºC): d = 3.30 (s, 3H), 3.43 (m, 2H), 3.51 (m, 4H), 3.58 (m, 2H), 3.74 (m, 2H), 4.13 (m, 2H), 6.87 (d, 2H, J = 8.6), 7.03 (d, 2H, J = 8.8), 7.52 (d, 2H, J = 8.4), 7.62 (d, 6H, J = 8.1), 9.52 (s, 1H) ppm. ^{13}C-NMR (75 MHz, d_6 -DMSO, 25 ºC): d = 58.27, 67.41, 69.18, 69.83, 70.03, 70.17, 71.49, 115.14, 115.98, 126.56, 126.71, 127.73, 127.77, 130.61, 132.33, 137.90, 138.69, 157.35, 158.28 ppm. MALDI-TOF (dithranol): m/z = 408.0 $[M]^+$, 431.0 $[M+Na]^+$. HRMS (ESI) m/z calculated for $C_{25}H_{28}NaO_5$ $[M+Na]^+$: 431.1834, found 431.1831.

Characterizations of fluoresce response for metal ions by using the fluoresce probe.

Fluorescence probe **1** (*ca.* 1wt%) was mixed in each carbonate salt /and inorganic salt. Fluoresce responses were observed and the fluorescence spectra were measured as already stated in the experimental part of Chapter 2-1.

Plant growth conditions and imaging.

Seeds of *Alabidopsis thaliana* Col-0 (wild typewere) surface sterilized, sown on media with or without cesium, then grown for 9 days under long-day conditions (16 h daylight / 8h night), 22 ^{0}C. Light intensity was 70–90 μmol/m^2/sec. The media was composed of 0.5 mM KCl, 2 mM $Ca(NO_3)_2$, 0.5 mM phosphoric acid, 0.75 mM $MgSO_4$, 50 μM H_3BO_3, 10 μM $MnCl_2$, 2 μM $ZnSO_4$, 1.5 μM $CuSO_4$, 0.075 μM $NH_4Mo_7O_{24}$ and 74 μM Fe-EDTA, pH 5.8 with $Ca(OH)_2$, 1% (w/v) sucrose and 1% (w/v) SeaKem agarose, the medium was supplemented with 0.5 mM Cs_2CO_3. Freeze-dried sample were sprayed with 0.02wt% methanolic Cesium Green solution and observed under

fluorescence microscope.

Elemental analysis of Arabidopsis.

Wild type (Col-0) seedlings were grown for 9 days then washed in Milli-Q water, dried on a paper towel, placed in a paper envelope and dried in an oven at 65 °C for 3 days. Approximately 2 mg of dried samples were extracted with 1 mL of 60% (*v/v*) HNO_3 at 125 °C for 1 h, followed by 1 mL of 30% (*v/v*) H_2O_2 and diluted with Milli-Q water to a total volume of 10 mL. In order to prevent ionization of Cs^+, 0.1% (*w/v*) KCl was added to each sample and a standard solution according to the manufacturer's instructions (PerkinElmer, Waltham, MA, USA). Cs^+ concentrations were measured using a PerkinElmer AAnalyst 200 atomic absorption spectrometer and calculated against the standard curve. One-way ANOVA with Bonferroni's multiple comparison posttest ($p < 0.05$) was performed using Prism (GraphPad Software, La Jolla, CA, USA) to determine the statistical significance.

Preparation of Optode.

KDM-13 (2.9 mg, 1.0 eq.), host molecules (**1-C12**, **Biscrown** or **Calix**) (4.2 mg, 1.0 eq.), NaTFPB (6.9 mg, 1.0 eq.), PVC (30 mg) and DOS (60 mL) were dissolved in of THF (0.6 mL). The resulting mixture was stirred for 5 min, then coated onto a plastic film and allowed to dry. The prepared optode membrane was immersed in Bis-Tris buffer solution in the presence of cations (CsCl, RbCl, KCl, NaCl, $CaCl_2$ and $MgCl_2$), filled in a 1 cm cuvett, and then absorbance spectra were measured by UV/vis spectroscopy.

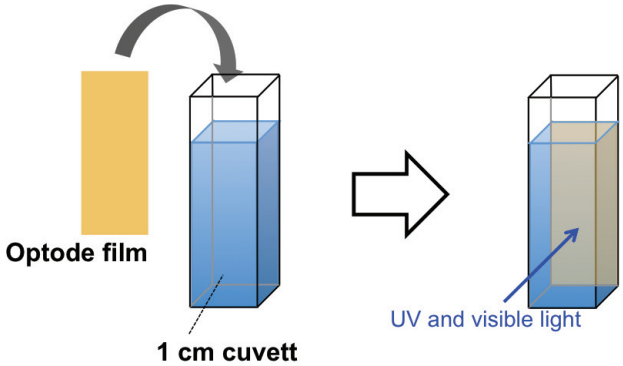

Figure 18. Schematic view of characterization of optode membranes.

Principle of optode system[44,45]

The response mechanism of the optode membrane is explained by the ion-pair extraction/ion exchange principles. In the case where a neutral ionophore, S, selective for the target ion, i^+, a deprotonated cationic dye, D, and a lipophilic anionic additive, R^- are incorporated, the response mechanism is given by the following chemical equilibrium:

$$i_w^+ + S_o + DH^+R_o^- \Leftrightarrow Si^+R_o^- + D_o + H_w^+ \qquad (1)$$

where H^+ is the hydrogen ion; DH^+R^- is the ion pair of the protonated dye and an additive, and Si^+R^- is the ion pair of the ion-ionophore complex and an additive. "o" and "w" mean that the chemical species is in the membrane phase and the water phase, respectively. The hydrogen ion is exchanged for the target ion in the water phases when the target ion complexes with the ionophore in the membrane phase. Simultaneously, the dye in the organic phase transfers from the protonated form, DH^+, to the neutral form, D, with the result that its spectrum of absorption or fluorescence changes. According to the law of mass action, the chemical equilibrium of eq. 1 gives the following equation:

$$K_{exch} = \frac{[Si^+R_o^-][D_o][H_w^+]}{[i_w^+][S_o][DH^+R_o^-]} \qquad (2)$$

where the brackets represent the concentration of the chemical species and K_{exch} is the equilibrium constant. The target ion concentration can be described with the experimental conditions of the total ionphore concentrations, $[S_{tot}]$, the total cationic dye concentration, $[D_{tot}]$, and the total anionic additive, $[R^-]$, as a follow:

$$[i_w^+]=\frac{[H_w^+]}{K_{exch}}\frac{\alpha}{1-\alpha}\frac{[R_{tot}]-(1-\alpha)[D_{tot}]}{[S_{tot}]-[R_{tot}]+(1-\alpha)[D_{tot}]} \qquad (3)$$

In this experiment, because

$$R_{tot} = S_{tot} = D_{tot} \qquad (4)$$

eq. (3) can be simplified to

$$[i_w^+]=\frac{[H_w^+]}{K_{exch}}\frac{\alpha^2}{(1-\alpha)^2} \qquad (5)$$

Here, if C is defined as a follow:

$$C = \frac{[i_w^+]K_{exch}}{[H_w^+]} \qquad (6)$$

α is described by

$$\alpha = \frac{1+2C-\sqrt{1+4C}}{2C} \qquad (7)$$

In this experiment, $[i_w^+]$ and $[H_w^+]$ can be obtained from a concentration of cation and pH of buffer solution. By using eq. 7, the calibration curve can be obtained by fitting the experimental points, and also the value of K_{exch} can be obtained.

References

(1) Essen L.; Parry J. V. L. *Nature* **1995**, *176*, 280–282.

(2) Glisin V.; Crkvenjakov R.; Byus C. *Biochemistry* **1974**, *13*, 2633–2637.

(3) Butterman W. C.; Brooks W. E.; Reese R. G. Jr Mineral commodity profile: caesium *Open-File Report* **2004**, 2004–1432 (Virginia: US Geological Survey) p 5.

(4) Johnson G. T.; Lewis T. R.; Wagner W. D. *Toxicol. Appl. Pharmacol.* **1975**, *32,* 239–245.

(5) International Atomic Energy Agency 2006 Environmental consequences of the Chernobyl accident and their remediation: twenty years of experience *Report of the UN Chernobyl Forum Expert Group 'Environment'* (Vienna: IAEA) STI/PUB/1239.

(6) Brumfiel G. *Nature* **2011**, *478*, 435–436.

(7) Mangano J. *Bull. Atom. Sci.* **2004**, *60*, 30–35.

(8) Langham W. H.; Andersen E. C. *Health Phys.* **1959**, *2*, 30–48.

(9) Rowan D. J.; Rasmussen J. B. *Can. J. Fish. Aquat. Sci.* **1994**, *51*, 2388–2410.

(10) Rahman M. M.; Voigt G. *J. Environ. Radioact.* **2004**, *71*, 127–138.

(11) Turekian K. K.; Wedepohl K. H. *Geol. Soc. Am. Bull.* **1961**, *72*, 175–192.

(12) Kaneyasu N.; Ohashi H.; Suzuki F.; Okuda T.; Ikemori F. *Environ. Sci. Technol.* **2012**, *46,* 5720–5726.

(13) *Visualization of Radioactive Substances with JAXA's 'Ultra-Wide-Angle Compton Camera'* www.jaxa.jp/press/2012/03/20120329 compton e.html
29 March 2012.

(14) *Toshiba Develops Camera to Detect Radiation Hotspots* http://techon.nikkeibp.co.jp/english/NEWS EN/20111214/202583/ 14 December 2011

(15) Matsunami M.; Takaki A.; Maekawa H.; Nishiguchi I. *Sci. Technol. Adv. Mater.* **2005**, *6*, 172–180.

(16) Bureekaew S.; Shimomura S.; Kitagawa S. *Sci. Technol. Adv. Mater.* **2008**, *9*, 014108.

(17) Ariga K.; Hill J. P.; Lee M. V., Vinu A.; Charvet R.; Acharya S. *Sci. Technol. Adv. Mater.* **2008**, *9*, 014109.

(18) Li M.; Ishihara S.; Ji Q.; Akada M.; Hill J. P.; Ariga K. *Sci. Technol. Adv. Mater.* **2012**, *13*, 053001.

(19) Ohshima A, Momotake A and Arai T *Sci. Technol. Adv. Mater.* **2005**, *6*, 633–643.

(20) Kuroiwa K, Oda N and Kimizuka N *Sci. Technol. Adv. Mater.* **2005**, *7*, 629–634.

(21) Xing Z. C.; Chang Y.; Kang I. K. *Sci. Technol. Adv.Mater.* **2010**, *11*, 014101.
(22) Brown W. H.; Foote C. S.; Iverson B. L.; Anslyn E. V.; Novak B. M. 2011 *Organic Chemistry* 6th edn (Belmont, CA: Brooks/Cole) chapter 21, p 853–905.
(23) Yamaguchi I.; Goto K.; Sato M. *Tetrahedron* **2009**, *65*, 3645–3652.
(24) Yamaguchi I.; Goto K.; Sato M *Macromolecules* **2009**, *42*, 7836–7845.
(25) Förster T. 1965 Delocalized excitation and excitation transfer *Modern Quantum Chemistry. Istanbul Lectures. Part III: Action of Light and Organic Crystals* ed O Sinanoglu (New York: Academic) p 93–137.
(26) Birks J. B. *Rep. Prog. Phys.* **1975**, *38*, 903–137.
(27) Hampton, C. R.; Bowen, H. C.; Broadley, M. R.; Hammond, J. P.; Mead, A.; Payne, K. A.; Prichard, J.; White, P. J. Cesium Toxicity in Arabidopsis *Plant Physiol.* **2004** *136*, 3824–3837.
(28) Adams, E.; Abdollahi, P.; Shin, R. *Int. J. Mol. Sci.* **2013**, *14*, 4545–4559.
(29) Apse, M. P.; Blumwald, E. *FEBS Lett.* **2007**, *581*, 2247–2254.
(30) Frisch M. J. *et al* 2009 *Gaussian 09* revision A.01 (Wallingford, CT: Gaussian)
(31) Valeur B.; Leray I. *Coord. Chem. Rev.* **2000**, *205*, 3–40.
(32) Bourson J.; Valeur B. *J. Phys. Chem.* **1989**, *93*, 3871–3876.
(33) Samshuddin S.; Butcher R. J.; Akkurt M.; Narayana B.; Sarojinid B. K.; Yathirajane H. S. *Acta Crystallogr.* **2012**, *E68*, o74– o75.
(34) Bakker, E.; Simon, W. *Anal. Chem.* **1992**, *64*, 1805–1812.
(35) Bakker, E.; Buhlmann, P.; Pretsch, E. *Chem. Rev.* **1997**, *97*, 3083–3132.
(36) Buhlmann, P.; Pretsch, E.; Bakker, E. *Chem. Rev.* **1998**, *98*, 1593–1687.
(37) Seo, H. S.; Lee, S. H. *J. Fluoresc.* **2011**, *21*, 747–751.
(38) Zeng, H. H.; Dureault, B. *Talanta* **1998**, *46*, 1485–1491.
(39) Hisamoto, H.; Tohma, H.; Yamada, T.; Yamauchi, K.; Siswanta, D.; Yoshioka, N.; Suzuki, K. *Anal. Chim. Acta* **1998**, *373*, 271–289.
(40) Luboch, E.; Cygan, A.; Biernat, F. J. *Tetrahedron* **1991**, *47*, 4101–4112.
(41) Cadogan, A.; Diamond, D.; Smyth, M. R.; Svehla, G.; McKervey, M. A.; Seward, E. M.; Harris, S. J. *Analyst* **1990**, *115*, 1207–1210.
(42) Liu L.; Zhang Y.; Xin B. *J. Org. Chem.* **2006**, *71*, 3994–3997.
(43) Ouchi M.; Inoue Y.; Liu Y.; Nagamune S.; Nakamura S.; Wada K.; Hakushi T. *Bull. Chem. Soc. Japan* **1990**, *63*, 1260–1262.
(44) Kurihara, K.; Nakamura, K.; Hirayama, E.; Suzuki, K. *Anal. Chem.* **2002**, *74*,

6323–6333.
(45) Bakker, E.; Bühlmann, P.; Pretsch, E. *Chem.Rev.* **1997**, *97*, 3083–3132.

Chapter 4
Development of Photo-Functional Systems with Molecular Assemblies Formed by Surfactants

4-1 Photo-Responsive Molecular Assembly Systems and their Structural Characterization using Small-Angle Neutron Scattering

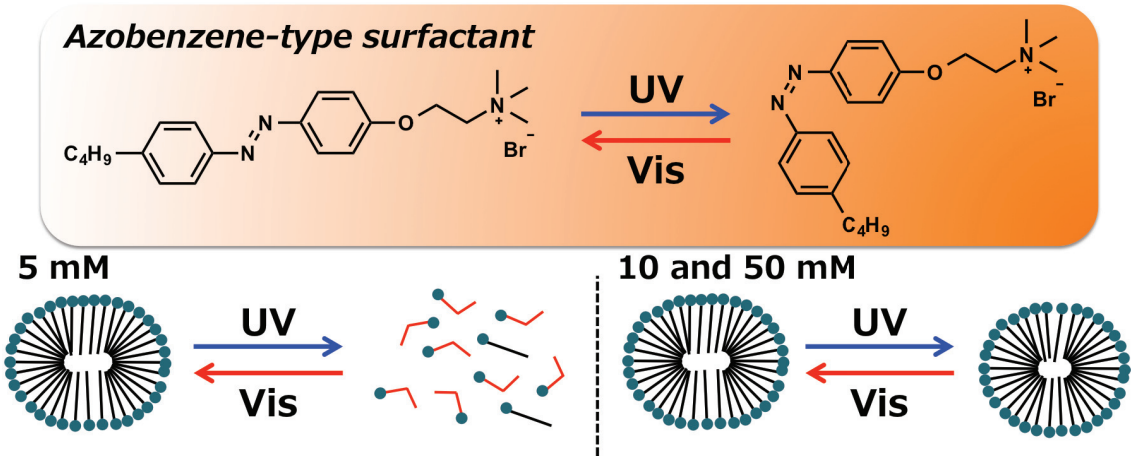

Abstract

Photo-responsive micellar systems of 4-butylazobenzene-4′-(oxyethyl)trimethylammonium bromide (AZTMA) were examined with and without ethylbenzene using small-angle neutron scattering (SANS). Analysis of SANS profiles showed that an aqueous solution containing 5, 10 and 50 mM AZTMA forms prolate spheroids with a long radius (R_a) of 38 Å and a short radius (R_b) of 21 Å. In the 5 mM AZTMA solution, the concentration of micelles decreased upon UV light irradiation, while their size and shape remained almost unchanged. Subsequent visible light irradiation reversed the decrease and increased the number of micelles. In contrast, 10 and 50 mM AZTMA solutions showed that the number and long radius of the micelles decreased with UV light irradiation, while subsequent exposure to visible light irradiation restored them. For AZTMA micellar solutions equilibrated with excess ethylbenzene, the solubilized amount of ethylbenzene increased upon UV light irradiation due to enhanced swelling of the micelles with *cis*-AZTMA. This photoinduced uptake of the solubilizate has potential applicability for the collection and removal of hazardous oily substances.

4-1-1 Introduction

Molecular assemblies that form or break up upon application of external stimuli, such as light,[1–7] a redox reaction,[8] a magnetic field,[9] a temperature change,[10] or a pH change,[11] have been applied for triggering controlled release in drug delivery systems and personal careproducts such as perfume. In particular, light is a promising stimulus because it is clean and easy to apply. Therefore, photoinduced formation and breakup of micelles[5,6] and vesicles[2,4,7] have been studied widely. For example, Eastoe *et al.* developed a photo-responsive gemini surfactant containing a stilbene unit as the photo-responsive component.[12] Vesicles formed by the surfactant transformed into small spherical micelles upon UV irradiation.

Our group has previously reported the reversible controlled release and uptake of hydrophobic solutes with cationic surfactant micelles containing an azobenzene unit as a photo-responsive moiety.[13] Ultraviolet irradiation of an aqueous *trans*-AZTMA solution with solubilized ethylbenzene resulted in photo-isomerization to the *cis* isomer, which caused the release of a portion of the solubilized ethylbenzene (Figure 1). Subsequent visible light irradiation of the *cis*-AZTMA solution resulted in photo-isomerization back to the *trans* isomer, resulting in resolubilization of the released ethylbenzene. However, the mechanism involved in this release and uptake system using light irradiation has not been elucidated. A thorough understanding of this system could provide the information needed to develop a more effective photo-induced controlled release system. The amount of solubilization is strongly related to micelle characteristics. To understand the variation in solubilized amounts of ethylbenzene in AZTMA micelles upon photoirradiation, the micelle structure before and after UV light irradiation must be examined in detail.

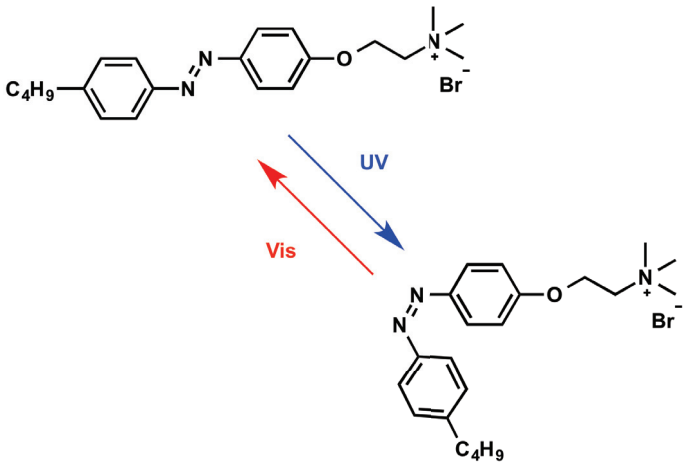

Figure 1. Molecular structure of AZTMA and the structural changes induced by UV and visible light irradiation.

Small-angle neutron scattering (SANS) allows the direct determination of micelle structure, in situ, allowing changes resulting from irradiation to be determined directly. Using SANS,[14] Abbott *et al.* revealed that a mixture of sodium dodecyl sulfate and a photo-responsive cationic bolaform surfactant containing a photo-responsive azobenzene moiety underwent a transformation from a dispersion of vesicles with a bilayer thickness of 35 ± 2 Å into cylindrical micelles with a cross-sectional radius of 19 ± 3 Å under UV light irradiation.

In this section, SANS has been used to examine how photoirradiation affects the structure of AZTMA micelles with and without an oily solubilizate, ethylbenzene.

4-1-2. Results and discussion

4-1-2-1 Photoisomerization of an Azobenzene type cationic surfactant in aqueous solutions monitored by UV/vis absorptions measurements

Figure 2 shows changes in the UV/Vis absorption spectra of a 5 mM AZTMA solution as a function of UV irradiation time. Ultraviolet irradiation decreased the absorption at 350 nm assigned to the *trans* form and resulted in simultaneous appearance of a new peak at 431 nm assigned to the *cis* isomer, indicating photo-isomerization of the AZTMA. The spectra reached a photostationary state after about 5 min irradiation, and it contains *trans*- (*ca*. 15%) and *cis*-AZTMA (*ca*. 85%) isomers (Figure 2c). Subsequent irradiation with visible light for 15 min resulted in recovery of the peak at 350 nm. 10 mM AZTMA solutions also underwent reversible photo-isomerization, with photostationary states obtained after 15 min UV (*ca*. 20% of *trans*- and *ca*. 80% of *cis*-isomers) and 20 min visible light (*ca*. 85% of *trans*- and *ca*. 15% of *cis*-isomers) irradiation (Figures 2c, 2d). In contrast, the 50 mM AZTMA solution produced only small spectral changes, and 60 min (UV; *ca*. 35% of *trans*- and *ca*. 65% of *cis*-isomers) and 30 min (visible light; *ca*. 90% of *trans*- and *ca*. 10% of *cis*-isomers) were needed to achieve a photostationary state (Figures 2c and 2d). These results indicate that increase in AZTMA concentration increases the amount of time required for achieving a photostationary state. This is because that the much greater absorption of concentrated solutions requires longer irradiation times for achieving a photostationary state.

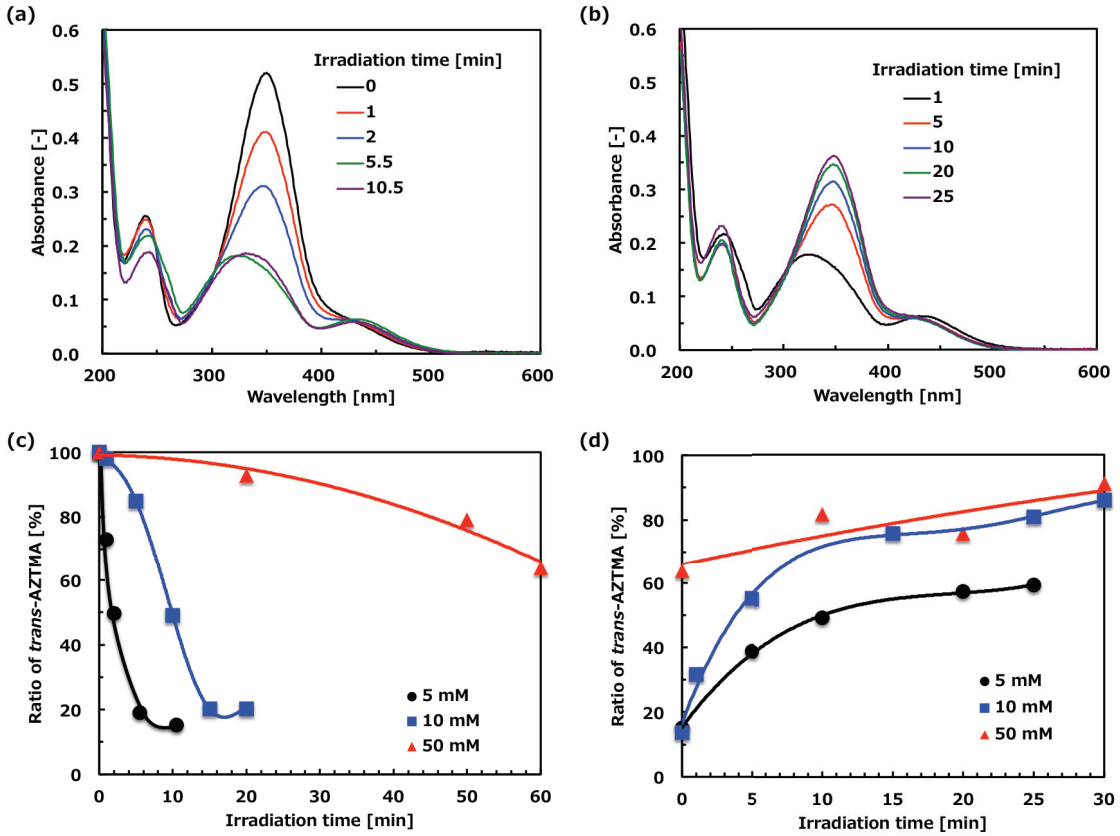

Figure 2. Variations in UV/Vis absorption spectra of 5 mM aq. AZTMA after (a) UV and (b) visible light irradiation (solutions were diluted 100-fold before the measurements) and ratios of *trans*-AZTMA in 5, 10, and 50 mM AZTMA solutions as a function of (a) UV and (b) visible light irradiation time.

4-1-2-2 Small-angle neutron scattering measurements and analysis of AZTMA single aqueous systems

Figure 3a shows SANS profiles for 5 mM AZTMA solutions as a function of UV and, subsequently, visible light irradiation time. Before UV irradiation, the scattered intensity is low due to the low concentration used, but the scattering profile indicates small, spherical micelles. The data were fitted to a model of uniform prolate spheroids[18] with a long radius (R_a) of about 39 Å and a short radius of about 21 Å present at a volume fraction of 0.00084. This is in good agreement with the expected volume fraction of micelles in a 5 mM *trans*-AZTMA solution, corrected for the CMC of 2.7 mM, which should be between 0.00078 and 0.00097, depending on the degree of bromide counterion association.

Ultraviolet light irradiation decreased the scattering intensity which depends on the volume fraction of micelles until the solution is below the CMC of the *cis* isomer and none micelles can be detected (Figure 4a). The low angle scattering seen at long irradiation times (and in all scattering patterns) is attributed to microbubbles on the surface of the SANS cell stabilized by adsorbed cationic surfactant, or the difference between the background and the scattering can't be measured adequately due to the low scattering intensity (because a profile at the low q region is sensitive). These have been seen in other systems very near their CMCs.[19] At higher concentrations, *vide infra*, this effect is negligible. Throughout irradiation the micelle diameter remained unchanged from a long radius (R_a) of about 39 Å and a short one of about 21 Å. Subsequent visible light irradiation caused the scattering intensity to increase back to its original value, which suggests that reversible formation and breakup of micelles (Figures 3a and 4a).

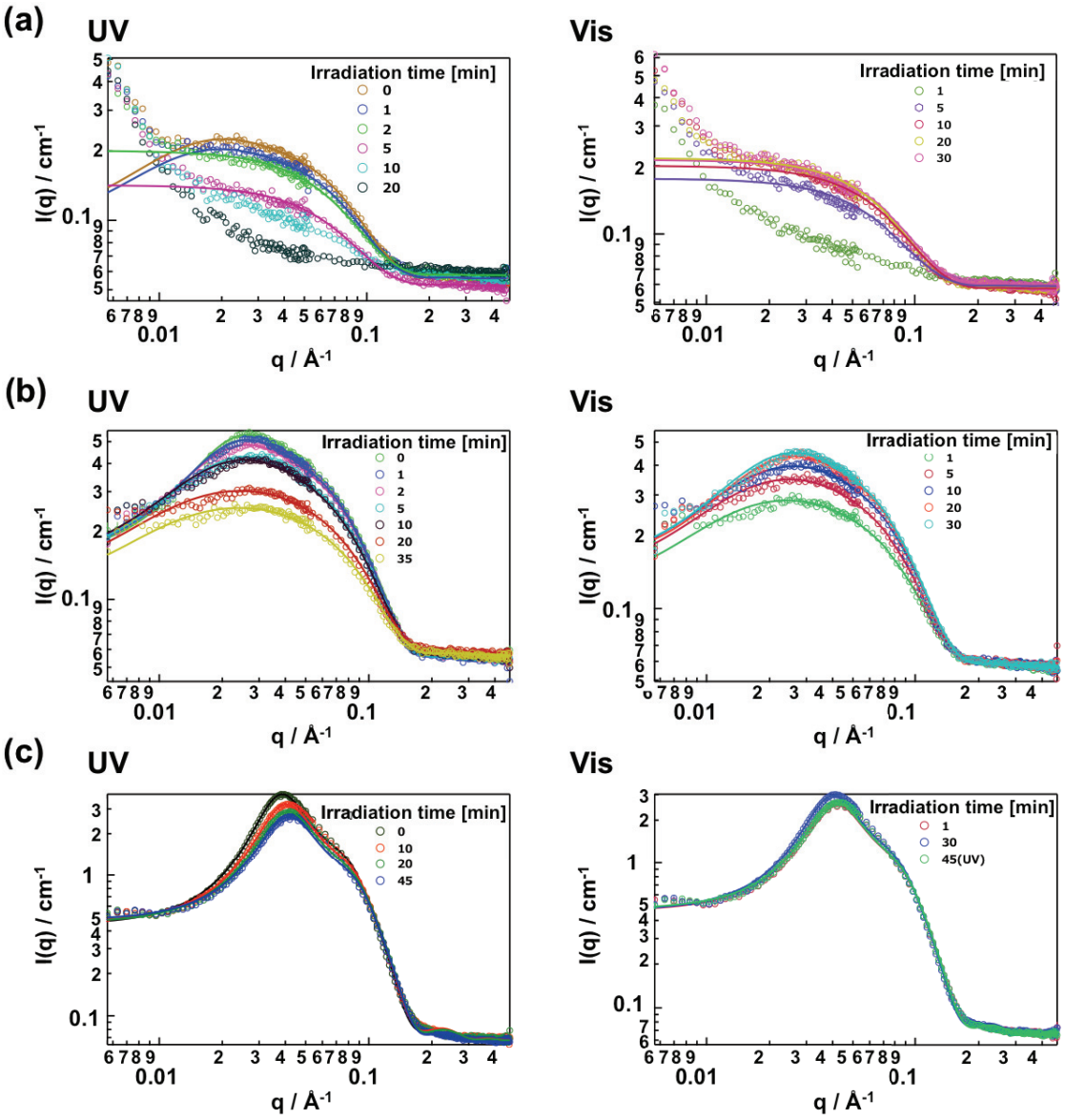

Figure 3. SANS profiles with fitting results after UV and visible light irradiation of (a) 5 mM, (b) 10 mM, and (c) 50 mM aq. AZTMA solutions.

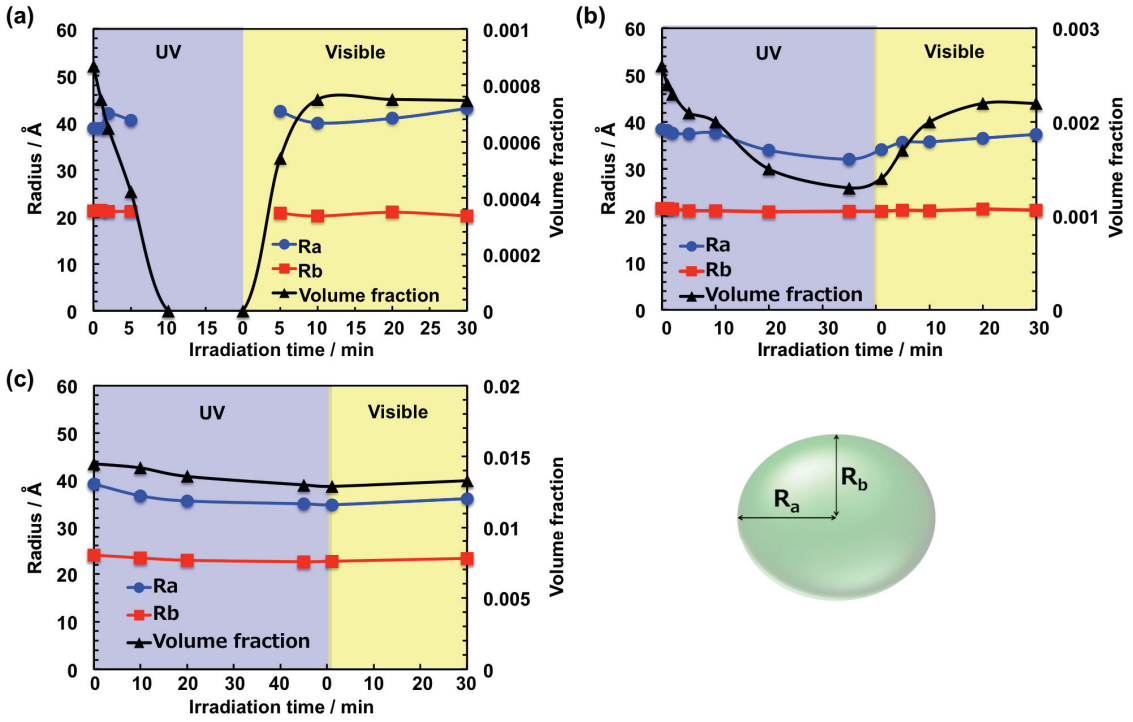

Figure 4. Variation in SANS fit values for (a) 5 mM, (b) 10 mM, and (c) 50 mM aq. AZTMA solutions after UV and visible light irradiation. Uncertainties are ±5% for scales and volume fractions and ±0.5 Å for mean radius.

At higher concentrations (10 and 50 mM AZTMA), which were above the CMCs for both the *trans* and *cis* isomers, the SANS profiles exhibited a broad peak (Figures 3b and 3c), indicating interactions between micelles. These data were again fitted to a model of homogenous prolate spheroids,[18] but also included a structure factor describing electrostatic interactions between micelles through a screened Coulomb potential.[20,21] Before irradiation, the long radius (R_a) was about 38 Å and the short radius (R_b) was 21 Å for both the 10 and 50 mM solutions (Figures 4b and 4c). Upon UV light irradiation of the 10 mM AZTMA solution, the scattering intensity decreased, broadened and moved to higher angle, indicating a decrease in the concentration of micelles. Thus, the concentration of micelles decreased because the CMC for the *cis* form was greater than that for the *trans* form. However, for the 10 mM AZTMA system, the volume fraction was greater than zero (0.0013), even in the photostationary state after UV light irradiation. This difference is due to the existence of micelles after UV light irradiation because the concentration of 10 mM is greater than the CMC for *cis*-AZTMA. This variation in volume fraction corresponded to changes in the

photo-isomerization ratio (Figures 2c and 3b) In addition, the long radius (R_a) decreased to about 32 Å upon UV light irradiation (Figure 4b), while short radius (R_b) remained unchanged (21 Å). Subsequent visible light irradiation restored the peak position and scattering intensity, and recovered the original long axis radius. In contrast, the profiles for the 50 mM AZTMA solution changed slightly upon both UV and visible light irradiation (Figures 3c and 4c), indicating that the changes in a ratio of *trans*- and *cis*-AZTMA is small at the higher concentration with light irradiation. At 50 mM, UV irradiation causes similar changes the scattering profiles, reducing intensity and moving the structure factor peak to higher angle. Here, far above the CMCs of both the *cis* and *trans* isomers, the changes are smaller due to the smaller impact of this CMC difference. Visible light did not recover the original micelle structure even after 45 minutes irradiation, which we attribute to the higher optical density of the concentrated solution but lower extinction coefficient of the *cis* isomer. These results demonstrate that at higher concentrations, UV and visible light irradiation reversibly changes the size and interactions of micelles.

The results showed that the long radius (R_a) of the micelles decreases upon UV light irradiation in 10 and 50 mM AZTMA solutions, but, somewhat surprisingly, the short radius does not. As the effective chain length of the *cis* form is much shorter than that of the *trans* form (Figure 1), a decrease in the short micelle radius was expected to accompany UV irradiation. This occurs because the photostationary state achieved by UV irradiation contains both *trans*- (*ca*. 20%) and *cis*-AZTMA (*ca*. 80%) isomers, so the micelle structures are determined by the two components. In particular, the smallest micelle radius is determined by the longer alkyl chain length component. For example, oblate spherical micelles of dodecyltrimethylammonium bromide (DTAB) form upon addition of a surfactant with a long chain, cetyltrimethylammonium bromide (CTAB).[22] In this case, increasing the amount of the shorter surfactant (DTAB) decreases the length of the micelles while maintaining their thickness (*i.e.*, short radius). Similarly, using fluorescent probes with long alkyl chains to measure micelle sizes, it has been shown that even one long-chained probe per micelle can substantially increase aggregation number.[23] Thus, in the present AZTMA system, the radius of the long axis decreased because the percentage of *cis*-AZTMA having a shorter hydrophobic unit increased (Figure 5), but even a small population of *trans*-AZTMA is sufficient to maintain the same value of R_b.

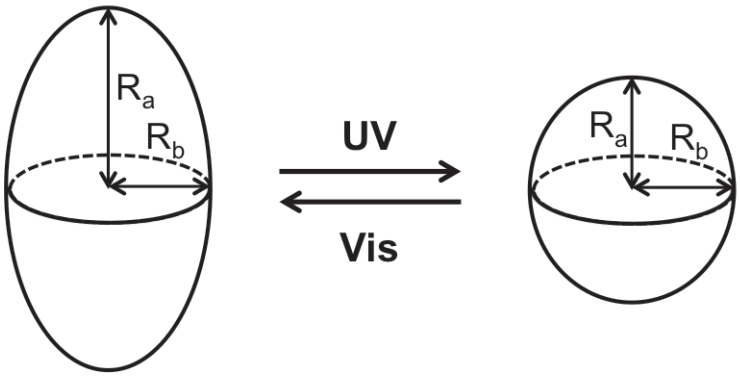

Figure 5. Morphological changes to AZTMA micelles in 10 mM aqueous solutions after UV and visible light irradiation.

These results indicate that micelle concentrations reversibly decrease and increase upon UV and visible light irradiation, respectively, at concentrations near the CMC for AZTMA. In addition, changes in micelle morphology are induced at concentrations greater than the CMC by the photo-isomerization reaction of AZTMA. These results suggest that light irradiation causes changes in the solubilizing capacity of micelles for oily substances.

4-1-2-3 SANS measurements and analysis of AZTMA aqueous solutions solubilizing an oily substance

Next, SANS measurements were obtained for aqueous AZTMA solutions saturated with ethylbenzene. In these systems the solutions studied contained a small excess of ethylbenzene in contact with the micellar solution but out of the beam path, so that the system remained saturated. Results are shown in Figure 6.

SANS data for the 5 and 10 mM AZTMA systems were fitted to a model of disperse spheroids[20,24,25] (Figures 6a, 6b). The polydispersity was quite small for both concentrations (Table 1). Compared to systems without ethylbenzene, the volume fraction and radius increased, which suggests that ethylbenzene molecules are solubilized in the core of the AZTMA micelles and increase the size of the micelles. A previous study reported that hydrophobic solubilizates increase the size of micelles.[26–30] By irradiating these solutions with UV light, both the volume fraction and radius were increased. However, subsequent visible light irradiation did not affect these parameters, which indicates that UV irradiation causes greater swelling of the micelles when

ethylbenzene is used. In addition, the structures of the micelles with ethylbenzene do not return to their initial states, even after visible light irradiation. The SANS profiles for the 50 mM system with solubilized ethylbenzene were fitted to a core-shell model with a polydisperse core of constant shell thickness.[16,20] Ultraviolet light irradiation also increased the volume fraction and size (the core) of aggregates. Subsequent visible light irradiation did not affect these parameters. In contrast, the number of micelles, calculated from the volume fraction and size at each concentration, decreased upon UV light irradiation (Table 1). This decrease in the number of micelles is consistent with values in systems without ethylbenzene. The behavior of change in the volume fraction and size induced by UV light irradiation differs from the previous report[13] and is thought to be due to the solubilization conditions for the present system, in which an excess amount of ethylbenzene exists as an oil phase at the top of the aqueous solutions. While, ethylbenzene was added to each AZTMA solution after light irradiation in previous reports; the present study involved light irradiation of solutions that solubilized the ethylbenzene.

To examine the difference in results, the amount of solubilizates in micelles of AZTMA was quantitatively evaluated using HPLC. The solubilization amount of ethylbenzene in 5, 10, or 50 mM AZTMA solutions increased with UV light irradiation, and remained high with subsequent visible light irradiation (Figure 7), which indicates that micelles of AZTMA take in more ethylbenzene upon UV light irradiation. This uptake behavior is due to the affinity of mixed micelles of *trans*- and *cis*-AZTMA toward ethylbenzene. The number of ethylbenzene molecules solubilized in one AZTMA micelle, calculated with the solubilization amounts, increases from about 200 to 300 with UV light irradiation. Also, after UV light irradiation, the 5 mM mixed *trans*- and *cis*-AZTMA solution with excess ethylbenzene formed micelles, despite being below the CMC for *cis*-AZTMA (8.2 mM) (Figure 6a and Table 1). These results indicate that ethylbenzene molecules have a strong affinity toward the mixed micelles. Thus, micellar solutions of *cis*-AZTMA solubilize more ethylbenzene than *trans* solutions in the presence of an excess amount of ethylbenzene. This photo-induced uptake behavior may be useful for removing hazardous oily substances from aqueous solutions.

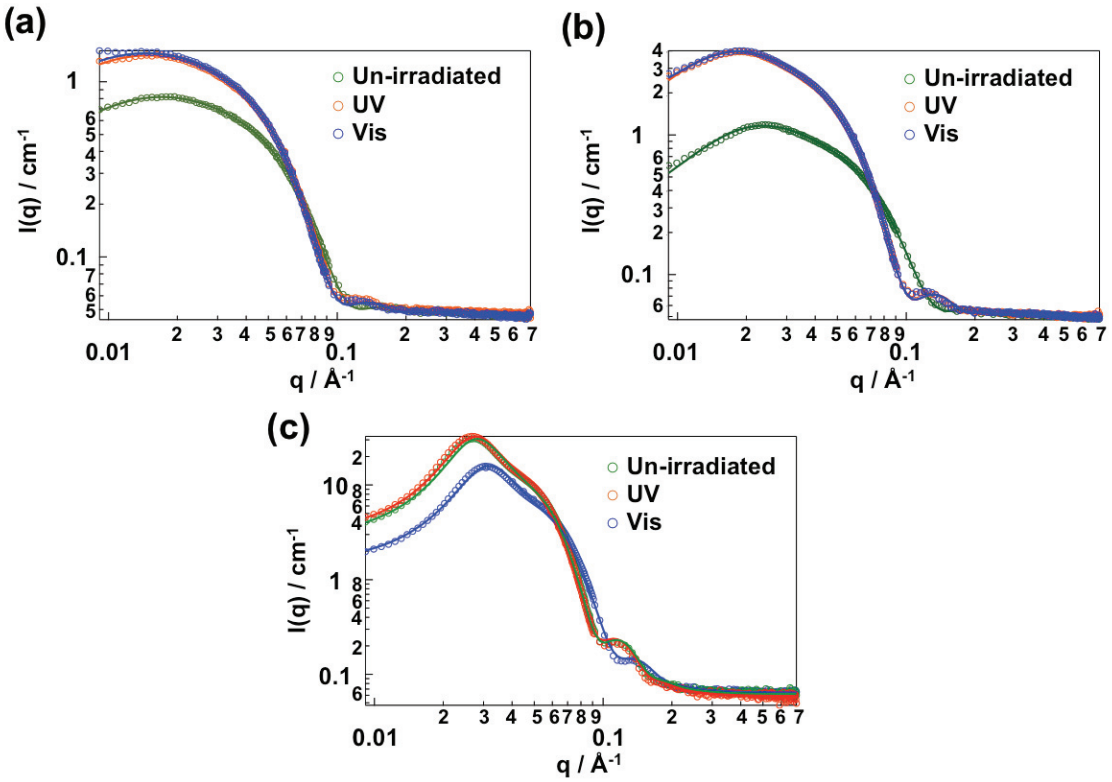

Figure 6. SANS profiles with fitting results after UV and visible light irradiation of (a) 5 mM, (b) 10 mM; and (c) 50 mM aq. AZTMA solutions saturated with ethylbenzene.

Table 1 SANS fit values for aq. AZTMA solutions saturated with ethylbenzene after UV and visible light irradiation

AZTMA/ mM	5			10			50		
	Initial	UV	Visible	Initial	UV	Visible		Initial	UV	Visible
ϕ	0.0013	0.0016	0.0016	0.0030	0.0042	0.0042	f	0.024	0.028	0.028
r/Å	35.7	40.5	40.5	30.0	41.9	42.0	r_c/Å	22.2	29.7	30.5
p	0.13	0.14	0.15	0.15	0.13	0.13	p_c	0.25	0.20	0.21
							r_c+t	38.2	45.7	46.5
C_m/mM	0.0113	0.0095	0.0095	0.0440	0.0226	0.0225	C_m/mM	0.169	0.116	0.114

Spheres with Shultz size distribution model[a] and polydisperse core with constant shell thickness[b] are modeled. ϕ is volume fraction; r and p are mean radius and polydispersity of radius, respectively; r_c, p_c, and t are mean core radius, core polydispersity, and shell thickness, respectively; C_m is the concentration of micelles. Uncertainties are ±5% for scales and volume fractions, ±0.5 Å for mean radius.

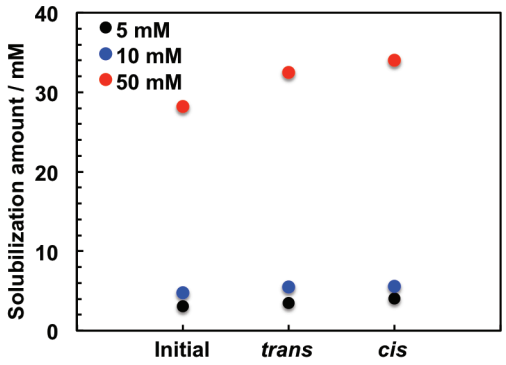

Figure 7. Variation in solubilization amount of ethylbenzene in aq. AZTMA solutions after UV and visible light irradiation.

4-1-3 Conclusions

Small-angle neutron scattering (SANS) measurements were carried out on photo-responsive surfactant (AZTMA) systems. A 5 mM aqueous AZTMA solution forms prolate-spheroid micelles. Upon UV and visible light irradiation, the volume fraction of scattering objects (concentration of micelles) decreased and increased, respectively. SANS profiles for 10 and 50 mM solutions were also fitted to a model of prolate spheroids. Ultraviolet irradiation progressively decreased the long radius and volume fraction. However, they recovered upon visible light irradiation. On the other hand, UV irradiation increased the size and volume fraction through solubilization of ethylbenzene into the AZTMA micelles, indicating that micelles of AZTMA take in more ethylbenzene upon isomerization from the *trans* to the *cis* form. This photoinduced uptake of oily substances is expected to be useful for collection of hazardous oily substances from aqueous solutions.

4-1-4 Experimental part

Materials.

AZTMA was synthesized as described previously.[13] Ethylbenzene (98%, Aldrich) and D_2O (98%, C/D/N isotope) were used as received without further purification.

Sample preparations.

Solutions of 5, 10 and 50 mM AZTMA in D_2O were prepared. The critical micelle concentrations (CMC) of AZTMA in its *trans* and photostationary (*cis*) forms were 2.7 and 8.2 mM, respectively.[13] In the solubilization study, an excess of ethylbenzene was added to D_2O solutions of 5, 10, and 50 mM AZTMA. These were maintained at room temperature for at least 1 day to reach an equilibrium saturation.

UV and visible light irradiation.

UV and visible light irradiation was conducted using an Oriel 200 W mercury arc lamp. Irradiation wavelength ranges (UV < 400 nm; visible light > 400 nm) were accomplished using color filters. Each solution was irradiated with light (10 mW/cm^2) in a quartz cuvette also used for SANS measurements. Ethylbenzene-saturated samples were exposed to UV light irradiation under stirring in 1-cm quartz cuvettes also used for UV/Vis absorption measurements. Photoisomerization rates were monitored through UV/Vis absorption spectrophotometry in a 1.0-cm quartz cuvette.

High Performance Liquid Chromatography (HPLC).

Variations in the amount of ethylbenzene were characterized using a high-performance liquid chromatography system (Capcell Pak C18 AQ column, Shiseido) equipped with a UV-2075 Intelligent UV/Vis detector (Jasco) using a mixture of acetonitrile and 20 mM ammonium acetate as the mobile phase.

Experimental section for Small-Angle Neutron Scattering (SANS).

SANS measurements were conducted on samples in 2 mm path length quartz cells with or without ethylbenzene in two facilities. One facility was the NIST Center for Neutron Research (NCNR) at the National Institute of Standards and Technology (NIST), Gaithersburg MD, on the NG7-SANS beam line[29] with 6.0 Å neutrons collected at 1.3-m and 9-m sample-to-detector distances, which gave a combined q

range of 0.008–0.3 $Å^{-1}$. The other facility was the Quokka beam line[30] at the Bragg Institute at the Australian Nuclear Science and Technology Organization (ANSTO), Australia, with 4.5–40 Å neutrons collected at 1.3-m and 8-m sample-to-detector distances, giving a combined q range of 0.004–0.7 $Å^{-1}$. Data reduction and analysis were performed with Igor Pro (Wave-metrics Inc., version 6.33J) using the NIST reduction and analysis macros (version 7.2).[31]

4-1-5 Theory of Small-Angle Neutron Scattering (SANS).

Colloidal particles (approximately 10-10^4 Å) can be studied by means of small-angle X-ray and neutron scattering (SAXS and SANS) to reveal their size, shape, and internal structure because these scales are fit to the region of these techniques as depicted by Bragg equation (eq. 1).[32]

$$2d\sin\theta = n\lambda \qquad (1)$$

A scattering of X-ray from a scatter is derived from electron density because X-ray is an electromagnetic ray bearing a charge. On the other hand, a neutron is an uncharged subatomic particle, but mainly interacts with a matter through the short-range strong nuclear force and their magnitude moments. These interactions make neutron scattering as X-ray one. From this difference of the scattering principle, neutron can be a unique probe to reveal the structures of colloidal objects. For example, neutron is likely to penetrate the bulk material, compared to X-ray and also light.

As mentioned above, neutron scattering is derived from an interaction with the atom core. The extent of neutron scattering with each atom core is expressed by scattering density. As shown in Table 2, ^{1}H has a quite low value of scattering length density, compared to other atoms. This means that ^{1}H significantly scatters neutrons.

Table 2. Scattering length of atoms.[33]

Atom	Scattering length / 10^{-12} cm
^{1}H	-3.741
D (^{2}H)	0.6671
^{12}C	0.6646
^{16}O	0.5803
^{19}F	0.5650
^{23}Na	0.3580
^{31}P	0.5131
^{32}S	0.2847
Cl	0.9577

A scattering length density of a molecule, which shows an extent of neutron scattering from it, is calculated with a sum of scattering length of atoms, composed of

the molecule, and the density. As shown in Table 3, because scattering length density of D_2O is significantly smaller than one H_2O, a neutron scattering from D_2O is low. Moreover, general organic molecules are composed of ^1H, which shows strong scattering. Thus, when neutron scattering is conducted for molecular assembles, forming in deutrated solvents, the scattering from the assembles can be effectively corrected.

Table 3. Scattering length density of light and heavy water.[33]

Solvent	Scattering length density / 10^{10} cm^{-2}
H_2O	-0.560
D_2O	6.356

The intensity of the scattering, I is measured as a function of a scattering angle, θ (Figure 8).

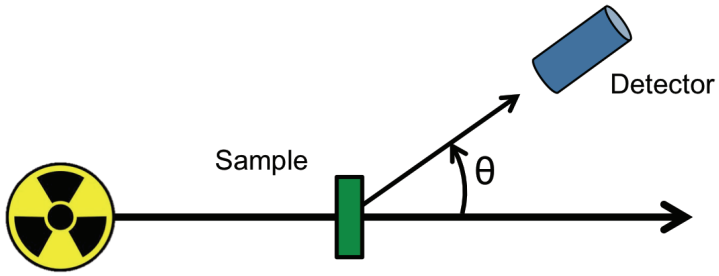

Figure 8. Schematic instrumental setup of a small-angle neutron scattering experiments.

In small-angle neutron scattering experiments, *I* is expressed as function of a scattering vector, defined by eq. 2 (Figure 9).

$$q = \frac{4\pi}{\lambda}\sin(\frac{\theta}{2}) \qquad (2)$$

The scattering intensity is given by

$$I(q) = NP(q)S(q) \qquad (3)$$

where N is the number of particles, $P(q)$ form factor, and $S(q)$ structure factor.[32]

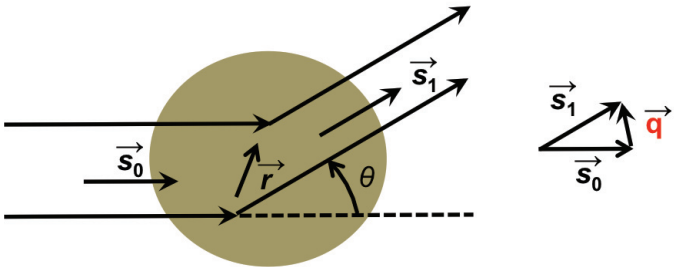

Figure 9. Geometrical relationships in scattering experiments.

Figure 10 shows an example of neutron scattering profile. q value has a dimension of a reciprocal of a length. Thus, the scattering profile in the region of low q represent information about the longer scale of the scatter, and one in the region of high q represents information about its shorter scale. Generally, scattering profiles can be considered as three regions (Figure 10). Firstly, a scattering in region A (called Guinier region) exhibits a size of a particle (scatter). Secondly, region B (called intermediate region) gives a shape of the particle. Thirdly, region C (called Prod region) represents a structural information o the surface.

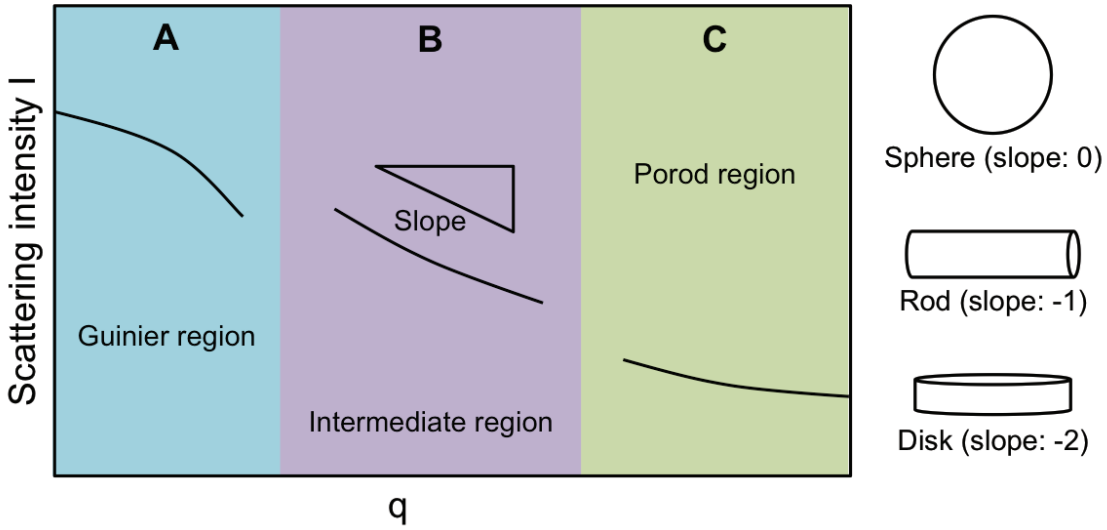

Figure 10. An example of scattering profile.

From eq. 3, obtained scattering profiles are consisted of individual particles and interpartcle scattering ($P(q)$ and $S(q)$). We can consider these contributions to total scattering individually. If there are no interactions, the scattering is just from form factor $P(q)$. For data on a log-log plot, the power law gives the shape, e. g. 0 for small

particles, -1 for rods, and -2 for disks. On the other hand, when a contribution of $S(q)$ due to interparticle interactions appear, low q scattering is significantly altered. Typically, a risen peak is derived from distance correlations between scatters. There are many models for $P(q)$ for the shape and $S(q)$ for interactions. By fitting the theoretical curve to experimental one, detailed information for the scatters (shapes, sizes, volume fractions, interactions, etc.) can be obtained.

References

(1) Eastoe, J.; Vesperinas, A. *Soft Matter* **2005**, *1*, 338–347.

(2) Bonini, M.; Berti, D.; Di Meglio, J. M.; Almgren, M.; Teixeira, J.; Baglioni, P. *Soft Matter* **2005**, *1*, 444–454.

(3) Aikawa, S.; Shrestha, R.; Ohmori, T.; Yuko, F.; Yoji, T.; Endo, T.; Kanjiro, T.; Koji, T.; Kazutami, S.; Kenichi, S.; Masahiko, A.; Hideki, S. *Langmuir* **2013**, *29*, 5668–5676.

(4) Matsumura, A.; Tsuchiya, K.; Torigoe, K.; Sakai, K.; Sakai, H.; Abe, M. *Langmuir* **2011**, *27*, 1610–1617.

(5) Gohy, J.; Zhao, Y. *Chem. Soc. Rev.* **2013**, *42*, 7117–7129.

(6) Ketner, A. M.; Kumar, R.; Davies, T. S.; Elder, P. W.; Raghavan, S. R. *J. Am. Chem. Soc.* **2007**, *129*, 1553–1559.

(7) Oh, H.; Ketner, A. M.; Heymann, R.; Kesselman, E.; Danino, D.; Falvey, D. E.; Raghavan, S. R. *Soft Matter* **2013**, *9*, 5025–5033.

(8) Tsuchiya, K.; Orihara, Y.; Kondo, Y.; Yoshino, N.; Ohkubo, T.; Sakai, H.; Abe, M. **2004**, 12282–12283.

(9) Brown, P.; Bushmelev, A.; Butts, C. P.; Cheng, J.; Eastoe, J.; Grillo, I.; Heenan, R. K.; Schmidt, A. M. *Angew. Chemie - Int. Ed.* **2012**, *51*, 2414–2416.

(10) Aathimanikandan, S. V.; Savariar, E. N.; Thayumanavan, S. *J. Am. Chem. Soc.* **2005**, *127*, 14922–14929.

(11) Johnsson, M.; Wagenaar, A.; Stuart, M. C. A.; Engberts, J. B. F. N. *Langmuir* **2003**, *19*, 4609–4618.

(12) Eastoe, J.; Dominguez, M. S.; Wyatt, P.; Beeby, A.; Kingdom, D. H. U.; Heenan, R. K. **2002**, *18*, 7837–7844.

(13) Orihara, Y.; Matsumura, A.; Saito, Y.; Ogawa, N.; Saji, T.; Yamaguchi, A.; Sakai, H.; Abe, M. *Langmuir* **2001**, *17*, 6072–6076.

(14) Hubbard, F. P.; Santonicola, G.; Kaler, E. W.; Abbott, N. L. **2005**, 6131–6136.

(15) Glinka, C. J.; Barker, J. G.; Hammouda, B.; Krueger, S.; Moyer, J. J.; Orts, W. J. *J. Appl. Crystallogr.* **1998**, *31*, 430–445.

(16) Gilbert, E. P.; Schulz, J. C.; Noakes, T. J. *Phys. B Condens. Matter* **2006**, *385-386*, 1180–1182.

(17) Kline, S. R. *J. Appl. Crystallogr.* **2006**, *39*, 895–900.

(18) Neylon, C. *Eur. Biophys. J.* **2008**, *37*, 531–541.

(19) Araos, M. U.; Warr, G. G. *Langmuir* **2008**, *24*, 9354–9360.
(20) Hansen, J.-P.; Hayter, J. B. *Mol. Phys.* **1982**, *46*, 651–656.
(21) Hayter, J. B.; Penfold, J. *Mol. Phys.* **1981**, *42*, 109–118.
(22) Bergström, L. M.; Garamus, V. M. *J. Colloid Interface Sci.* **2012**, *381*, 89–99.
(23) Warr, G. G.; Grieser, F. *Chem. Phys. Lett.* **1985**, *116*, 505–509.
(24) Guinier, A.; Fournet, G. *J. Polym. Sci.* **1955**, *1*, 268.
(25) Bartlett, P.; Ottewill, R. H. *J. Chem. Phys.* **1992**, *96*, 3306–3318.
(26) Lazzara, G.; Milioto, S.; Gradzielski, M. *Phys. Chem. Chem. Phys.* **2006**, *8*, 2299–2312.
(27) Penfold, J.; Tucker, I.; Green, A.; Grainger, D.; Jones, C.; Ford, G.; Roberts, C.; Hubbard, J.; Petkov, J.; Thomas, R. K.; Grillo, I. *Langmuir* **2008**, *24*, 12209–12220.
(28) Parekh, P.; Marangoni, D. G.; Aswal, V. K.; Bahadur, P. *Colloids Surfaces A Physicochem. Eng. Asp.* **2012**, *400*, 1–9.
(29) Parekh, P.; Singh, K.; Marangoni, D. G.; Aswal, V. K.; Bahadur, P. *J. Surfactants Deterg.* **2011**, *15*, 23–32.
(30) Sharp, M. a; Washington, C.; Cosgrove, T. *J. Colloid Interface Sci.* **2010**, *344*, 438–446.
(31) Hayter, J. B.; Penfold, J. *Molecular Physics*, **1981**, *42*, 109–118.
(32) Fritz, G.; Bergmann, A.; Glatter, O. *J. Chem. Phys.* **2000**, *113*, 9733–9740.
(33) King, S. M. 'Small-Angle Neutron Scattering' a report published on ISIS Web page, 1997.

4-2 Development of High-Speed Photoisomerization System using Lophine Dimers Solubilized in Molecular Assemblies

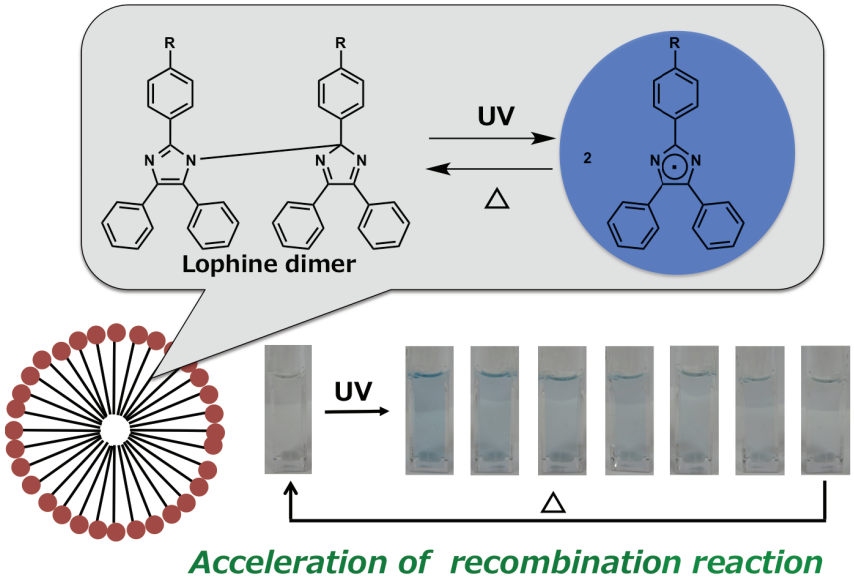

Abstract

This section describes an acceleration of a photo isomerization reaction of a lophine dimer analog by using the inside of micelles as reaction sites. A lophine dimer derivative (**C12-LPD**) was solubilized in 10 mM cetyltrimethylammonium bromide (CTAB) aqueous solution. With UV light irradiation, the color of solution changed from colorless to blue, and than the color faded by maintaining in the dark condition. UV/vis spectra of the solution showed a peak due to lophyl radicals appeared, and then disappeared by keeping in the dark. From these results, a dissociation and recombination reaction of a lophine dimer in a micellar solution was confirmed. A rate of the recombination reaction, obtained from second-order kinetics plot is 0.6785 min^{-1} which shows the reaction is accelerated with ca. 10-fold compared to organic solvents (toluene and octane). These results indicate that the reaction is accelerated because the diffusion of lophyl radicals, confined inside of the micelles, is prevented.

4-2-1 Introduction

Structural control of molecular assembles, triggered by photo stimulus using photochromic molecules, such as azobenzene and spiropyrane have been expected for functional systems because of the cleanness and the simplicity of this methodology.[1–7] These systems are applicable to the drug delivery system (DDS), cosmetics, optical materials, and so on. However, conventional photo-responsive molecular assembles have needed relatively long time to change the properties (their structures), e. g. several hours. In the application for DDS, drugs should be immediately released after photo irradiation. From the point of applications, photo-responsive systems reacting rapidly on an arbitrary time need to be developed or synthesized.

A lophine dimer rapidly dissociates to two lophyl radicals with UV light irradiation, and then these radical species thermally recovered to the initial dimer by a recombination reaction with keeping in the dark condition (Figure 1).[8] Because color tone of the solution changed rapidly in this process, lophine dimer is regarded as one of photochromic molecules. With the rapid dissociation reaction, lophine dimer derivatives have been researched and have used as radical initiators for polymerization reactions.[9] On the other hand, the molecules have not been paid attention as photochromic molecules, because the recombination reaction is relatively slow, compared to the dissociation reaction since collisions between lophyl radicals are unlikely to occur due to diffusion of the species in a solution. These days, Abe and coworkers accomplished a rapid recombination reaction with a synthetic approach.[10–12] In this case, since two lophine unites in the structures dimer are covalently bonded with a naphthalene or a cyclophane moiety, the diffusion of radical species, produced by UV light irradiation, is inhibited. As a result, the recombination reaction proceeds in a second.[12] From these report, I assume that if lophine dimer is confined in a nano-structure, the recombination reaction is accelerated because the distance between the radical species is quite small. This strategy for the acceleration of the reaction is simple, and thus a rapidly tunable photochromic system can be developed. In this study, by using the inside of micelles spontaneously formed by surfactants as a reaction site, an acceleration of the photochromic reaction of lophine dimer has been examined.

4-2-2 Results and discussion

Lophine dimer **C12-LPD**, alkylated with dodecyl chain, was synthesized, because **1** and **2** were not likely to dissolve in any micellar solutions of surfactants due to the less affinity of their aromatic moieties to alkyl chains of surfactant molecules. **C12-LPD** was solubilized in 10 mM cetyltrimethylammonium bromide (CTAB) aqueous solution. After UV light irradiation, color of the solution varied from colorless to blue, and then the color almost faded after ca. 30 min by keeping in the dark condition (Figure 2a). On the other hand, although the colors of **C12-LPD** in toluene and octane as organic solvents also changed to blue, it took about 1 day (Figures 2b and 2c).

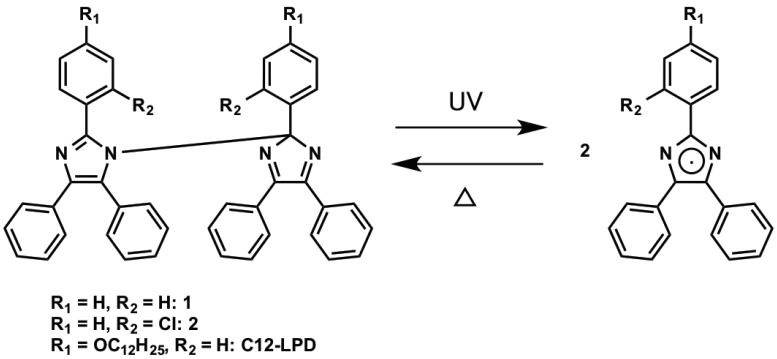

Figure 1. Chemical structures of lophine dimer analogs.

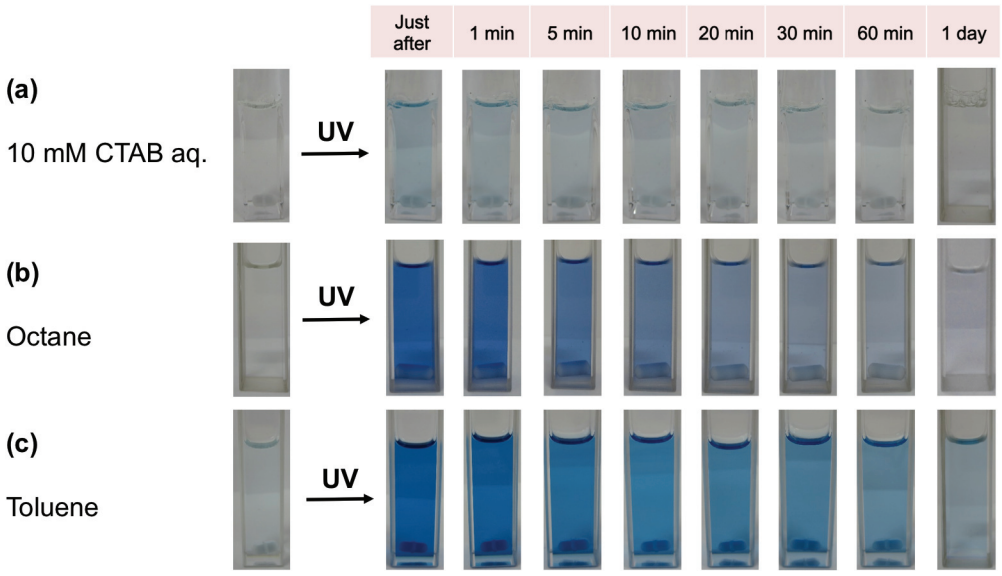

Figure 2. Transient variations in colors of **C12-LPD** in 10 mM CTAB aqueous solution (a), 5×10^{-5} M toluene (b) and octane (c), after UV light irradiation.

These color variations were monitored by UV/vis absorption spectroscopy, as shown in Figure 3. UV/vis spectra showed that after UV light irradiation, the peak at 285 nm due to lophine dimer **C12-LPD** decreased and simultaneously the one at 610 nm appeared. These absorbance recovered by keeping in the dark condition (Figure 3a). The plots of absorbance at 610 nm against time shows this process reached a stationary state in 50 minutes after UV irradiation. In toluene or octane, **C12-LPD** showed similar changes in these spectra (Figures 3b and 3c). However, stationary states in these solutions to disappear the blue color were obtained by over 100 minutes. A half-life $t_{1/2}$ to breach the color was 5.769 minutes, and was shorter than toluene and octane (Table 1). From these results, a dissociation and recombination reaction of **C12-LPD** in a micellar solution was confirmed.

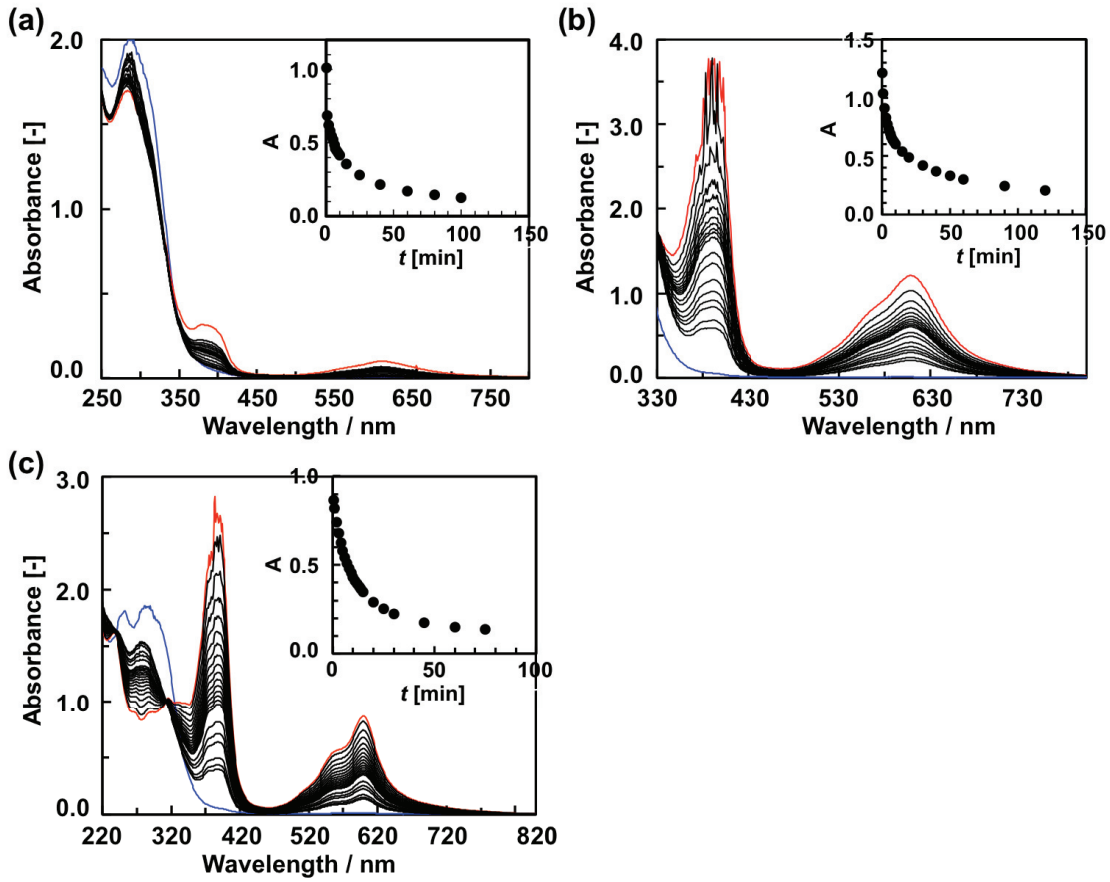

Figure 3. Variations in UV/vis absorption spectra of **C12-LPD** in 10 mM CTAB aq., toulen and octane (5×10^{-5} M) after UV light irradiation. Insets show changes in peaks at around 600 nm due to absorption of lophyl radical with time. The blue and red lines are spectra before and after UV irradiation.

The reaction rate of the recombination reaction of **C12-LPD** in each medium was calculated from the second-order kinetic plot (Figure 4). In 10 mM CTAB aqueous solution, the reaction rate, k is 1.73 min^{-1}. This value is ca. 10-fold bigger than ones in toluene and octane (Table 1).

From these results, the recombination reaction of lophyl radical is accelerated, compared to organic solvents. Octane was chosen for this experiment because the environment produced by octane is close to the inside of CTAB micelles, which is the space of alkyl chains. Moreover, solbilization amounts of **C12-LPD** in the 10 mM CTAB solution, roughly obtained from the spectrum was close to the concentration in octane which I set ([**C12-LPD**] = 5×10^{-5} M). These considerations indicate that by confining a lophine dimer inside of the micelles, the diffusion of the radical species produced by UV light irradiation is prevented, and then the recombination reaction is accelerated. Strehmel and coworkers also have reported the recombination reaction is accelerated within small structures of ionic liquids (IL).[13,14] Thus, to accelerate the recombination reaction of the lophyl radicals, a confinement of the species in small structures can be an effective methodology. In particular, nano-structures formed by surfactants, e. g. micells and microemulsions, are useful since varieties of structures and environments for enhancement of the reaction can be designed by using them.

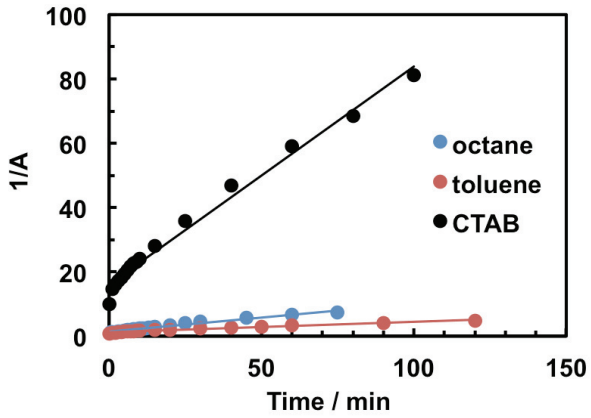

Figure 4. The second-order kinetic plot for **C12-LPD** in 10 mM CTAB aq., toluene and octane.

Table 1. Reaction rates, k and half-time, $t_{1/2}$ of **C12-LPD** in 10 mM CTAB aq., toluene and octane.

	k [min^{-1}]	$t_{1/2}$
10 mM CTAB aq.	1.73	5.77
Toluene	0.0805	10.3
Octane	0.123	9.40

4-2-3 Conclusions

A lophine dimer derivative, **C12-LPD** was solubilized in 10 mM CTAB aqueous solution. The color of the solution varied from colorless to blue with UV light irradiation, and than the blue color changed to the initial state by keeping in the dark condition. This color variation was monitored with UV/vis spectra of the solution. A peak due to lophyl radicals appeared with UV light irradiation, and then disappeared by keeping in the dark. A rate of the recombination reaction, obtained from second-order kinetics plot shows the reaction is accelerated with ca. 10-fold, compared to the uses of organic solvents. These results indicate that lophyl radicals smoothly recombine inside of the micelles, and the reaction is accelerated in this condition. Based on this result, if a surfactant bearing lophine dimer is synthesized, the recombination reaction of lophyl radicals in micelles formed by this surfactant is accelerated and a rapid control of the assembling structure is simultaneously possible.

4-2-4 Experimental part

General procedures.

Solvents and reagents were purchased from Tokyo Chemical Industry Co. Ltd. (Tokyo, Japan) or Wako Pure Chemical Co. (Osaka, Japan) and were used without further purification. **2** was purchased from Tokyo Chemical Industry Co. Ltd. (Tokyo, Japan) and was used without further purification. All reaction mixtures and fractions eluted by column chromatography eluents were monitored using thin layer chromatography (glass backed (TLC) plates (Kieselgel 60 F254). The developed thin layer chromatography plates were observed under UV light at 254 and 365 nm. Flash column chromatography over silica gel (LC60A35-70 μM) was used for all separations.

Measurements.

^{1}H and ^{13}C NMR spectra were measured at 298 K from an acetone-d_6 solution of the samples using a JEOL model JNM-AL300 (300 MHz) spectrometer with $SiMe_4$ as internal standard. Chemical shifts (*d*) and coupling constants (*J*) are given in parts per million and Hertz, respectively. ESI-MS spectra were measured using a JASCO model JMS-T100CS. UV/vis absorption spectra were measured using Agilent 222 UV/vis spectrophotometer with a quartz cuvette (1.0 cm path length).

UV light irradiation.

UV light irradiation was conducted using a 200 W Hg-Xe Lamp (SUPERCUR UVF-203S, SAN-EI ELECTRONIC). Irradiation wavelengths (300–390 nm) were accomplished using color filters. Each solution was irradiated with light (10 mW/cm^2) in a 1.0 cm path quartz cuvette.

Synthesis and structural characterization.

Preparation of lophine dimer **1** has been reported previously.[8] A synthetic route of **C12-LPD** is shown in scheme 1.

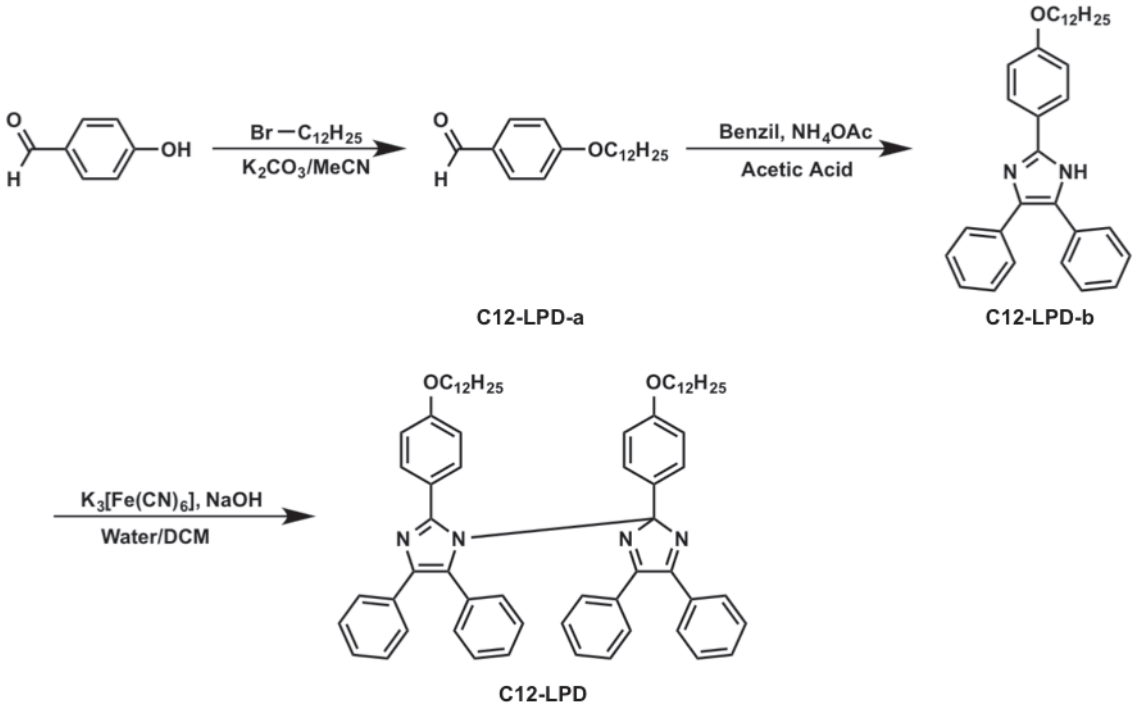

Scheme 1. Synthesis of host molecule **C12-LPD**.

2-(4-(((25λ^1-pentacosaoxidanyl)dodeca-1,3,5,7,9,11-hexayn-1-yl)oxy)phenyl)-4,5-diphenyl-1*H*-imidazole (C12-LPD-b)

K_2CO_3 (4.0 g, 30 mmol) was added to a solution of a mixture of 4-Hydroxybenzaldehyde (1.83 g, 15 mmol), 1-Bromododecane (2.49 g, 10 mmol) and catalytic amounts of KI in CH_3CN (30 ml), and the resulting suspension was refluxed for 12 h. The reaction mixture was allowed to cool to room temperature and solvent removed under reduced pressure. The residue was dissolved in ethyl acetate and the solution was washed with water, dried over anhydrous Na_2SO_4, and then solvent was removed under reduced pressure. The crude product was subjected to column chromatography (SiO_2, AcOEt/hexane 1/2 v/v) yielding the product as colorless oil. This crude product was used synthesis of **C12-LPD-b**. A l00mL flask was charged with benzil (1.179 g, 7.9 mmol), a crude product of **C12-LPD-b** (2.312 g, 8.0 mmol), and ammonium acetate (3.4 g, 64.8 mmol) in acetic acid (16 mL) and the mixture was refluxed for 3h. After evaporation of the solvent, the crude product was washed with ethyl acetate, then was recrystallized from ethyl acetate to yield 1.056 g (28 %) as a pale yellow powder. ^{1}H-NMR (300 MHz, $CDCl_3$, 25 ºC): d = 0.86 (t, 3H J = 6.0), 1.22–1.47 (m, 18H), 1.64–1.88 (m, 2H), 3.88 (s, 2H), 6.68–6.97 (m, 8H), 7.07 (d, 4H, J = 6.0),

8.25 (d, 2H, J = 9.0) ppm. ESI-MS: m/z = 481.32 $[M+H]^+$.

2,2'-bis(4-(((25λ^1-pentacosaoxidanyl)dodeca-1,3,5,7,9,11-hexayn-1-yl)oxy)phenyl)-4,4',5,5'-tetraphenyl-2'*H*-1,2'-biimidazole (C12-LPD)

A mixture of **3-b** (0.240 g, 0.5 mmol) in dichloromethane (15 mL), potassium ferricyanide (0.626 g, 1.7 mmol), and sodium hydrate (0.6 g, 15 mol) dissolved in water (5 mL) was stired for 24 h at room temperature. The reaction mixture was washed twice with water and the isolated organic phase was dried by anhydrous sodium sulfate. Upon removal of the solvent, the raw product was purified by flash column chromatography (silica gel) using $CHCl_3$/hexane = 1/1 as the eluent. After evaporation of the solvent, the amorphous product was dried in vacuo and kept for a couple of day to yield 0.216 g (90 %) as a yellow powder. ESI-MS: m/z = 981.61 $[M+Na]^+$. ^{1}H-NMR spectra could not be assigned completely because existences of a series of isomers.

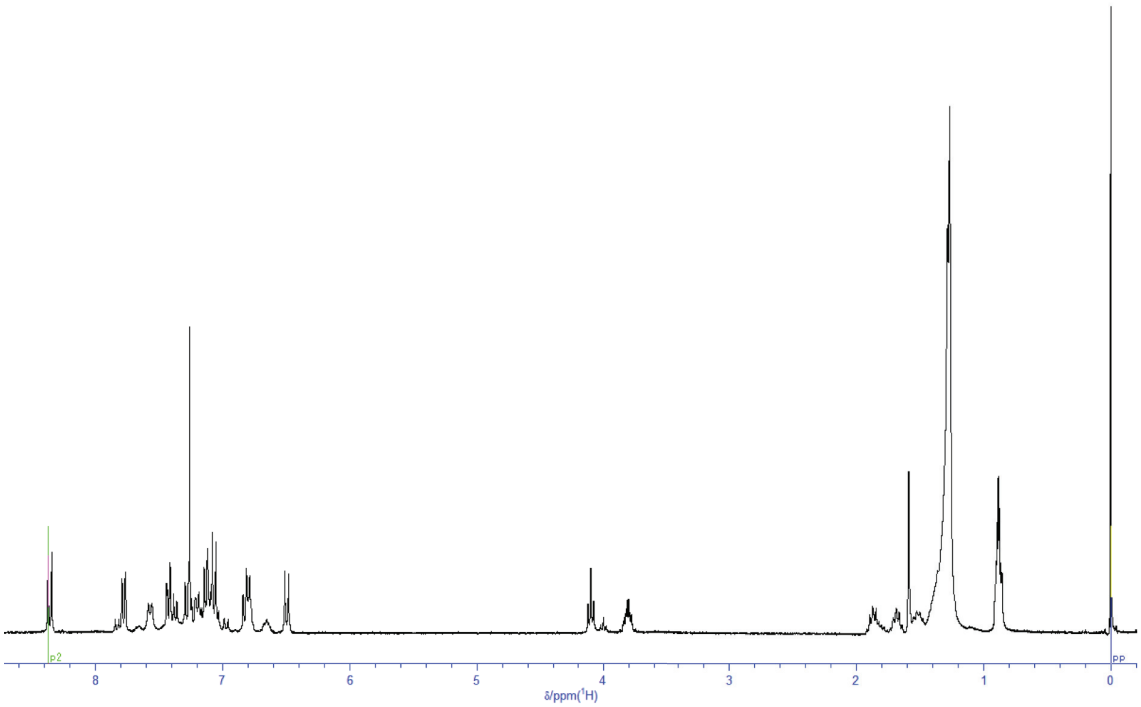

Figure 5. ^{1}H-NMR spectrum of **C12-LPD-b** (300 MHz, $CDCl_3$, 25 ºC).

Sample preparation.

Excess amount of lophine dimer derivatives were added to 10 mM CTAB aqueous solution, and this mixture was stirred with a magnetic stirrer for a couple of days to a reach equilibrium. Surplus lophine dimer was removed by a filtration.

Calculation of a reaction rate of the photochromic reaction using the second-order kinetics plot.

Second-order reaction is expressed by

$$\frac{1}{C} - \frac{1}{C_0} = k't \qquad (1)$$

where C and C_0 are concentration of lophyl radical after t and 0 minute later, k' reaction rate, and t . Here, A and A0, of lophyl radical after t and 0 minute later are treated as C and C_0.

$$\frac{1}{A} - \frac{1}{A_0} = kt \qquad (2)$$

The obtained k is reaction rate of the recombination reaction of a lophyl radical.

References

(1) Eastoe, J.; Vesperinas, A. *Soft Matter*, **2005**, *1*, 338–347.

(2) Bonini, M.; Berti, D.; Di Meglio, J. M.; Almgren, M.; Teixeira, J.; Baglioni, P. *Soft Matter* **2005**, *1*, 444–454.

(3) Aikawa, S.; Shrestha, R.; Ohmori, T.; Yuko, F.; Yoji, T.; Endo, T.; Kanjiro, T.; Koji, T.; Kazutami, S.; Kenichi, S.; Masahiko, A.; Hideki, S. *Langmuir* **2013**, *29*, 5668–5676.

(4) Matsumura, A.; Tsuchiya, K.; Torigoe, K.; Sakai, K.; Sakai, H.; Abe, M. *Langmuir* **2011**, *27*, 1610–1617.

(5) Gohy, J.; Zhao, Y. *Chem. Soc. Rev.* **2013**, *42*, 7117–7129.

(6) Oh, H.; Ketner, A. M.; Heymann, R.; Kesselman, E.; Danino, D.; Falvey, D. E.; Raghavan, S. R. *Soft Matter* **2013**, *9*, 5025–5033.

(7) Shi, H.; Ge, W.; Oh, H.; Pattison, S. M.; Huggins, J. T.; Talmon, Y.; Hart, D. J.; Raghavan, S. R.; Zakin, J. L. *Langmuir* **2013**, *29*, 102–109.

(8) Taro, Hayash.; Koko, M. *Bull. Chem. Soc.* **1960**, *33*, 565–566.

(9) Monroe, B. M.; Weed, G. C. *Chem. Rev.* **1993**, *93*, 435–448.

(10) Iwahori, F.; Hatano, S.; Abe, J. *J. Phys. Org. Chem.* **2007**, *20*, 857–863.

(11) Fujita, K.; Hatano, S.; Kato, D.; Abe, J. *Org. Lett.* **2008**, *10*, 3105–3108.

(12) Kishimoto, Y.; Abe, J. *J. Am. Chem. Soc* **2009**, *131*, 4227–4229.

(13) Strehmel, V.; Wishart, J. F.; Polyansky, D. E.; Strehmel, B. *ChemPhysChem* **2009**, *10*, 3112–3118.

(14) Berdzinski, S.; Horst, J.; Straßburg, P.; Strehmel, V. *ChemPhysChem* **2013**, *14*, 1899–1908.

Chapter 5
Summary

In this thesis, the studies on developments of photo-functional systems based on supramolecular chemistry by utilizing dynamic chemical equilibrium were described.

In Chapter 2, developments of an optical sensor and molecular memory, based on acid-base reaction of phenol fluorophores were described. In section 2-1, alcohol sensors with fluorescence response were developed by using composites of terphenol derivatives and bases. Commercially available alcohol beverages were qualitatively detected with the naked eye. In section 2-2, volatile and non-volatile molecular memories were developed based on acid-base reaction of phenolic hydroxyl group with fluoride anion and water molecules. These memory systems also can treat with not only on-off, but also varieties of information.

In Chapter 3, developments of cesium probe were described. A fluorescene probe for cesium was newly synthesized with the terphenol unit as mentioned in Chapter 2. This cesium probe detected cesium on the surface of solid. With the probe, an accumulation spot of cesium was imaged in a cell of the plant (*Arabidopsis*) for the first time. Moreover, with an optode system, cesium ion was detected in the aqueous system, even in sea and tap water. Thus, cesium was detected in three systems, which are mainly contaminated by radioactive cesium due to the nuclear plant accident.

Chapter 4 treats with developments of photo-functional systems with molecular assembles, formed by surfactants. In section 4-1, SANS analysis was carried out for micelles formed by a photo-responsive surfactant (AZTMA). The numbers of micelles, formed at around CMC (5 mM) decreased with UV light irradiation. 10 mM AZTMA solution forms ellipsoidal micelles, and the long radius decreased with UV light irradiation. Moreover, these values, such as the numbers of micelles and the radius recovered with subsequent irradiation of visible light. From these results, effects of photo-irradiation on structures of the micelles and the solution property were understood. Section 4-2 describes an acceleration of a photo isomerization reaction of a lophine dimer was investigated by using the inside of micelles as reaction sites. A recombination reaction of lophyl radicals, produced by lophine dimer with UV light irradiation was carried out in micellar solutions. A rate of the recombination reaction was accelerated with ca. 10-fold in micelles formed by CTAB, compared to organic

solvents, such as toluene and octane. It is expected that the reaction is accelerated because the diffusion of lophyl radicals, solubilized in the micelles, is prevented.

As mentioned above, I have tried developments of photo-functional systems by using dynamic chemical equilibrium, such as sensors, memories, and also photo-responsive molecular assembles by using the supramolecular strategy. In particular, I have developed not only new functions of sensors and memories, but also tried to focus on developments of functional systems with visible information because visualized information in sensors and memories are simple and easy to recognize. I expect that functional devices bearing visible information are developed more in the future. In addition, the structures of photo-responsive surfactant systems were analyzed precisely, and effects of photo-irradiation on solution properties were understood. I hope these results would be utilized for developments of new photo-responsive molecular assembles.

Publication list

Main papers

1. Taizo Mori, ○Masaaki Akamatsu, Ken Okamoto, Masato Sumita, Yoshitaka Tateyama, Hideki, Sakai, Jonathan P. Hill, Masahiko Abe and Katsuhiko Ariga,
   "Micrometer-level Naked-eye Detection of Caesium Particulates in the Solid State"
   Sci. Technol. Adv. Mater., **2013**, *14*, 015002.
2. ○Masaaki Akamatsu, Hirokazu Komatsu, Taizo Mori, Eri Adams, Ryoung Shin, Hideki Sakai, Masahiko Abe, Jonathan P. Hill, and Katsuhiko Ariga,
   "Intracellular Imaging of Cesium Distribution in Arabidopsis Using Cesium Green"
   ACS Appl. Mater. Interfaces, **2014**, *6* (11) 8208–8211.
3. ○Masaaki Akamatsu, Taizo Mori, Ken Okamoto, Hideki Sakai, Masahiko Abe, Jonathan P. Hill and Katsuhiko Ariga,
   "Multicolour Fluorescent Memory based on the Interaction of Hydroxy Terphenyls with Fluoride Anions"
   Chem. Eur. J. **2014**, *20* (49) 16293–16300.

Additional research products

Original papers

1. ○Masaaki Akamatsu, Paul Fitzgerald, Mayu Shiina, Yoichi Orihara, Takeshi Endo, Kenichi Sakai, Masahiko Abe, Gregory G. Warr and Hideki Sakai
   "Micelle Structure in a Photo-Responsive Surfactant with and without Solubilized Ethylbenzene from Small-Angle Neutron Scattering"
   J. Phys. Chem. B, submitted.
2. ○Masaaki Akamatsu, Taizo Mori, Ken Okamoto, Hirokazu Komatsu, Ken Kumagai, Seimei Shiratori, Masaki Yamamura, Tatsuya Nabeshima, Hideki Sakai, Masahiko Abe, Jonathan P. Hill and Katsuhiko Ariga
   "Visual Estimation of Ethanol Contents in Alcoholic Beverages"
   ACS Appl. Mater. Interfaces, submitted.

Book chapter

1. Katsuhiko Ariga, Gary J. Richards, ○Masaaki Akamatsu, Hironori Izawa, and Jonathan P. Hill (editor: Katsuhiko Ariga)
   "Supramolecular Materials Nanoarchitechtonics",
   MANIPULATION OF NANOSCALE MATERIALS: AN INTRODUCTION TO NANOARCHITECTONICS
   Royal Chemical Society, 2012, Chapter 2, 7-27.

Reviews

1. Katsuhiko Ariga, Taizo Mori, ○Masaaki Akamatsu, Jonathan P. Hill,
   "Two-Dimensional Nanofabrication and Supramolecular Functionality Controlled by Mechanical Stimuli"
   Thin Solid Films **2014**, *554* 32–40.
2. Katsuhiko Ariga, Hirokazu Komatsu, ○Masaaki Akamatsu, Qingmin Ji, Jonathan P. Hill
   "Nanoarchitectnics cellar imaging"
   Display and Imaging, accepted.

Patent

森泰蔵、有賀克彦、○赤松允顕、岡本健、ヒル　ジョナサン　ピー
「蛍光プローブ、および、セシウム含有物質を検出する方法」
12MS098FR

Award

1. Poster award, the World Congress on Oleo Science (WCOS 2012) & 29th ISF Congress, Arkas Sasebo, Japan, Sep. 30-Oct. 4, 2012.
2. Best student award, 28th SPSJ Young Scientist Meeting, Tsukubamirai, Japan, Oct. 7-8, 2013.
3. 6th Hopemeeting, Tokyo, Japan, selected as one of 25 attendants from PhD students and young scientists in Asia and pacific countries.
4. Poster award, the 65th Divisional Meeting on Colloid & Interface Chemistry, Tokyo University of Science, Japan, Sep. 4, 2014.

Acknowledgements

First of all, I would like to express deepest gratitude to Professor Hideki Sakai, for educating me to be a researcher and giving me a great opportunity to research this interesting PhD project. His professional guidance and evocative suggestions greatly contributed to the success of my project in Tokyo University of Science.

I would like to express sincerest gratitude to Dr. Katsuhiko Ariga, principle investigator, for giving me a wonderful opportunity to research this project in National Institute for Material Science (NIMS.)

I owe a very important debt to Dr. Jonathan P. Hill, Dr. Ken Okamoto, Dr. Taizo Mori and Hirokazu Komatsu in NIMS for giving me meaningful advices, precious discussion and guidance in specific techniques and skill of experiment about this project. Without their supports, I couldn't have advanced this project.

I am indebted to professor Gregory G. Warr and Dr. Paul FitzeGerald in the University of Sydney for giving a great opportunity to engage small-angle neutron scattering measurements and supporting me for the experiments in Sydney, Australia.

I would like to deeply thank Dr. Masato Sumita in NIMS for giving me advices about photochemistry and supporting this project by his technique about computational simulation.

I also thank professor Masahiko Abe and professor Kenichi Sakai in Tokyo University of Science for giving advices encouraging suggestion in this project.

I would like to thank other staff members of Sakai-Sakai group in Tokyo University of Science; Dr. Kanjiro Torigoe and Dr. Takeshi Endo.

I'm grateful to my senior student, Dr. Takeshi Misono in Sakai-Sakai group for giving me how to stay as a PhD student.

I also thanks to Mr. Taiki Suzuki and Mr. Atsuki Matsuda to support my projects.

I also wish to thank all past and present group members of Sakai-Sakai group (or Abe-Sakai group) in Tokyo University of Science and Supramolecular group in NIMS, who helped me and give me a lot of pleasant memories for this 6-year.

Finally, I wish to thank my parents, brother, and grandparents, for their encouragement throughout my life. Without their support, I could not have completed this research.

Masaaki Akamatsu
November 2015

Appendix for Chapter 2-2

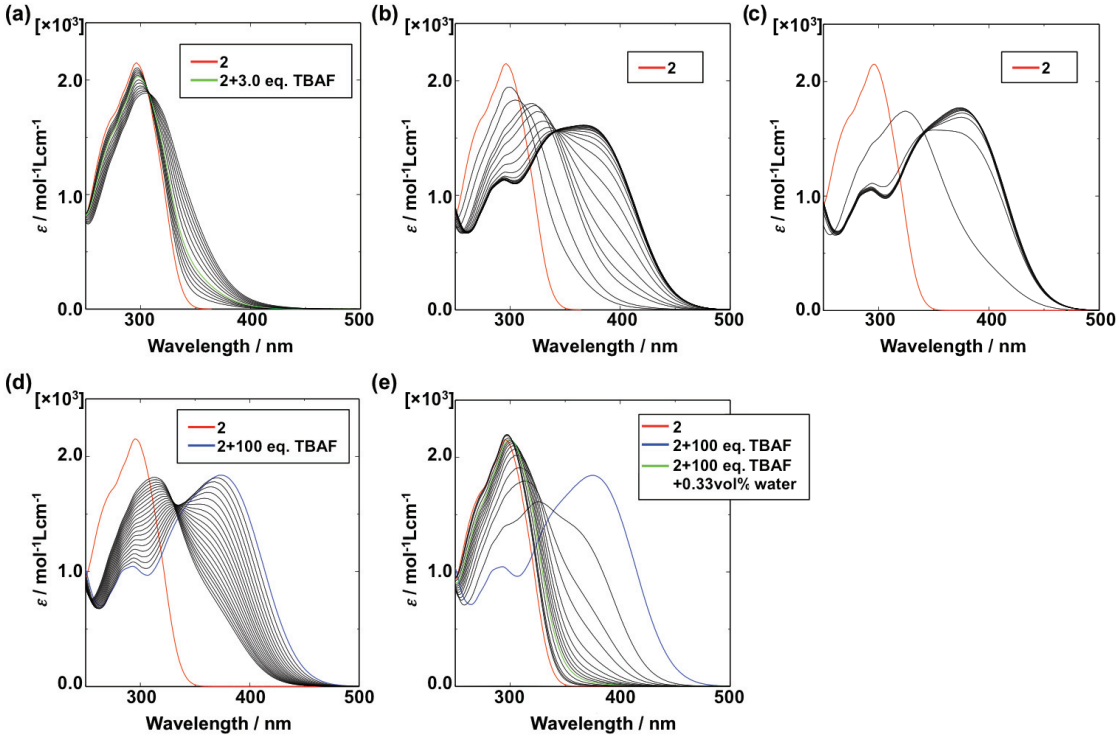

Figure A1. Variations in UV/vis absorption spectra with addition of TBAF and water ([**2**] = 1×10^{-4} M in THF): (a) addition of 0-1.00 eq. TBAF (increment of 0.03 eq. TBAF: 0.05-0.30 eq., increments of 1.0eq. TBAF: 0.30-1.00eq.). (b) Addition of 0-10.0 eq. TBAF (increments of 0.50 eq. TBAF). (c) Addition of 0-0.33 vol% water to **2** solution containing 100eq. TBAF, (d) Addition of 0.0-3.2 vol% water to **2** solution containing 100 eq. TBAF.

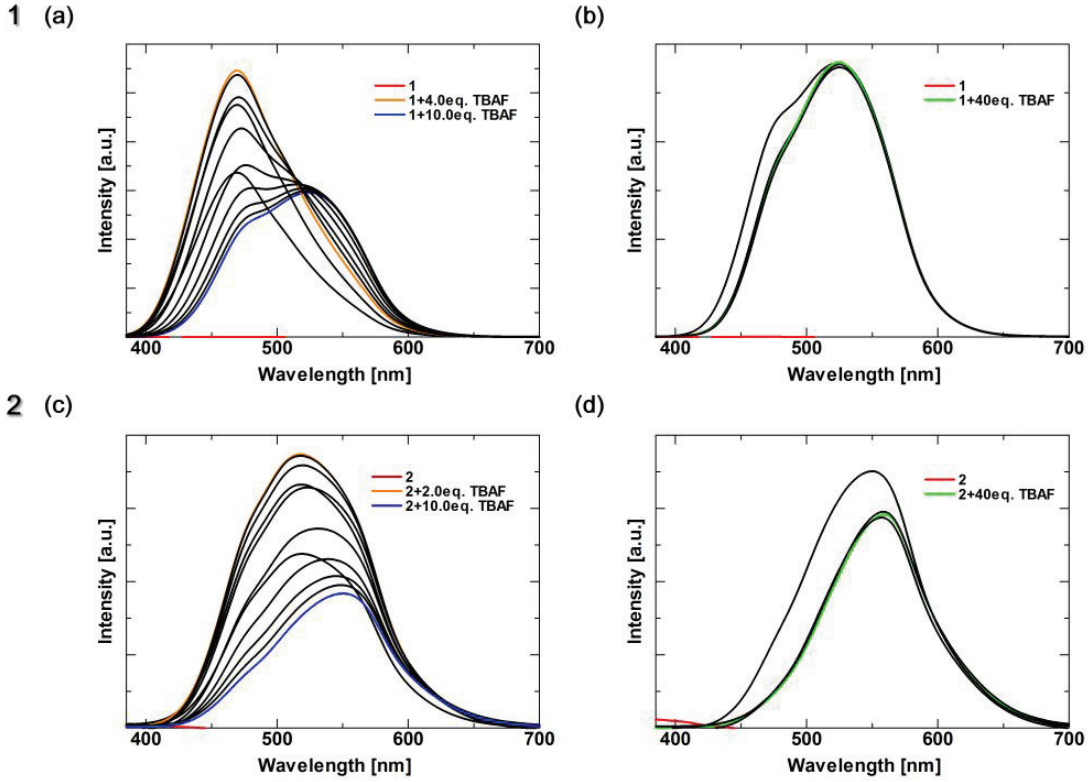

Figure A2. Variations in fluorescence spectra with addition of TBAF ([**1**] or [**2**] = 1×10^{-4} M in THF, ex: 365 nm): (a) Addition of 0-10.0 eq. TBAF (increments of 1.0 eq.TBAF) to **1** solution. (b) Addition of 0-40.0 eq. TBAF (increments of 10.0eq. TBAF) to **1** solution. (c) Addition of 0-10.0 eq. TBAF (increments of 1.0 eq. TBAF) to **2** solution. (d) Addition of 0.0-50.0 eq. TBAF (increments of 10.0 eq. TBAF) to **2** solution.

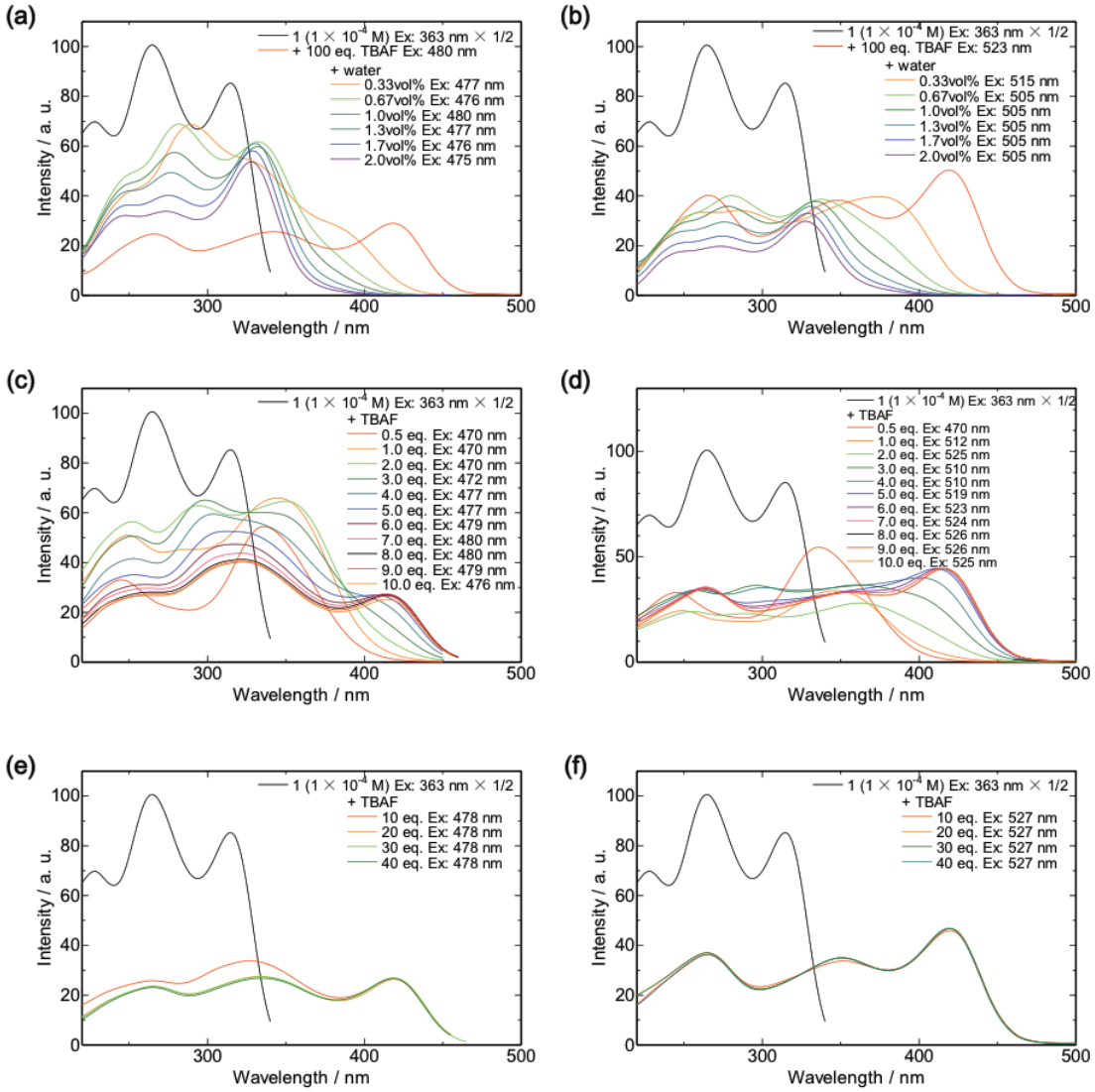

Figure A3. Excitation spectra with addition of TBAF and water ([**1**] = 1×10^{-4} M in THF): (a), (b) addition of water into a solution of **1** containing TBAF; (c)-(f) addition of TBAF.

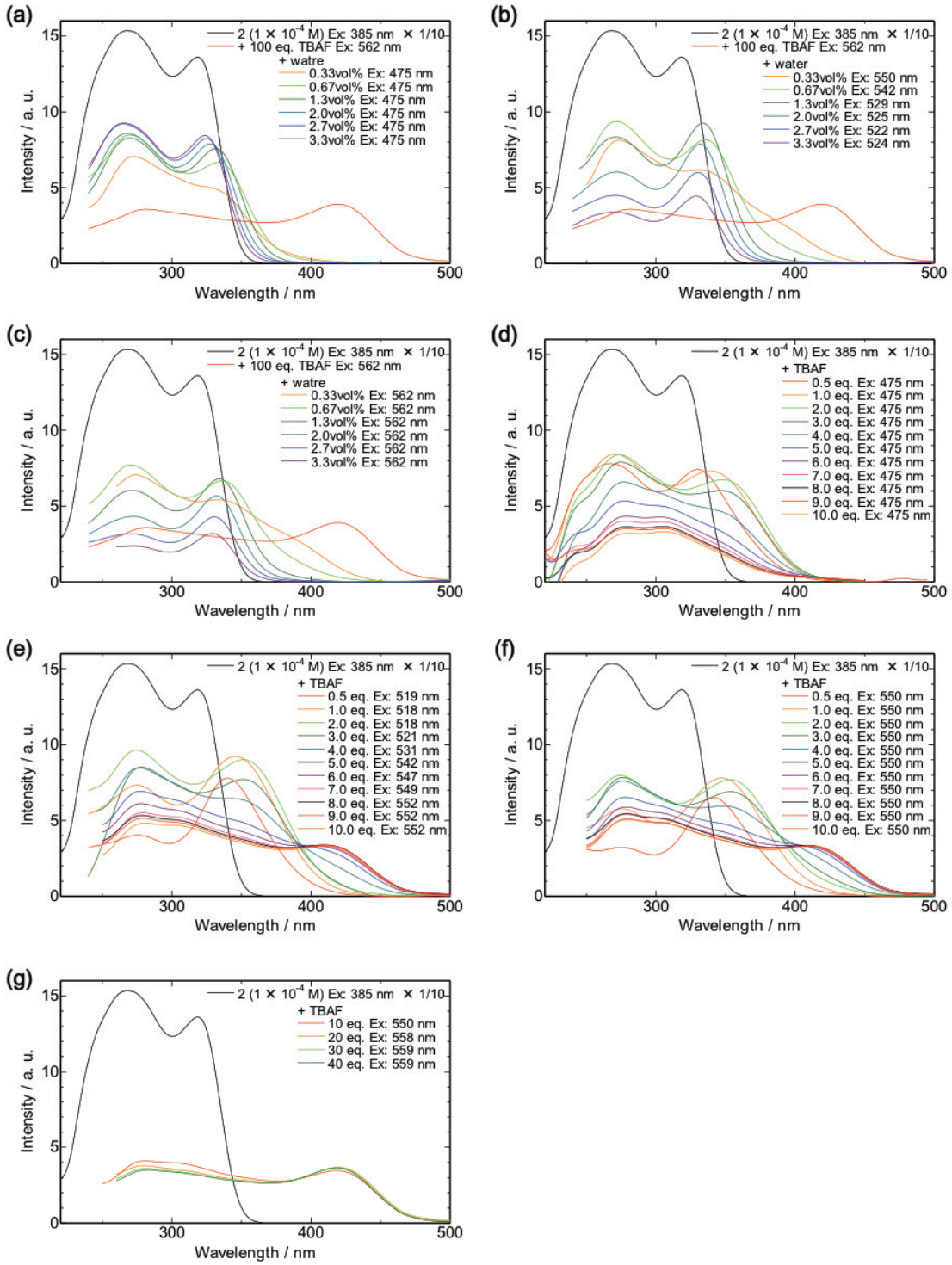

Figure A4. Excitation spectra with addition of TBAF and water ([**2**] = 1×10^{-4} M in THF): (a)-(c) addition of water to a solution of **2** containing TBAF; (d)-(g) addition of TBAF.

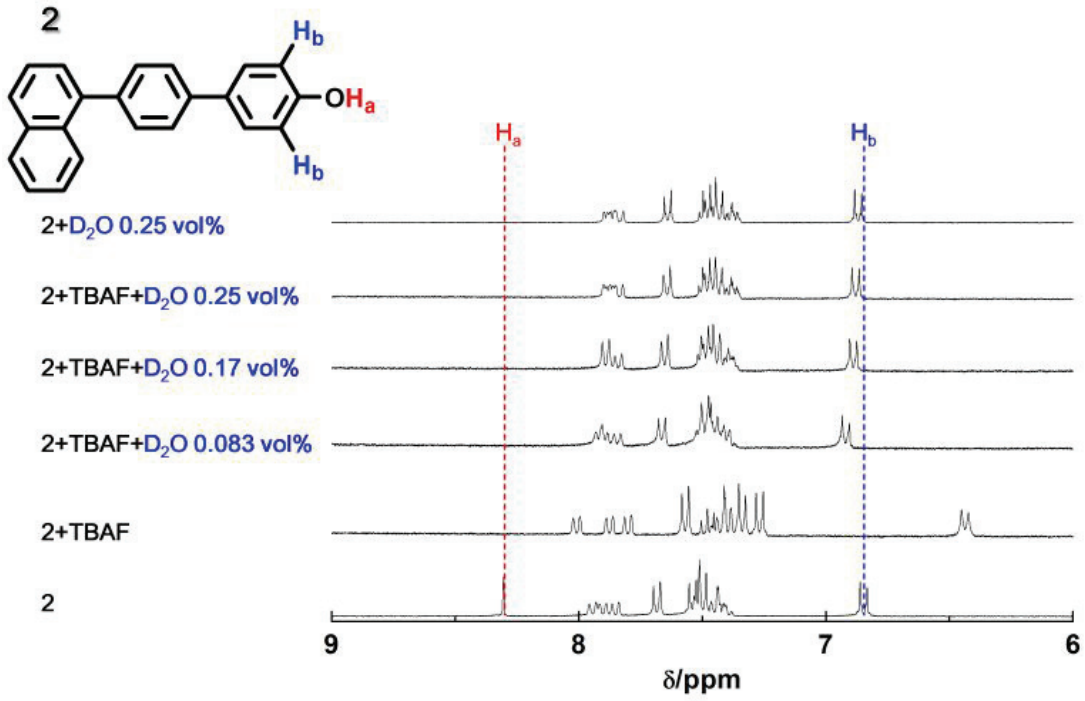

Figure A5. Variation of ^{1}H-NMR spectra of **2** with addition of TBAF and deuterated water (1.0 mg/600 µl THF-d_8, 30 eq. TBAF, rt, 300 MHz).

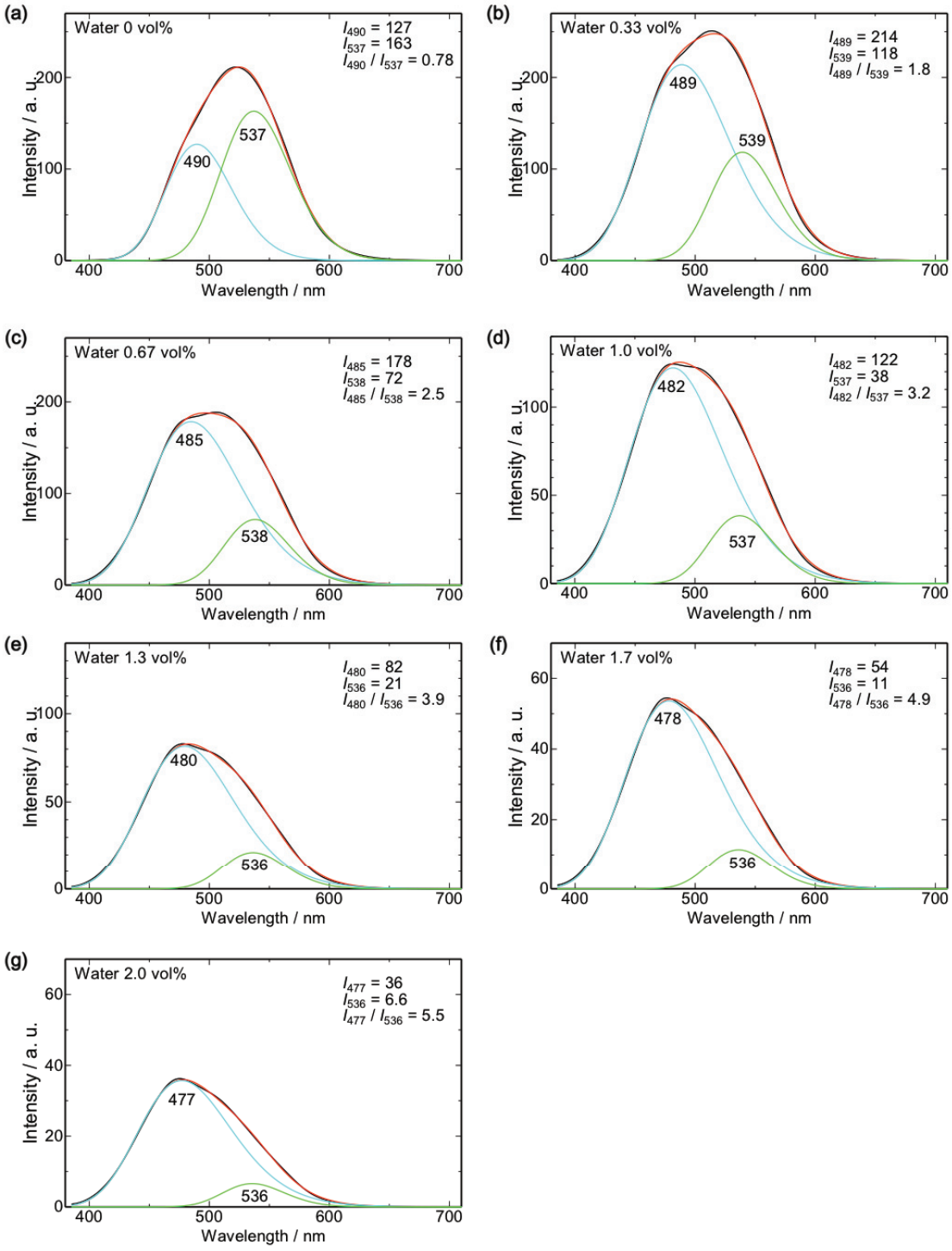

Figure A6. Original fluorescence spectra and peak deconvoluted curves of **1** (Figure 2d).

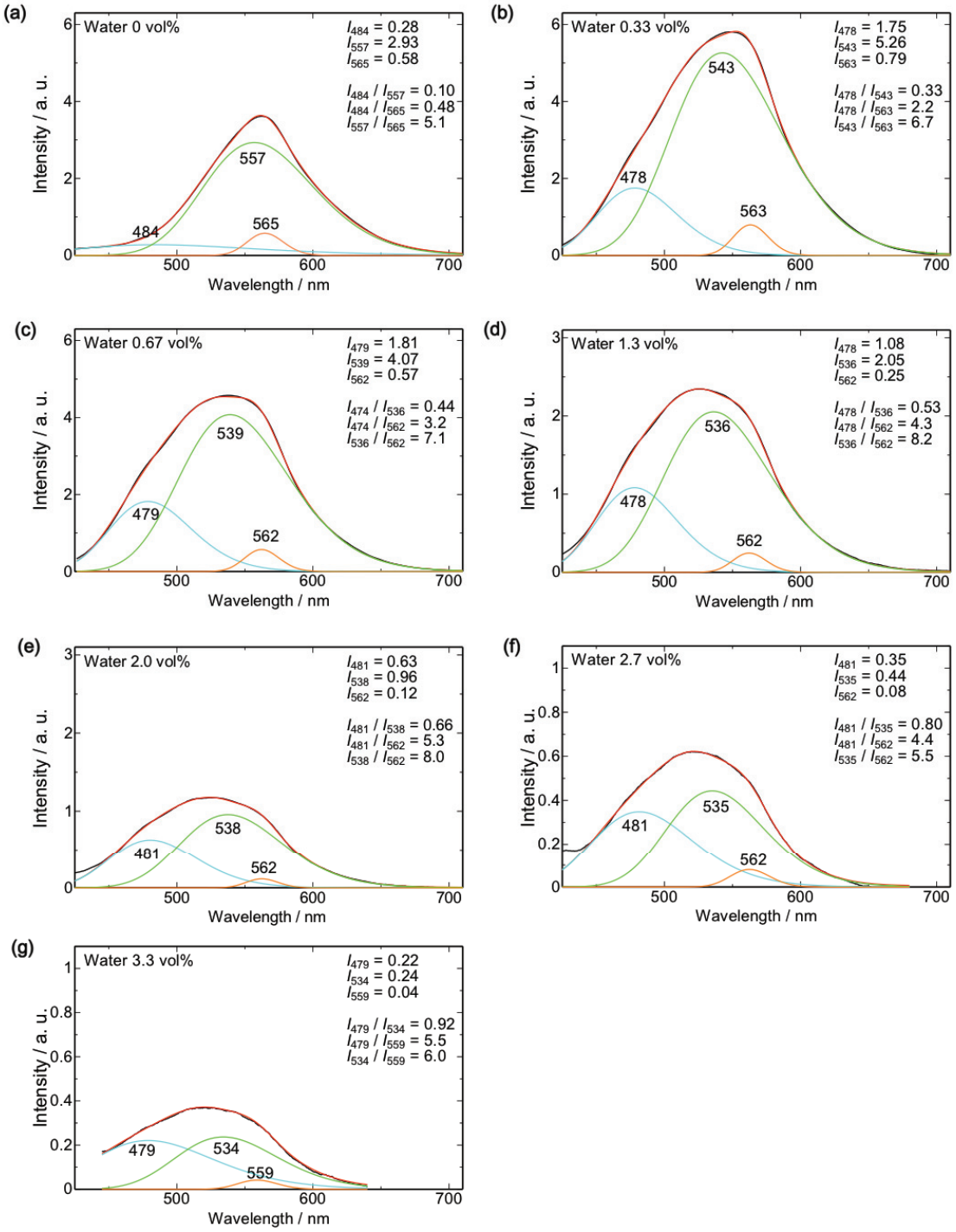

Figure A7. Original fluorescence spectrum and peak deconvoluted curves of **2** (Figure 2d).

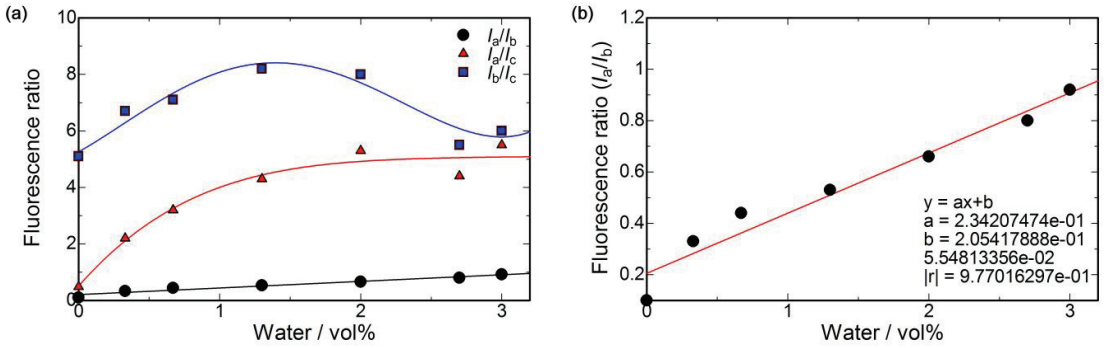

Figure A8. Ratio of fluorescence intensities of **2** to amounts of water.

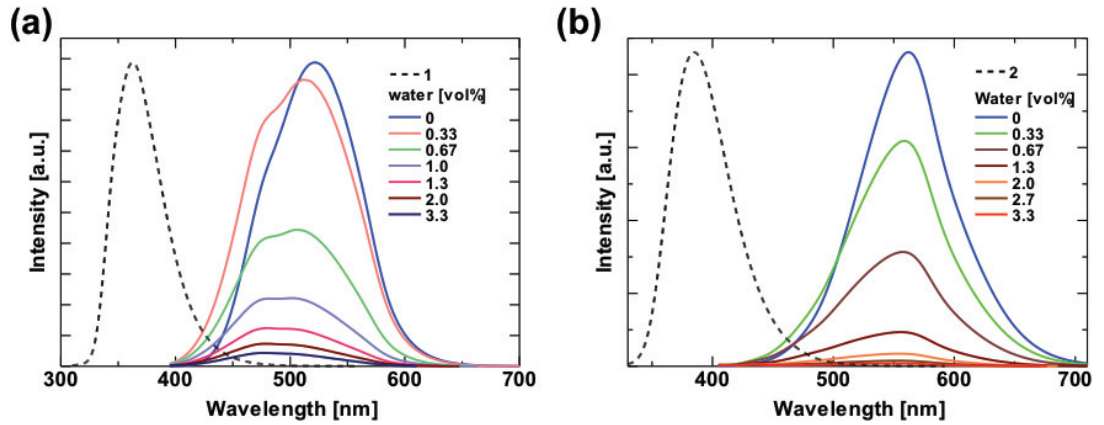

Figure A9. Fluorescence spectra of (a) **1** and (b) **2** with addition of TBAF (dashed black line) and water in THF (1×10^{-4} M). Water was titrated into the solution containing 100 eq. TBAF. The solution of **1** was excited at 290 nm (before addition of TBAF) and 375 nm. (after addition of TBAF/water), and that of **2** was at 306 nm (before addition of TBAF) and 385 nm (after addition of TBAF/water).

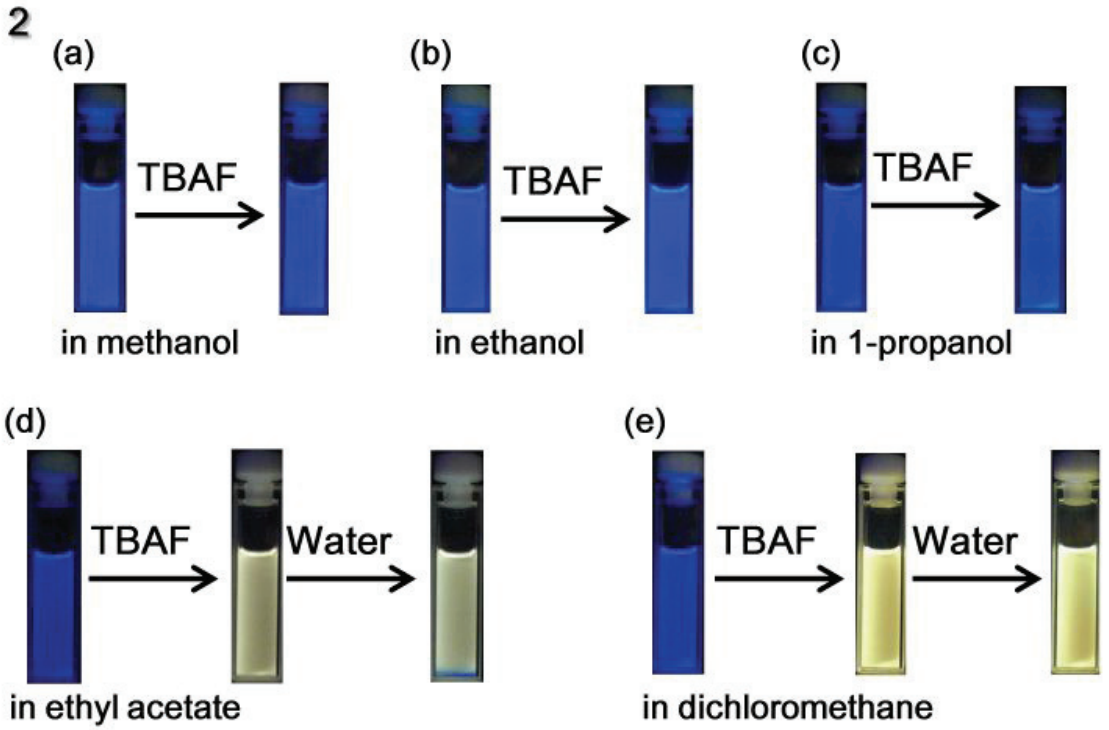

Figure A10. Fluorescence color changes of **2**with addition of TBAF in protic solvents: (a) methanol, (b) ethanol and (c) 1-propanol; non-polar solvents: (d) ethyl acetate, (e) dichloromethane. Water was added into these non-polar solvent solutions (1×10^{-4} M, 100eq. TBAF, ex: 365 nm).